

STATUS OF THESIS

Title of thesis Development of Titanium Dioxide Photoelectrode Material for Dye Solar Cell

I SITI NUR AZELLA BINTI ZAINE
(CAPITAL LETTERS)

hereby allow my thesis to be placed at the Information Resource Center (IRC) of Universiti Teknologi PETRONAS (UTP) with the following conditions:

1. The thesis becomes the property of UTP
2. The IRC of UTP may make copies of the thesis for academic purposes only
3. This thesis classified as

Confidential

Non-confidential

If this thesis is confidential, please state the reason:

This study involves development of a novel structure photoelectrode material which could spur the development of higher performance DSC. Besides, this research finding is also in the process of patent filing. Currently, research work has been carried out for further improvement of the performance of DSC.

The contents of this thesis will remain confidential for 1 year.

Remarks on disclosure:



Signature of Author

Permanent address: No 193,
Blok Kota Bharu, Ayer Lanas
17700, Jeli,
Kelantan.

Date: 2/7/2012

Endorsed by 

Signature of Supervisor

Name of Supervisor
Prof. Dr. Norani Muti Mohamed

Date: 2/7/2012

Prof. Dr. Norani Muti Mohamed
Director of Nanotechnology Research
Fundamental & Applied Sciences Department
Universiti Teknologi PETRONAS

UNIVERSITI TEKNOLOGI PETRONAS

DEVELOPMENT OF TITANIUM DIOXIDE PHOTOELECTRODE MATERIAL
FOR DYE SOLAR CELL

by

SITI NUR AZELLA BINTI ZAINÉ

The undersigned certify that they have read, and recommend to the Postgraduate Studies Programme for acceptance this thesis for the fulfillment of the requirements for the degree stated.

Signature:



Prof. Dr. Norani Muti Mohamed
Director of Nanotechnology Research
Fundamental & Applied Sciences Department
Universiti Teknologi PETRONAS

Main Supervisor:

Prof. Dr. Norani Muti Mohamed

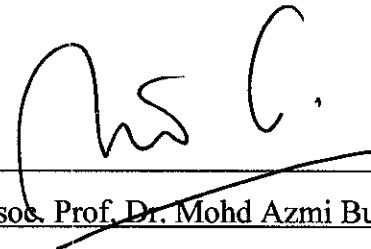
Signature:



Co-Supervisor:

Assoc. Prof. Dr. Mohd Azmi Bustam @ Khalil

Signature:



Head of Department:

Assoc. Prof. Dr. Mohd Azmi Bustam @ Khalil

Date:

3/7/2012

Assoc. Prof. Dr. Mohamed Azmi Bustam @ Khalil
Head, Chemical Engineering Department
Universiti Teknologi PETRONAS

DEVELOPMENT OF TITANIUM DIOXIDE PHOTOELECTRODE MATERIAL
FOR DYE SOLAR CELL

by

SITI NUR AZELLA BINTI ZAINE

A Thesis

Submitted to the Postgraduate Studies Programme
as a Requirement for the Degree of

Prof. Dr. Noraini Mustaffa
PhD in Chemical Engineering
Research Fellow
Senior Lecturer
Chemical Engineering Department
UNIVERSITI TEKNOLOGI PETRONAS
BANDAR SERI ISKANDAR,
PERAK

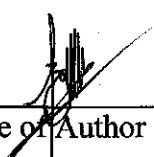
JUNE 2012

DECLARATION OF THESIS

Title of thesis Development of Titanium Dioxide Photoelectrode Material for Dye Solar Cell

I SITI NUR AZELLA BINTI ZAINÉ
(CAPITAL LETTERS)

hereby declare that the thesis is based on my original work except for quotations and citations which have been duly acknowledged. I also declare that it has not been previously or concurrently submitted for any other degree at UTP or other institutions.

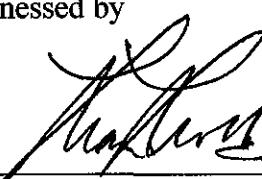


Signature of Author

Permanent address: No 193,
Blok Kota Bharu, Ayer Lanas,
17700, Jeli,
Kelantan.

Date: 2/7/2012

Witnessed by



Signature of Supervisor

Name of Supervisor
Prof. Dr. Norani Muti Mohamed

Date: 2/7/2012

Prof. Dr. Norani Muti Mohamed
Director of Nanotechnology Research
Fundamental & Applied Sciences Department
Universiti Teknologi PETRONAS

ACKNOWLEDGEMENTS

I would like to express word of appreciation with the success and completion of this thesis. Thanks to the almighty God for giving me strength to finally complete my MSc study.

I would like to show my greatest gratitude to my supervisor, Prof. Dr. Norani Muti Mohamed and my co-supervisor, Assoc. Prof. Dr. Mohamad Azmi Bustam @ Khalil. With their guidance, advice and cooperation have helped me to endure the problems and challenges faced throughout my study period. Furthermore, I am very thankful to the research team at Dye Solar Lab of Universiti Teknologi PETRONAS for their assistance, support and teamwork in the research activities and sharing ideas.

I am also very thankful for the financial support from Petroleum Research Fund (PRF) and Universiti Teknologi PETRONAS. The research work has extensively used the facilities at university and I am grateful for that.

Thanks to Central Analytical Laboratory (CAL) of Universiti Teknologi PETRONAS and the entire technician for their help and cooperation in samples characterization and evaluation for my research purposes.

Last but not least, I would like to show my appreciation towards my family and friends, which had involved directly and indirectly on my research activities. They are always ready and willing to help me through the tough times and give balance to my life.

ABSTRACT

Dye solar cell (DSC) has advantage over other solar generation; high possibilities for improving parameters, compatible with flexible substrate, lower productions cost and work even in diffuse light. However, DSC still suffers from low efficiency due to the competition between electron generation and recombination.

The aim of the study is to develop TiO₂ photoelectrode material namely nanoparticles, aggregates and aggregates/nanoparticles composite that promise better performance efficiency of DSC. The effect of two critical parameters; percentage of water in ethanol solution and calcination temperature on the morphology and microstructure of the synthesized TiO₂ aggregates have been investigated using SEM, XRD and BET. TiO₂ photoelectrode films were prepared by screen printing technique on FTO glass, dye-coated with N719, and assembled in sandwich configuration with platinized conducting electrode to form DSC. The performance of the integrated DSCs was compared based on UV-Vis absorption and *I-V* characteristic under simulated AM1.5 sunlight illumination with 100 mW/cm² light output.

Synthesized TiO₂ nanoparticles photoelectrode materials exhibit an efficiency of 3.545%, while aggregates synthesized with 0.9 vol% of water shows higher efficiency of 3.915%. The optimum calcination temperature was found to be at 450°C. Higher efficiency of over 4% can be achieved by incorporating 20% nanoparticle in aggregates films synthesized using 0.9 vol% of water content and calcined at 450°C, producing well formed spherical aggregates with mean size of 0.45 μm consisting of 15±3 nm of nanocrystallite. The submicron-sized aggregates can induce the light scattering while nanocrystallites can increase the surface area for dye chemisorption. The incorporated nanoparticles in aggregates films results in better connectivity thus improves the transport properties. The breakthrough in hierarchical structured photoelectrode material could spur the development of higher performance DSC to challenge the high cost of commercially available silicon-based solar cells.

ABSTRAK

Sel suria pewarna (DSC) mempunyai kelebihan berbanding sel solar generasi lain seperti kebarangkalian untuk mengoptimumkan parameter, sesuai dengan substrat fleksibel, kos pengeluaran yang lebih rendah dan berfungsi walaupun dalam keadaan redup. Walau bagaimanapun, DSC masih mempunyai kecekapan prestasi yang rendah kerana persaingan di antara pembentukan dan penggabungan semula elektron.

Kajian ini bertujuan untuk membangunkan foto-elektrod TiO₂ berstruktur nanopartikel, agregat dan komposit agregat/nanopartikel yang menjanjikan prestasi DSC yang lebih baik. Selain itu, kesan dua parameter kritikal iaitu peratusan air dan suhu pengkalsinan pada morfologi dan mikrostruktur TiO₂ agregat yang disintesis turut dikaji menggunakan SEM, XRD dan BET. Filem foto-elektrod TiO₂ dihasilkan melalui teknik percetakan skrin pada kaca FTO, direndam dalam pewarna N719, dan dicantum dengan elektrod konduktif yang dilapisi mas putih membentuk DSC. Prestasi DSC kemudiannya dibandingkan berdasarkan penyerapan UV-Vis dan ciri-ciri *I-V* di bawah pencahayaan simulasi AM1.5 dengan 100 mW/cm² cahaya.

TiO₂ nanopartikel mencatatkan peratus kecekapan sebanyak 3.545%, manakala agregat yang disintesis dengan 0.9% air mencatatkan prestasi lebih tinggi, 3.915%. Suhu pengkalsinan yang optimum direkodkan pada 450°C. Prestasi yang lebih tinggi daripada 4% boleh dicapai dengan mencampurkan 20% nanopartikel dalam filem agregat yang disintesis menggunakan 0.9% air dan dikalsin pada suhu 450°C, menghasilkan agregat bulat dengan purata saiz 0.45 µm yang terdiri daripada nanokristal bersaiz 15±3 nm. Agregat bersaiz submikron mendorong penyerakan cahaya manakala nanokristal pula menambah luas permukaan untuk penyerapan pewarna. Nanopartikel yang dicampur memperbaiki penyambungan antara partikel seterusnya membantu pergerakan elektron. Kejayaan cemerlang dalam pembangunan bahan photo-elektrod berstruktur hierarki merangsang pembangunan DSC berprestasi tinggi untuk menyaingi sel suria berasaskan silikon yang jauh lebih mahal.

In compliance with the terms of the Copyright Act 1987 and the IP Policy of the university, the copyright of this thesis has been reassigned by the author to the legal entity of the university,

Institute of Technology PETRONAS Sdn Bhd.

Due acknowledgement shall always be made of the use of any material contained in, or derived from, this thesis.

© Siti Nur Azella binti Zaine, 2012

Institute of Technology PETRONAS Sdn Bhd

All rights reserved.

TABLE OF CONTENTS

LIST OF TABLES.....	xii
LIST OF FIGURES.....	xiii
ABBREVIATION & SYMBOL	xvii

Chapter

1. INTRODUCTION.....	1
1.1 The Need for Renewable Energy	1
1.2 Solar as Promising Renewable Energy	2
1.2.1 TiO ₂ -based Dye Solar Cell (DSC).....	5
1.3 Research Goals.....	6
1.3.1 Problem Statement.....	6
1.3.2 Research Objectives	8
1.3.3 Scope of Study.....	9
1.4 Outline of the Thesis	10
2. LITERATURE REVIEW.....	12
2.1 Photoelectrochemical solar cell (PEC).....	12
2.2 Dye Solar Cell (DSC).....	13
2.2.1 Structure of DSC	13
2.2.2 Operation Principle of DSCs	18
2.3 Structure Modification of TiO ₂ Photoelectrode Material.....	20
2.3.1 Reducing the Size of TiO ₂ Nanoparticles.....	21
2.3.2 One-Dimensional (1D) Structures of TiO ₂ Photoelectrode Material.....	23
2.3.3 Light Scattering Effect in TiO ₂ Photoelectrode Film	27
2.3.4 Submicrons-size TiO ₂ Aggregates.....	28
3. METHODOLOGY.....	31
3.1 Synthesis and Paste Preparation of TiO ₂ Photoelectrode Material	32
3.1.1 Synthesis of TiO ₂ Photoelectrode Material	32

3.1.2	Preparation of TiO ₂ Photoelectrode Paste	36
3.2	Characterization of Synthesized Samples	37
3.2.1	Thermogravimetric-Differential Thermal Analysis (TG-DTA).	37
3.2.2	Scanning Electron Microscopy (SEM).....	38
3.2.3	X-ray Diffraction (XRD)	39
3.2.4	Brunauer-Emmett-Tellet (BET) Analysis	41
3.2.5	UV-Visible (UV-Vis) Analysis	42
3.3	Cells Integration and Performance Verification	43
3.3.1	Test Cells Integration.....	43
3.3.2	Performance Verification	46
4.	RESULT AND DISCUSSION	49
4.1	Synthesis of TiO ₂ Nanoparticles for Dye Solar Cells (DSC).....	50
4.1.1	Physico-chemical Properties of P-25, TiO ₂ -MERCK and Synthesized TiO ₂ Nanoparticles.....	50
4.1.2	Optical Properties of P-25, TiO ₂ -MERCK and Synthesized TiO ₂ Nanoparticles	54
4.1.3	Performance of DSC based on P-25, TiO ₂ -MERCK and Synthesized TiO ₂ Nanoparticles.....	55
4.2	Development of TiO ₂ Aggregates Photoelectrode Material in Dye Solar Cells (DSCs).....	59
4.2.1	Effect of Water Content in Hydrolysis Process.....	60
4.2.2	Effect of Calcination Temperature	73
4.3	TiO ₂ Aggregates/Nanoparticles Composite Based DSC.....	84
4.3.1	Performance Verification	84
5.	CONCLUSION	92
5.1	Summary	92
5.1.1	Synthesis of TiO ₂ Nanoparticles for Dye Solar Cell	92
5.1.2	Development of TiO ₂ Aggregates Photoelectrode Material in Dye Solar Cell	93
5.1.3	TiO ₂ Aggregates/Nanoparticles Composite Based Dye Solar Cell.....	95
5.2	Conclusion.....	96

5.3	Benefit.....	97
5.4	Recommendation for Future Work	98
	REFERENCES	100
	APPENDIX	115
A.	Figure of Characterization Equipment	115
B.	List of Patent Filed/Publication/Exhibition & Award/Conference & Seminar	118

LIST OF TABLES

Table 3.1: Specification of P-25 (Degussa) and TiO ₂ -MERCK	33
Table 3.2: Condition adopted in the preparation of TiO ₂ aggregates samples	35
Table 3.3: Specification of photocurrent action spectra analysis	48
Table 4.1: Intensity (counts), FWHM, d-spacing, and crystallite size of anatase TiO ₂ at (<i>d</i> _{1 0 1}) plane while at (<i>d</i> _{1 1 0}) plane for rutile.....	54
Table 4.2: Photovoltaic properties of TiO ₂ nanoparticles as photoelectrode material.....	56
Table 4.3: Mean size and standard deviation of the synthesized TiO ₂ as a function of percentage of water content in ethanol solution.	62
Table 4.4: Intensity (counts), FWHM, d-spacing, and crystallite size of anatase TiO ₂ phase at (<i>d</i> _{1 0 1}) plane.....	65
Table 4.5: Surface area, pore volume and pore size of the synthesized TiO ₂ as a function of water percentage in ethanol solution.....	67
Table 4.6: Photovoltaic properties of the synthesized TiO ₂ aggregates as a function of water percentage in ethanol solution.....	68
Table 4.7: Intensity (counts), FWHM, d-spacing, and crystallite size of anatase at (<i>d</i> _{1 0 1}) plane while at (<i>d</i> _{1 1 0}) plane for rutile TiO ₂	76
Table 4.8: Surface area, pore volume and pore size of the synthesized TiO ₂ as a function of calcination temperature.....	79
Table 4.9: Photovoltaic properties of the synthesized TiO ₂ aggregates as a function of calcination temperature.....	80
Table 4.10: Comparison of photovoltaic properties of aggregates, composite and nanoparticles based DSC.....	86

LIST OF FIGURES

Figure 1.1: Annual electricity production from RE resources.....	3
Figure 1.2: Basic structure of a DSC.....	5
Figure 2.1: Schematic structure of a typical DSC structure	13
Figure 2.2: Chemical structure of N3, N719 and black dye	16
Figure 2.3: Photocurrent action spectra of N3, black dye and bare TiO ₂	16
Figure 2.4: Schematic energy diagram and operating principle of DSC.....	18
Figure 2.5: Illustration of electrons diffusion in photoelectrode films made up of nanoparticles and 1D structure.....	23
Figure 2.6: Schematic representation of possible mechanisms for the formation of multi-wall nanotubes through (a) helical scrolling, (b) curving and (c) direct production of a multi-walled nanotube.....	24
Figure 2.7: Schematic representation of light scattering in submicrometer-sized aggregates films	29
Figure 2.8: Illustrate the electrolyte diffusion through the external and internal pores of submicron-sized aggregates photoelectrode films	29
Figure 3.1: Flowchart of overall methodology	31
Figure 3.2: Flowchart of the process in producing TiO ₂ nanoparticles.....	33
Figure 3.3: Flowchart of the process in producing TiO ₂ aggregates	35
Figure 3.4: Flowchart of the process in preparing photoelectrode paste.....	37
Figure 3.5: Image of Perkin Elmer EXSTAR TG/DTA 6000 Series	37
Figure 3.6: Heating profile of TG-DTA analysis.	38
Figure 3.7: Image of Zeiss Supra 55VP Scanning Electron Microscopy	38
Figure 3.8: Image of X-Ray Diffractometer D8 Advance.....	39
Figure 3.9: Ideal peaks of TiO ₂ anatase phase based on PDF (21-1272)	39
Figure 3.10: Ideal peaks of TiO ₂ rutile phase based on PDF (21-1276).....	40
Figure 3.11: Image of Surface Area and Pore Size Analyzer model Micromeritics ASAP 2020.....	41

Figure 3.12: Image of UV-Vis Reflectance Spectrophotometer (Shimadzu UV-3150)	42
Figure 3.13: shows the image of UV-Vis Spectrophotometer (Shimadzu UV-3150)	42
Figure 3.14: Dimension of (a) working and (b) counter electrode	43
Figure 3.15: Temperature profile for firing CE and WE	44
Figure 3.16: Overall process flow of the assembly of DSC test cell	45
Figure 3.17: Image of assembled DSC	45
Figure 3.18: (a) Picture and (b) schematic diagram of Universal Photovoltaic Test System, Dyesol.....	46
Figure 3.19: Typical <i>IV</i> -curve of a DSC.....	47
Figure 4.1: TG-DTA curve of the synthesized TiO ₂ precursor at heating rate of 10 °C/min under flowing nitrogen gas.....	51
Figure 4.2: SEM images of (a) P-25 at 100KX (b) TiO ₂ -MERCK at 100KX and (c) synthesized TiO ₂ nanoparticles at 200KX.....	52
Figure 4.3: XRD pattern of (a) synthesized TiO ₂ (b) P-25 and (c) TiO ₂ -MERCK samples.....	53
Figure 4.4: Optical absorption of N719 dye absorbed on TiO ₂ films.....	55
Figure 4.5: <i>I-V</i> plot of DSC integrated with different types of photoelectrode material.....	56
Figure 4.6: UV-Vis absorption of desorbed-dye solution	58
Figure 4.7: Illustration of formation mechanism of TiO ₂ aggregates.....	60
Figure 4.8: SEM image of synthesized TiO ₂ with 0.9 vol% of H ₂ O at (a) 10 KX (b) 150 KX and (c) aggregates size distribution curve	61
Figure 4.9: SEM image of synthesized TiO ₂ with 1.8 vol% of H ₂ O at (a) 10 KX (b) 150 KX and (c) aggregates size distribution curve.....	61
Figure 4.10: SEM image of synthesized TiO ₂ with 2.7 vol% of H ₂ O at (a) 10 KX (b) 150 KX and (c) aggregates size distribution curve	62
Figure 4.11: SEM image of synthesized TiO ₂ with 3.6 vol% of H ₂ O at (a) 10 KX (b) 150 KX and (c) aggregates size distribution curve	62

Figure 4.12: XRD pattern of synthesized TiO ₂ photoelectrode material hydrolyzed with (a) 0.9 vol% (b) 1.8 vol% (c) 2.7 vol% and (d) 3.6 vol% of water in ethanol solution.	64
Figure 4.13: Nitrogen adsorption and desorption isotherm of synthesized TiO ₂ aggregate at different water percentage.	66
Figure 4.14: Pore size distribution of synthesized TiO ₂ aggregate at different water percentage.....	66
Figure 4.15: <i>I-V</i> curve of synthesized TiO ₂ aggregates at various water percentage in ethanol solution.	68
Figure 4.16: Optical absorption spectra of synthesized TiO ₂ aggregates films.....	70
Figure 4.17: Photocurrent action spectra of the electrodes with synthesized TiO ₂ aggregates structure.....	71
Figure 4.18: LHE versus wavelength	72
Figure 4.19: SEM image of synthesized TiO ₂ aggregates calcined at (a) 400°C (b) 500°C (c) 600°C and (d) 700°C for 2 hours at 100 KX of magnification.....	74
Figure 4.20: XRD pattern of synthesized TiO ₂ photoelectrode material subjected to various calcination temperatures (a) 400°C (b) 500°C (c) 600°C and (d) 700°C	76
Figure 4.21: Nitrogen sorption isotherm of synthesized TiO ₂ aggregate at different calcination temperature.	78
Figure 4.22: Pore size distribution of synthesized TiO ₂ aggregate at different calcination temperature.	78
Figure 4.23: Dependence of short circuit current on calcination temperature	81
Figure 4.24: Dependence of performance efficiency of DSC on calcination temperature.....	81
Figure 4.25: Absorption spectra of the desorbed-dye from the TiO ₂ photoelectrode material at difference calcination temperature.	83
Figure 4.26: Dependence of short-circuit current on percentage of nanoparticles in photoelectrode films.....	87
Figure 4.27: Dependence of performance efficiency of integrated DSCs on percentage of nanoparticles in photoelectrode films.....	87

Figure 4.28: UV-Vis spectra of desorbed dye at different percentage of nanoparticles	89
Figure 4.29: Nominal optical spectra of dyed TiO ₂ aggregates films mixed with different percentage of nanoparticles	89
Figure 4.30: Illustration of light travelling in photoelectrode TiO ₂ films of (a) aggregates and (b) nanoparticles structure	91
Figure 5.1: Dye solar module of size 100 mm x 180 mm	98

ABBREVIATION & SYMBOL

Abbreviations

AAM	Anodic alumina membrane
AIST	Advanced Industrial Science and Technology
AM	Air Mass
BET	Brunauer-Emmett-Tellett
Biogen	Biomass Power Generation & Cogeneration Project
BJH	Barrett-Joyner-Halenda
CE	Counter electrode
CHP	Combine heat to power
CIGS	Copper indium gallium diselenide
CPO	Crude palm oil
CTAB	Cetyltrimethylammonium bromide
CVD	Chemical vapor deposition
DSC(s)	Dye solar cell(s)
DTA	Differential Thermal Analysis
FSM	Full scale model
FTO	Fluorine-doped tin oxide
FWHM	Full-width half maxima
GEF	Global Environment Facility
HOMO	highest occupied molecular orbital
IEA	International Energy Agency
IPCC	Intergovernmental Panel on Climate Change
IPCE	Incident Photon to Current Conversion Efficiency
LHE	Light harvesting efficiency
LUMO	Lower unoccupied molecular orbital
MBIPV	Malaysian Building Integrated Photovoltaic
MLCT	Metal-to-ligand charge transfer
PDF	Powder diffraction file

POME	Palm oil effluents
PSC(s)	Photoelectrochemical solar cell(s)
RE	Renewable energy
RTIL(s)	Room temperature ionic liquid(s)
SEM	Scanning Electron Microscopy
SMART	Specific, measurable, achievable, realistic and time-specific
TG	Thermogravimetry
UNDP	United Nations Development Programme
UPTS	Universal Photovoltaic Test System
UV-Vis	Ultraviolet-Visible
WE	Working electrode
XRD	X-ray diffraction

Symbols

β	line broadening
D_n	diffusion coefficient of electron
d	crystallite size
d_{hkl}	interplanar spacing between the planes
FF	fill factor
hr(s)	hour(s)
$h\nu$	photon energy
η	efficiency
I_{max}	maximum current
I_{sc}	short circuit current
λ	wavelength
S	sensitizer
S^*	excited energy state of the sensitizer
S^+	oxidized state of the sensitizer
St_{dev}	standard deviation
T_c	crystalline temperature
V_{max}	maximum voltage
V_{oc}	open circuit voltage

CHAPTER 1

INTRODUCTION

1.1 The Need for Renewable Energy

Fossil fuels are the main global energy source and are predicted to remain the dominant source of energy to 2030, accounting for 83% of the overall increase in energy demand between 2004 and 2030 [1]. As in Malaysia, the energy sector had been highly dependent on a single source of energy (oil) until the implementation of four-fuel diversification strategy; oil, nature gas, hydro and coal in 1980 [2]. This strategy was implemented after the occurrence of two international oil crisis and quantum leaps in prices in the year 1973 and 1979 [2]. As a direct consequence of this strategy, the contribution of oil to the energy mix has dropped drastically from a high 90% dependence in 1980 to less than 10% in 2003 [2]. However, using conventional non-renewable energy such as fossil fuels (oil and coal) and natural gas in the energy mix has lead to serious energy crisis; finite depletion of resources which can cause severe supply disruption and associated price escalation [1, 2] and secondly, the emission of greenhouse gasses, that raise the issue of climate change [1-5].

As predicted by the Intergovernmental Panel on Climate Change (IPCC), the global energy demand will rise by a factor of five over the next century, from 10 TW to nearly 46 TW by 2100 [5]. Burning of this fossil fuel has raised the energy-related carbon dioxide (CO₂) emission issues [5-8]. The International Energy Agency (IEA) forecasts that the world will face an increment of 14.3 Gt CO₂ over the 2004 level by 2030 [7]. According to Boercker et. al., one of the major consequences of increasing anthropogenic CO₂ is the rise of almost 6°C of the average global temperature by the year 2100 [5]. Such a dramatic rise would cause thermal expansion of the oceans as well as melting of the polar ice caps, resulting in floods and storms.

In the past few years, Malaysia also has experienced a number of such effects. For example, the floods in Johor on Peninsular Malaysia from December 2006 to January 2007 were the worst in 100 years [4]. These floods caused 90,000 people to leave their homes and killed 17 people. This natural event resulted in the country to suffer financial losses of about RM 6 billion. In order to combat this impending energy crisis, and the catastrophic consequences of global warming, carbon-free alternative energy sources need to be used to meet the ever increasing global energy demand.

However, renewable energy (RE) is believed to be able to meet the global energy demand and lead to cumulative greenhouse gas savings equivalent to 220 to 560 Gt of CO₂ between 2010 and 2050 [9]. As a signatory of United Nation Convention on Climate Change and the Kyoto Protocol, Malaysia has taken a drastic approach in reducing the emissions of green house gasses by adding RE resources mainly hydro, biomass, and solar as the fifth source of fuel in the 8th Malaysia Plan (2001–2005) [2-4]. In addition to that, the government had announced the National Renewable Energy Policy and Action Plan in mid 2010, with a goal of increasing renewable energy from 1% to 5.5% of electricity supply by 2015 [10].

1.2 Solar as Promising Renewable Energy

Malaysia's indigenous RE sources include palm oil biomass waste and palm oil mill effluents, hydro, solar power, solid waste, wind energy and geothermal [11]. Out of all, biomass waste and biogas is one of the potential RE in Malaysia since Malaysia is covered by about 4.3 million hectares of palm oil crop alone; the second world largest producer of crude palm oil (CPO) [12]. The palm oil planted area has grown by 3.4% which is 4.85 million hectares in 2010 with 16.99 million tonnes of CPO were produced compared to 15.8 million tonnes in 2006 [11, 13]. With abundant sources available, the palm oil industry is likely to become ever more prominent in adopting renewable energy. In 1999, a project known as Biomass Power Generation & Cogeneration Project (Biogen) was started with the ultimate desired outcome to implement a full scale model (FSM) of biomass based power generation with

combine heat to power (CHP) in conjunction with a palm oil effluents (POME) derived biogas system [1]. The project was expected to produce an average of 665MW capacity by utilizing 20.8 million tonnes of biomass residues and 31.5 million m³ of POME. Whilst the concept of biomass based CHP generation for sale to the grid or other consumers is well accepted, lack of experience and a number of barriers have hindered its development [1].

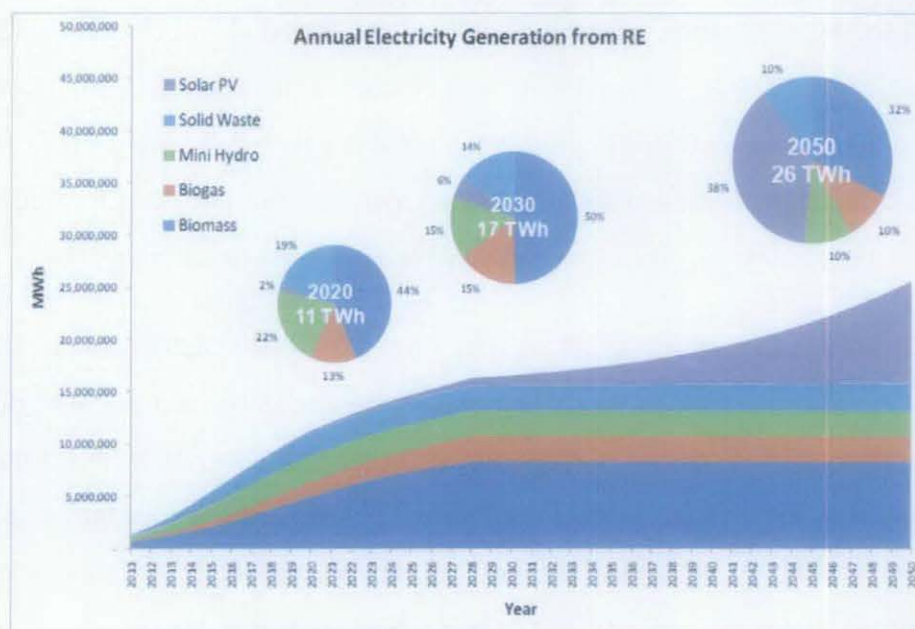


Figure 1.1: Annual electricity production from RE resources [11].

Besides the biomass, the climatic conditions in Malaysia are favorable for the development of solar energy as another major contender for RE. Being near the equator, Malaysia receives solar radiation ranging from as low as 6.0 kwh/m² in the months of August and rise to as high as 6.5 kwh/m² in the months of January [2]. In 2005, the government of Malaysia with co-financing from Global Environment Facility (GEF) disbursed through United Nations Development Programme (UNDP) has embarked on a project known as Malaysian Building Integrated Photovoltaic Technology Application Project (MBIPV) [2, 3]. The aim of the project was to induce an increase of BIPV application by 330% from baseline in 2005 and reduce 20% of the long-term cost of solar photovoltaic technology by year 2010 through the development of a sustainable and widespread local market [11]. Figure 1.1 shows the annual electricity production from RE resources under specific, measurable, achievable, realistic and time-specific (SMART) target introduce under MBIPV

project. Based on the figure, solar energy will be the most demanding source of RE by the year 2050, as it is the only unlimited source of energy with significant capacity available in the country [11].

Solar energy can be classified into three different generations where the first solar generation was developed by Chapin, Fuller and Pearson at the Bell Telephone Laboratories in the mid 1950's [14]. About 86% of current solar market was dominated by this generation which is mainly silicon based solar cells. This situation is due to the high efficiency where the highest efficiency recorded for a laboratory cell is 24.7% whilst commercial crystalline silicon solar panels is about 15% [15]. The first generation solar cells demand for high purity Si thus the need for high-level semiconductor technology, and as such expensive and very capital intensive.

Second solar generation consist of thin film solar cells such as as amorphous silicon (a-Si), cadmium telluride (CdTe), copper indium gallium diselenide (CIGS), and thin film crystalline silicon. Comparing with the first generation, thin film solar cells are significantly cheaper to produce than the first generation cells but have lower efficiencies [14-16]. In addition, second generation solar cells are more flexible, lightweight, aesthetically pleasing solar innovations such as solar shingles and solar panels that can be rolled out onto a roof or other surface [16].

The third generation is the cutting edge of solar technology beyond the silicon-based cells. This technology is still in the research phase and generally comprises of non-semiconductor technologies (polymer-based cells and biomimetics), quantum dot technologies, tandem/multi-junction cells, hot-carrier cells, dye solar cells (DSCs) and up-conversion technologies [17, 18]. The advantage of the third generation over other generation is that they offer very high possibilities for improving parameters such as charge generation, separation, molecular mass, band gap, molecular energy levels, rigidity, and molecule-to-molecule interactions [17, 18]. Furthermore, the materials are also compatible with flexible substrates and have lower production cost with almost 30-40% compared to the first two generation [17]. Despite all of these great advantages, organic solar cells suffer from very low efficiencies of just 5% on an average and thus limit their current usage. Among the third generation solar

technology, DSCs are currently the most efficient third-generation solar technology and work well even in diffuse light [16].

1.2.1 TiO_2 -based Dye Solar Cell (DSC)

Dye solar cell (DSC), also known as Grätzel cell, is an artificial photosynthesis where a dye analogous to chlorophyll absorbing light, thus generating electrons which enter the conduction band of a high surface area semiconductor film and travel along an external circuit, producing electricity [19-23]. Unlike the conventional PV, the basic structure of DSC (Fig. 1.2) comprises of a layer of photo-electrode material, photosensitized by a monolayer of dye and assembled in between a sandwich layer of transparent electrically conducting substrate and conducting catalytic substrate. An electrolyte, based on an Iodide/Tri-iodide redox system is filled in between the layer gap of photosensitized titania and transparent electrically conducting catalytic substrate.

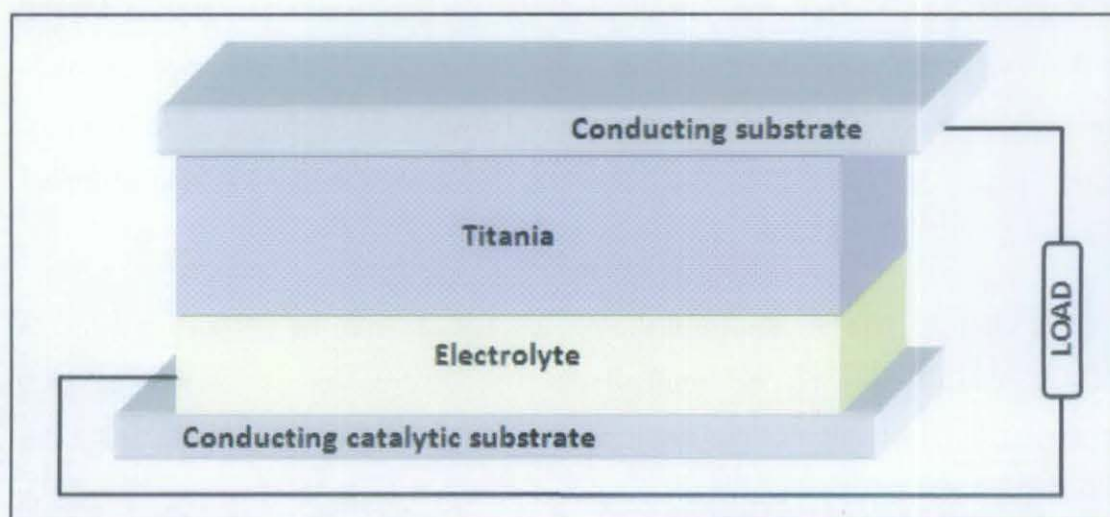


Figure 1.2: Basic structure of a DSC.

DSC has been discovered as early as 1970's [5, 24]. However the efficiency of DSC was too low (approximately 1%), until 1991, where Grätzel and O'Regan had found the breakthrough in obtaining higher efficiency by modifying the morphology of the wide band gap semiconductor from a smooth surface to a $10 \mu\text{m}$ thick of optically transparent TiO_2 nanoparticle film [5, 25]. Because of the high surface area

of the semiconductor film and the ideal spectral characteristics of the dye, the device harvests a high proportion of the incident solar energy flux (46%) and shows exceptionally high efficiencies for the conversion of incident photons to electrical current (more than 80%) [25]. Up to date, the conversion efficiency of DSC has achieved 11.1%, which is the highest DSC efficiency recorded so far and confirmed by National Institute of Advanced Industrial Science and Technology (AIST) [26].

1.3 Research Goals

1.3.1 Problem Statement

In the presence of sunlight, the photons strike the dyes with enough energy to create an excited state of the dye, resulting in generating electron which can be injected directly into the conduction band of the TiO_2 . The original state of the dye is subsequently restored by the electrons donation from the electrolyte (regeneration process) [19-21, 23]. However, in real condition, the generated electrons could travel in the reverse direction and recombine with the oxidized dyes before regeneration process take place. The dynamic competition between the electrons generation and recombination has found to be the bottleneck restricting the development of higher efficiencies of DSCs [27-29].

The electron-transfer rate from the photosensitizer into the conduction band of TiO_2 depends largely on the configuration of the dyes on the surface of TiO_2 photoelectrode material and the band gap between the lower unoccupied molecular orbital (LUMO) level of the dyes and the conduction band level of the TiO_2 [23]. Thus, one possible way to overcome the competition between electrons generation and recombination is by modifying the morphology and surface structure of the photoelectrode material which is critical in holding the dyes and transporting the electrons.

In most conventional DSCs, the photoelectrodes are made up of TiO_2 nanoparticles with sizes of 10–20 nm which have an advantage in providing larger surface areas and have a greater number of contact points, allowing for greater dye

adsorption [30]. However, the size is much smaller than the wavelength of visible light. The film is thus transparent with little light scattering [31]. In addition, smaller nanoparticles exhibit a larger number of grain boundaries where electrons need to pass through, which results in a higher probability of electron trapping [32-34]. In the event of competition between electron generation and recombination process, pioneering a rapid electron transport in the porous TiO₂ medium is important to obtain an efficient electrons collection by the conducting substrate [31, 35].

Fabrication of films by one-dimensional nanostructures such as nanotubes and nanowires array has proven to be an effective way to facilitate electron transport [31, 35, 36]. Besides, the nanostructures could also introduce light scattering, resulting in an enhancement of light harvesting. Mor et al. found that highly ordered nanotubes arrays show superior electron lifetimes and provide excellent pathways for electron percolation in comparison to nanoparticulate system [37]. The cell with a 360 nm thickness has generated a photocurrent of 7.87 mA/cm² with a conversion efficiency of 2.9%. Even though highly ordered nanostructures array show fast electron transport, the limited density and thickness may prevent a much higher efficiency [38].

Another approach to improve the conversion efficiency is by integrating larger particles (>100 nm) to introduce light scattering effect [39]. Experimentally, light scattering efficiency has shown a significant improvement in DSC performance. The resonant scattering most likely to occur when the size of the particles is comparable with the wavelength of the incident light [27]. Nevertheless, the introduction of larger particles has the drawback of reducing the internal surface area for dye chemisorptions, resulting in low light harvesting. On the other hand, utilizing smaller nanoparticles (~10 nm) have a great advantage in adsorbing much more sensitizer, yet higher efficiency is difficult to be achieved due to the low light harvest in the red region [33, 34].

A recent reported hierarchically structured film of ZnO aggregates, which provides the photoelectrode with both large surface area and efficient light scattering, possess more than double the conversion efficiency obtained for dispersed ZnO nanocrystallite [27-29, 38-40]. The idea is that, the submicron-size spherical

aggregates could introduce light scattering effect that can results in extending the distance travelled by the light radiance causing more electrons to be generated. Conversely, the primary nanocrystallites which made up the aggregates could ensure the desired high internal surface area for dye chemisorptions. However, when similar approach was employed to TiO₂, it is hampered by the availability of synthesis method in the production of desired nanostructures [40]. Thus, the work here focuses on the development of TiO₂ aggregates made up of nanocrystallite structures with high surface area and better scattering efficiency. This research will also investigate the effect of the relative aggregates/nanoparticles composite ratio on the performance of DSCs.

1.3.2 Research Objectives

Despite the big number of the previous research and study related to the development of TiO₂ as photoelectrode material in DSCs, the right photoelectrode structure for DSC remains elusive. Thus, on the whole, the aim of this research is to develop TiO₂ photoelectrode material namely nanoparticles, aggregates and aggregates/nanoparticles composite with desired characteristic that can exhibit better performance efficiency of DSC. This can be achieved by the following specific objectives:

- I. Synthesis of TiO₂ nanoparticles photoelectrode material with better properties compared to commercially available TiO₂ namely P-25 (Degussa) and TiO₂-MERCK.
- II. Synthesis of submicron-sized TiO₂ aggregates made up of nanocrystallites and optimization of the synthesis parameters namely percentage of water content and calcination temperature that can influence the physico-chemical properties and the performance of the synthesized TiO₂ aggregates when used as the photoelectrode of DSC.
- III. Development of TiO₂ aggregates/nanoparticles composite photoelectrode material and determination of the most favorable aggregates/nanoparticles composite ratio in achieving higher efficiency of DSCs.

1.3.3 Scope of Study

The main aim of the study is to develop TiO₂ photoelectrode material namely nanoparticles, aggregates and aggregates/nanoparticles composite and determine the structured properties relationship that can increase the efficiency of DSC. To achieve the main aim and the specific objectives of this research, the scope of the work includes the following tasks.

Before conducting detailed research, it is important to understand the basic structure, operation principle, factors that influence the performance as well as the bottleneck of a DSC. Therefore, this research was initiated by conducting a thorough literature review on the DSC generally and the previous research done on various TiO₂ photoelectrode structures, which have been the heart of DSC. The morphology of TiO₂ film is a major variability factor in DSCs performance, mainly because of its influence in the electron recombination rate. A relatively new and exciting research field in semiconductor morphology is the use of nanostructures, namely nanorods, nanotubes, nanowires, one-dimensional structures as well as aggregates. Despite the large number of past research on developing TiO₂ nanostructures, there is still no optimum structures obtained. Therefore, this study has been carried out to present reliable and optimized nanostructure TiO₂ for better DSC performance.

Based on the research objectives, the second task involved synthesizing TiO₂ nanoparticles and submicron-sized TiO₂ aggregates composing of nanocrystallites by way of sol method. Two most influenced parameters have been identified for investigation; percentage of water content used during synthesis step and calcination temperature. The physico-chemical properties of the synthesized samples were evaluated through thermogravimetric-differential thermal analysis (TG-DTA), scanning electron microscopy (SEM), X-ray diffraction (XRD) and BET method. UV-Visible spectroscopic was used to investigate the optical properties of the integrated TiO₂ photoelectrode films.

The third task involved integration of TiO₂ films into test cells. Films with an area of about 0.88 cm² and thickness of about 12 μm were deposited onto FTO-coated glass substrates (working electrodes) using screen printing technique and soaked

overnight in N719 dye. The working electrodes were then assembled into sandwich layer with counter electrodes which have been printed with platinum. An electrolyte, iodide/tri-iodide redox system was injected in between the electrodes. The performance verification of nanoparticles-based, submicron-sized aggregates-based as well as nanoparticles/aggregates composite-based DSCs were examined under a standard 100 mW/m^2 -illuminant Xenon lamp and a radiation source of AM-1.5.

The final task of this research involved the analysis of the results obtained from the experimental work. Detailed discussion of the analysis is presented. Finally, the main findings of this study are summarized in a conclusion.

1.4 Outline of the Thesis

The thesis is arranged in 5 chapters where the first chapter gives an introduction to the thesis by describing the background of the study, problem statement, objective and scope of study as well as the outline of the thesis.

Chapter 2 establishes the background necessary to understand the structures and operation principles of a DSC in detail. In this chapter also, there were reviews on the significance of having anatase phase as the active sites for dye chemisorptions as well as the previous published research on the approach taken in overcoming the competition between photon generation and recombination on materials science view. This includes the diverse study on improving the internal surface area, optimizing electrons transport, considering light scattering effect as well as introducing new yet exciting aggregates morphology.

Chapter 3 describes the research methodology including the synthesis of the TiO_2 nanoparticles and aggregates, photoelectrode paste preparation, characterization technique applied in this study and also DSCs integration as well as performance verification. The characterization technique comprises of thermal analysis for the precursor, phase identification, estimation of crystallite size and surface area as well as optical properties of the prepared photoelectrode film.

Chapter 4 presents the research discovery and achievement. These include the development of better performance TiO_2 nanoparticles as compared to the commercially TiO_2 , the optimum condition for synthesizing TiO_2 aggregates and the optimum ratio for nanoparticles/aggregates composite in obtaining higher performance efficiency of DSCs.

Chapter 5 summarizes the research finding and concludes the whole research study. This chapter also highlights the novelty, benefits of the research finding and suggests some possible future research directions that can further improve the efficiency of the DSC.

CHAPTER 2

LITERATURE REVIEW

2.1 Photoelectrochemical solar cell (PEC)

Photoelectrochemical solar cell (PEC) consists of a semiconducting photoanode and a metal cathode immersed in an electrolyte which generate electricity through conversion of light energy [41]. In theory, there are three preferences for the arrangement of photoelectrodes in the assembly of PEC [41]:

- Photoanode of a *n*-type semiconductor and a cathode made of metal;
- Photoanode made of a *n*-type semiconductor and a photocathode made of a *p*-type semiconductor;
- Photocathode made of a *p*-type semiconductor and an anode made of metal.

Several semiconductor materials namely single-crystal and polycrystal forms of *n*- and *p*-Si, *n*- and *p*-GaAs, *n*- and *p*-InP, and *n*-CdS, have been used as photoelectrodes [23]. Nevertheless, photocorrosion of the electrode under irradiation is inevitable, resulting in poor stability of the cells. Consequently, other oxide semiconductor materials such as TiO₂, ZnO and SnO₂ are primarily used in the PEC to achieve substantial efficiency due to their stability under irradiation in electrolyte solution [41]. However, stable oxide semiconductors are poor in absorbing visible light due to their relatively wide band gap. Sensitization of the oxide semiconductor photoelectrode material with photosensitizers, such as organic dyes makes it an attractive material for photoelectrochemical applications, namely dye-sensitized solar cells (DSCs).

2.2 Dye Solar Cell (DSC)

2.2.1 Structure of DSC

A typical structure of DSC compose of transparent working electrode coated with photoelectrode material, ruthenium (Ru) complex dye, iodide/tri-iodide redox couple electrolyte, platinized counter electrode and sealant. The schematic structure of a typical DSC is illustrated in Figure 2.1.

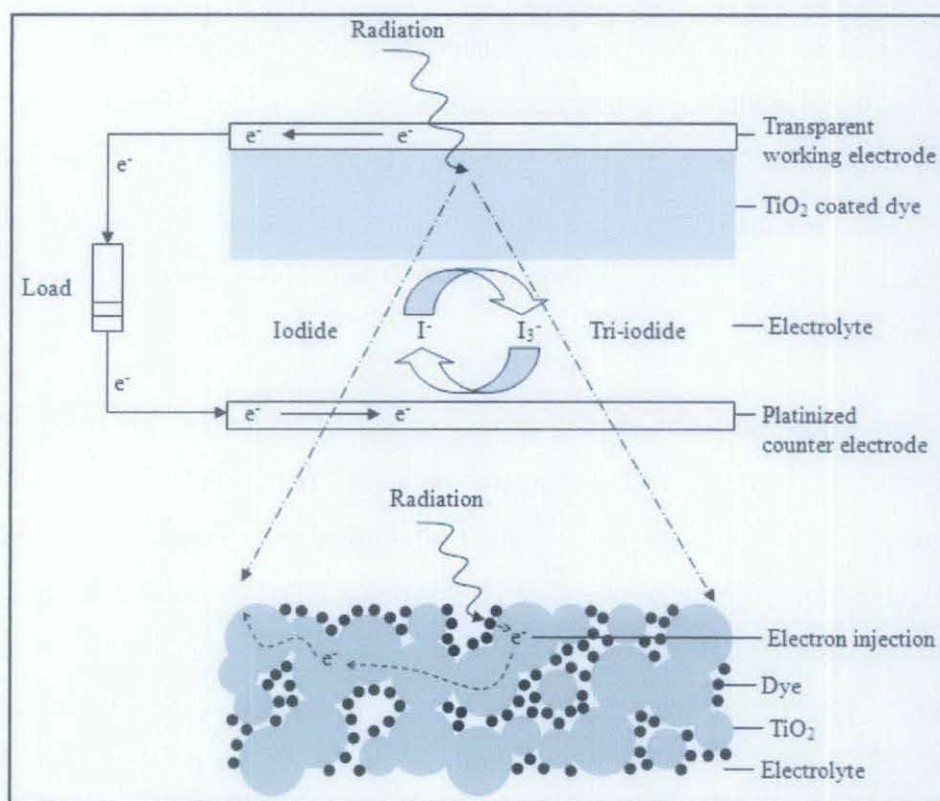


Figure 2.1: Schematic structure of a typical DSC structure [23].

2.2.1.1 TiO₂ Photoelectrode Material

The heart of DSC lies on the photoelectrode semiconductor material which is critical in holding the dye and transporting the electrons. Over the recent years, the developments of mesoscopic oxide or chalcogenide nanoparticles as photoelectrode material in DSC have attracted considerable attention. Several porous oxide semiconductor materials i.e. zinc oxide (ZnO) [19, 23, 27-29, 39, 42, 43], niobium pentoxide (Nb₂O₅) [19, 23, 42], stannous oxide (SnO₂) [23, 42] and indium oxide (In₂O₃) [23, 42] have been intensively studied as potential photoelectrode in DSC,

however nanocrystalline TiO₂ shows the best performance [23, 42]. In addition, TiO₂ also have a good chemical stability, nontoxic, widely available and inexpensive [19-21, 23]. Other materials such as Si, GaAs, InP and CdS have also been used as photoelectrode material yet decomposed under irradiation thus inherent toxicity concerns [23].

Sayama et al. [42] systematically studied the photoelectrochemical characterization of different types of porous semiconductor films such as TiO₂, Nb₂O₅, ZnO, SnO₂, In₂O₃ and WO₃ with an adsorbed layer of ruthenium (II) complex dye as a sensitizer. The photoelectrode materials were spread on conducting glass using doctor blade technique with an area of about 1 cm² and thickness of about 6-8 μm. They found that the open-circuit photovoltage (V_{oc}) of the Nb₂O₅ cell was the highest of all semiconductor cells followed by TiO₂ cells. Nevertheless, TiO₂ semiconductor cells showed much higher short-circuit photocurrent (I_{sc}) (0.73 mA) compared to others.

An exponential growth of research activities have been observed in the development of various TiO₂ nanostructures as photoelectrode materials in application of DSC. Some of the common structures are nanoparticles, nanotube, nanorods, nanotubes and nanowires. The properties of TiO₂ nanostructures are closely related to the material content, chemical composition, structures as well as surface morphology. The nanostructures of TiO₂ can be modified by controlling the synthesis parameters like precursor, hydrothermal growth temperature, addition of binder, use of template and calcination condition. Controlling this entire key parameters will produce an optimum characteristic of developed nanostructures material such as porosity, pore size distribution, active surface area, electron percolation as well as light scattering effect [19].

The surface morphology, active area, porosity and pore size of the photoelectrode film have a significant effect on the electron transport properties [36]. To date, there are many approaches studied in order to optimize the properties of TiO₂ as photoelectrode material. Optimizing the crystallinity and crystallite composition of developed TiO₂ photoelectrode materials is believed to lead to a significant improvement of DSCs. Tang et al [44] did study on the performance comparison of

amorphous and highly crystalline TiO₂-based DSC. For the same film thickness, they found that highly crystalline TiO₂ film is indeed more efficient than amorphous film in adsorbing the dye. Moreover, the shapeless amorphous TiO₂ particles cannot provide a homogeneous mesoporous inner structure for the film, which is the primary disadvantage to the performance of DSCs. Therefore, an amorphous TiO₂ film is usually avoided to be used in DSCs application.

Frequently, there are two crystalline phase of TiO₂ exist; anatase and rutile. Synthetic anatase is desirable for photocatalyst and photoelectrode material. Even though rutile is more stable, yet according to O'Regan and Gratzel [25], anatase structure plays a crucial role in a number of charge-separation device such as DSC application. Besides, TiO₂ with anatase phase possesses high band gap energy (3.2 eV) compared to rutile phase (3.0 eV) [45]. Park et. al [46] did a comparative study on the rutile and anatase-based solar cells. At an identical film thickness (11.5 μm), a rutile-based DSC exhibit 30% lesser short-circuit current density compared to anatase-based DSC. However, both cells show an identical value of open-circuit voltage (730 mV) at 1 sun light intensity. They found that, smaller surface area per unit volume and slower electron transport was the factors limiting an even higher performance of rutile-based DSC.

The most predominant morphology of anatase particles is bipyramidal exposing well-developed (d_{101}) facets [19] corresponding to the anatase crystal planes with the lowest surface energy. In general, a dye molecule is anchored to TiO₂ surface by functional groups, such as carboxylate, hydroxamate or phosphonate moieties. Only by forming a strong coordinative bond with the TiO₂ surface ions, can the dye efficiently inject photo-electrons into the conduction band of TiO₂ [44]. A conventional DSC is integrated with 10 μm film thickness of 10-30 nm size TiO₂ nanoparticles which account for an actual surface area of 1000 cm² [23].

2.2.1.2 Ruthenium (Ru) Complex Photosensitizer

N3 and N719 are two most successful Ru(II) complex dye reported by Grätzel and co-workers in 1993 accounting for 10.0% and 11.2% of performance efficiency of DSCs, respectively [47, 48]. These dyes have comparable capability in converting the

incident photons to current in the range of 800 nm, but N719 could help in increasing the cell voltage [49]. In 1997, a new dye known as black dye was established, with a capability to absorb wavelength up to 920 nm (near infrared region) [49, 50]. Figure 2.2 shows the chemical structure of N3, N719 and Black dye as reported by Vougioukalakis et. al [49] whilst Figure 2.3 show the photocurrent action spectra of N3 and black dye compared with bare TiO₂ [48].

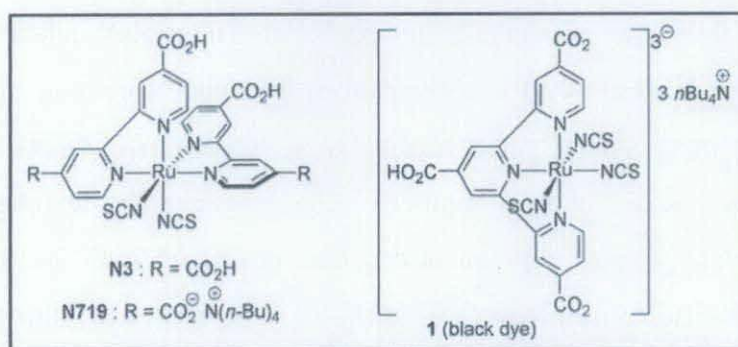


Figure 2.2: Chemical structure of N3, N719 and black dye [49].

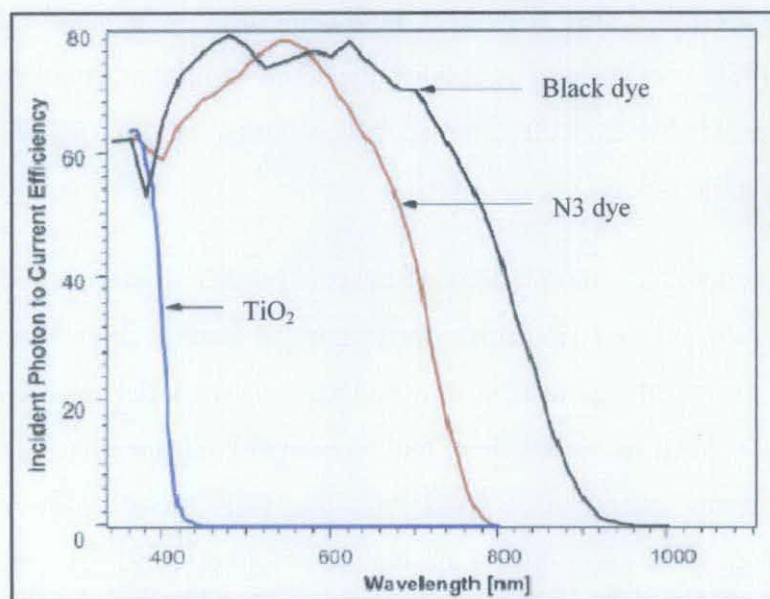


Figure 2.3: Photocurrent action spectra of N3, black dye and bare TiO₂ [48].

Since then, a series of modification on the earlier dye have been studied. The studies are focus on the several criteria which is believed to enhance the performance of the synthetic dyes such as [49, 51-55]:

- i. strong and broad absorption range extending from visible to the near-infrared region;
- ii. chemically stable under sunlight exposition;
- iii. higher reduction potential compared to the band edge of oxide semiconductor photoelectrode materials to increase electron injection efficiency;
- iv. strong electronic coupling dye;
- v. low oxidation potential compared to redox potential for faster regeneration process; and
- vi. reduce deactivation of excited dye under emission of light or heat;

2.2.1.3 Electrolyte

In a DSC, electrolyte is responsible for regenerating the dye and transportation of electron between the TiO₂ photoelectrode and the counter electrode [23, 49, 56]. Iodide/tri-iodide redox couple is the most efficient electrolyte [49]. To date, the diluted iodide/tri-iodide (I⁻/I₃⁻) redox couple in an organic electrolyte namely acetonitrile is the most efficient electron mediator in DSC [49]. Principally, nonprotonic solvents such as acetonitrile, propionitrile, methoxyacetonitrile and propylene carbonate are used to dissolve mixture of 0.1-0.5 M of iodide (e.g. LiI, NaI, KI, tetraalkylammonium iodide (R₄NI), and imidazolium-derivative iodides) and 0.05-0.1 M of I₂. The counter cations of iodide such as Li⁺, Na⁺, K⁺, and R₄N⁺ plays an important role in determining the performance of an integrated DSC due to their ion conductivity difference in electrolyte or adsorption on the TiO₂ surface, which results in a shift of the conduction-band level of the TiO₂ electrode [57, 58]. Even though, iodide/tri-iodide redox couple system shows a promising result, the high volatility of the solution had raise sealing-related problems.

Due to the problem, new room temperature ionic liquids (RTILs) and solid state-based electrolyte have been employed. RTILs is chemically and thermally stable, negligible vapor pressure, non-flammable, high ionic conductivity and wide electrochemical window electrolyte [56, 59]. 1,3-dialkylimidazolium iodide is the

most efficient ionic liquid-based electrolyte with 8.2% of DSCs performance efficiency [56]. In contrast, solid-state electrolyte employs a p-type semiconductor layer [20, 56] with the highest efficiency achieved so far of 7.7%. This was reported by Wang et. al to be due to the utilization of chemically cross-linked polymer gel electrolyte with a dendritic structure [60].

2.2.1.4 Platinized Counter Electrode

A thin layer of platinum film basically deposited on the counter electrode side of DSC will acts as an efficient catalyst for the reduction of tri-iodide ions [23]. However, platinum is an expensive catalyst. There were efforts in replacing the platinum with carbon as catalytic counter electrode. Kay and Gratzel did study on the utilization of carbon black, graphite powder and nanocrystallite TiO_2 particles as carbon electrode in DSC [61]. They found a comparable performance of carbon electrode and conventional Pt electrode as catalyst for tri-iodide reduction.

2.2.2 Operation Principle of DSCs

The working scheme of a typical DSC is illustrated in Figure 2.4, showing TiO_2 layer sensitized with dye deposited in a conductive electrode. Under illumination, the device constitutes a regenerative and stable photovoltaic energy conversion system.

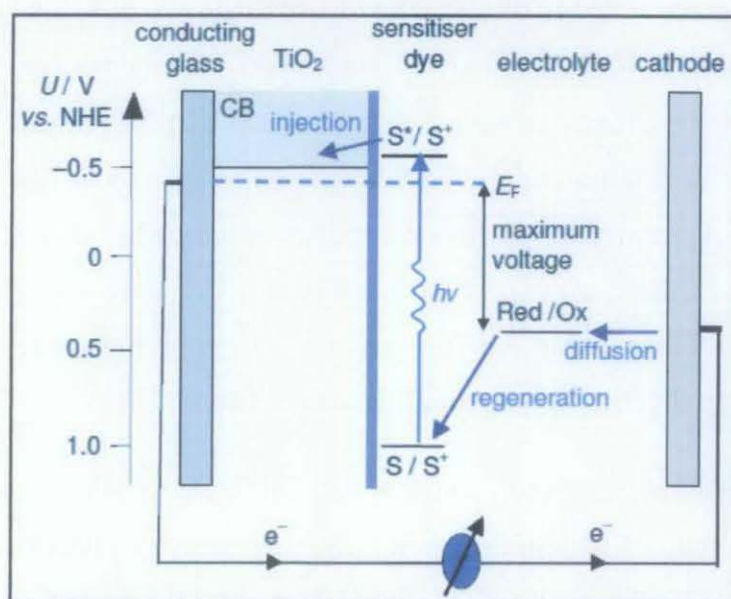
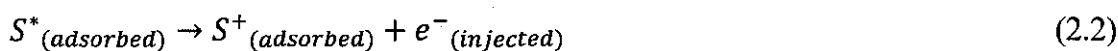


Figure 2.4: Schematic energy diagram and operating principle of DSC [62].

When the sunlight strike the photosensitized dye on the surface of TiO₂, the dye molecule absorbs the energy of photon and transform to the excited state (S*). The excitation of the dye is followed by injection of the resulting electrons into the conduction band of the TiO₂, leaving dye in the oxidized state (S⁺) as summarized in the equilibrium reaction (2.1) and (2.2) [20, 21, 23, 63] where $h\nu$ is the photon energy.



Regeneration of original state of the dye electrons occur through donation from iodide/tri-iodide redox electrolyte in contact with the dye (Equation 2.3 and 2.4) [20, 21, 23, 63].



The injected electrons collected on the working electrode side, travel along the external circuit to power the load and then flow to the counter electrode side. The electrons that reach counter electrode side will reduce the tri-iodide into iodide. The voltage generated is equal to the difference between the Fermi level of the electron in the solid TiO₂ and the redox potential of the electrolyte [39, 64].

Under real reaction condition, an undesirable recombination reaction of generated electrons either with oxidized sensitizer (Equation 2.5) or with the oxidized redox couple at the TiO₂ surface (Equation 2.6) or dark current can occur [23]. These reactions have to be much slower than electron injection and electron transfer from I⁻ ion into oxidized dyes, otherwise the DSC does not work [23].



A thorough study on the kinetics of recombination have been done by Huang et al. [65]. They reported that the net recombination reaction at the TiO₂-electrolyte interface is a two electron reaction (Equation 2.6, 2.7, 2.8 and 2.9) with Equation 2.9

as the limiting reaction while I_2 is the actual electron acceptor in the recombination reaction (Equation 2.8).



which composed of sub-reaction;



Besides, the recombination reaction can also occur between electrons in the conducting substrate and the electrolyte [23]. However, according to the study done by Cahen et al., the reaction is almost negligible due to low electrocatalytic activity of Pt-free conductive substrate surface for the iodine/triiodide redox system [66].

2.3 Structure Modification of TiO_2 Photoelectrode Material

A breakthrough in DSC could possibly be achieved by three possible ways; enhance light scattering, increase the open-circuit voltage of cells and decrease the energy loss due to the charge recombination, electron trapping and optical reflection [43, 64]. It is well known that, the photoelectrode material of DSC is critical in anchoring optimum amount of dye molecules and transport the generated electrons effectively before they are stopped by the surface defect and grain boundaries. Thus, in material science point of view, tailoring the nanomaterial photoelectrode structures may improve the solar cell efficiency by increased electron diffusion length, decreased back recombination, and physical effects such as photon localization, thus decrease in the energy loss [64].

Several approaches on developing noble photoelectrode structure have been on researched for several years. One way is by developing large specific surface area of oxide photoelectrode materials through incorporating smaller nanoparticle size (<20 nm) [30, 33, 67, 68] thus increase the dye absorption. Higher amount of dye

anchored will result in increasing the possibilities of electrons being excited thus increase the chances of them to be transported. Development of one-dimensional nanostructures photoelectrode material is another way of reducing the charge recombination and electron trapping [29, 69-74]. The third way is by introducing light scattering effect which can be done by employing photoelectrode materials with a size comparable to the wavelength of incidence light. The light scattering can extend the photon travel within the photoelectrode films so as to increase photon harvesting efficiency.

2.3.1 Reducing the Size of TiO₂ Nanoparticles

Nanoparticle is a conventional structure of photoelectrode material in DSC. The ease of fabrication, minimal cost and control over light scattering has made these structures widely used in DSC. High specific surface area and surface-to-volume ratio brought about by small particle size provide broad surface area for dye chemisorptions thus improve light harvesting efficiency and cells performance [33, 34]. Nanoparticle can easily be synthesized through sol method, sol-gel method, hydrothermal method, solvothermal method, micelle and inverse micelle and chemical vapor deposition method [32]. However, sol-gel method is a well known and widely applied in preparing the TiO₂ nanoparticles [75-78].

Lee et al. [67] performed a comparative study of TiO₂ nanoparticles prepared through solvothermal and sol-gel modified on DSC photovoltaic performance using 0.1 mol of titanium tetraisopropoxide as titanium precursor and ethanol as solvent. They reported that the sample prepared through solvothermal method at 200°C for 8 h in a nitrogen atmosphere at approximately 10 atm results in smaller particles (10-15 nm). The FT-IR spectroscopy of the two prepared samples with absorbed dye was compared to study the efficiency of charge injection process which is dependent on the bonding structure of the dye molecules on TiO₂ surface. Sample prepared through solvothermal method had shown a strong absorption at approximately 500 cm⁻¹, 1000-1200 cm⁻¹ and weak absorption at 1610-1650 cm⁻¹ which is corresponding to metal-O, C-O band and C=O band, respectively. On the other hand, C=O band is dominant in the sample prepared by sol-gel method. They suggest that

the surface of solvothermal TiO₂ prepared sample and COO⁻ of N719 dye are bonded with perfect bidentate linkage while monodentate and partially bidentate linkage in the case of sol-gel TiO₂ prepared sample resulting in the decrease in I_{SC} due to slow electrons transport.

Nakade et al. [30] reported their study on the influence of particle size in DSSC on diffusion coefficient of electrons (D_n) and electron recombination lifetimes (τ). Their samples of TiO₂ nanoparticle were synthesized through hydrolysis of aqueous TiCl₄ solution followed by hydrothermal at 180-240°C for 2-24 hours. They found that D_n increases as the particle size synthesized from same starting material increases. This would happen due to the decrease in the film surface area and the condition of grain boundaries. In contrast, τ decreases with particle size as τ is related to the electron transport rate in the TiO₂ electrodes. They did suggest that smaller particles size have advantage in absorbing the light which results in an increase in the amount of photogenerated electrons closer to TCO glass substrate. Even so, small particles size will result in short diffusion length.

Jiu et al. [33] had successfully synthesized and control the TiO₂ nanoparticles size of about 3-5 nm by using mixed template system of surfactant cetyltrimethylammonium bromide (CTAB) and copolymer F127 (poly(ethylene oxide)₁₀₆-poly(propylene oxide)₇₀-poly(ethylene oxide)₁₀₆). They focused their research on the optimization of calcination process and investigated the relationship between particles size, surface area and dye adsorption. The prepared samples were then calcined at temperature 350-550°C. Based on XRD patterns and Scherrer equation, the average crystallite size was calculated. The crystallite size was found to increase as the calcination increases from 350°C to 550°C yet the average size still smaller than 10 nm. The presence of copolymer in the sample restrains the crystallite to grow bigger whilst copolymer F127 promotes the homogeneity and avoids coagulation. The light-to-electricity conversion efficiency also increases as the calcination temperature increase due to the improved network structure and interconnection between film particles which in turn results in better electrons transport. Higher efficiency is difficult to achieve with very small nanoparticles

(lower calcination temperature of 350°C) because of low light harvesting in the red region even though it can provide larger surface area for dye chemisorption.

Despite adequate performance of nanoparticle films in conventional DSSCs, this kind of nanostructures TiO₂ photoelectrode material has several disadvantages namely low porosity, reduce the specific surface area due to well photoelectrode packing and tedious particle synthesis. In addition, according to Martinson et al. the key weakness of the nanoparticles structure is the small apparent diffusion coefficient, D_n [68].

2.3.2 One-Dimensional (1D) Structures of TiO₂ Photoelectrode Material

Recently, one-dimensional (1D) nanostructures such as rods, tubes and wires have also become the focus of intensive research owing to their unique applications. These types of nanostructures have potential applications in DSCs, hydrogen sensors, photocatalysts, supports for CdS quantum dots and for novel mesoporous ion-exchange materials. Several methods have been used to synthesize 1D nanostructure namely template method, anodic oxidation and the wet chemical method. The nanostructures are typically in the form of single crystal or quasi single crystal. Consequently, they can enhance the electron diffusion length thus increase the chances of electrons been transported from the point of electron injection to the substrate of the collection electrode [29]. Figure 2.5 illustrates the electrons diffusion in photoelectrode films made up of nanoparticles and 1D structure.

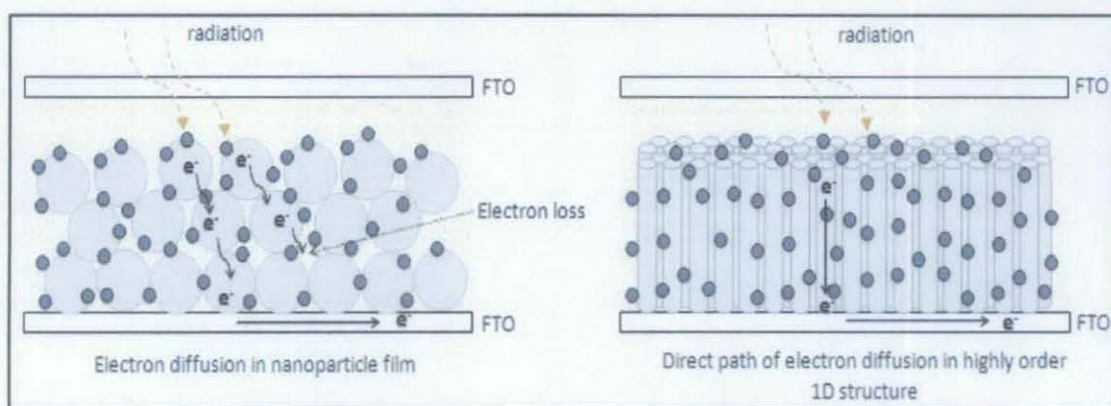


Figure 2.5: Illustration of electrons diffusion in photoelectrode films made up of nanoparticles and 1D structure.

Under alkaline condition, crystalline TiO_2 can transform into nanotube or nanowires structure through a mechanism involving the formation and consecutive wrapping of the titanate nanosheets. Bavykin and co-workers [69] have analyzed systematically the possible mechanisms of nanotube formation by studying the influence of preparation conditions in the alkali hydrothermal synthesis on the morphology of TiO_2 nanotubes. In a typical procedure, TiO_2 nanoparticles were treated with 10 M of NaOH in pressure vessel with temperature range between 120°C and 190°C for 22 hours. In principle, possible mechanisms for multi-wall nanotube formation might include the helical scrolling of a single-layer nanosheet, the curving of several conjoined nanosheets or direct production of a multi-walled nanotube (Figure 2.6).

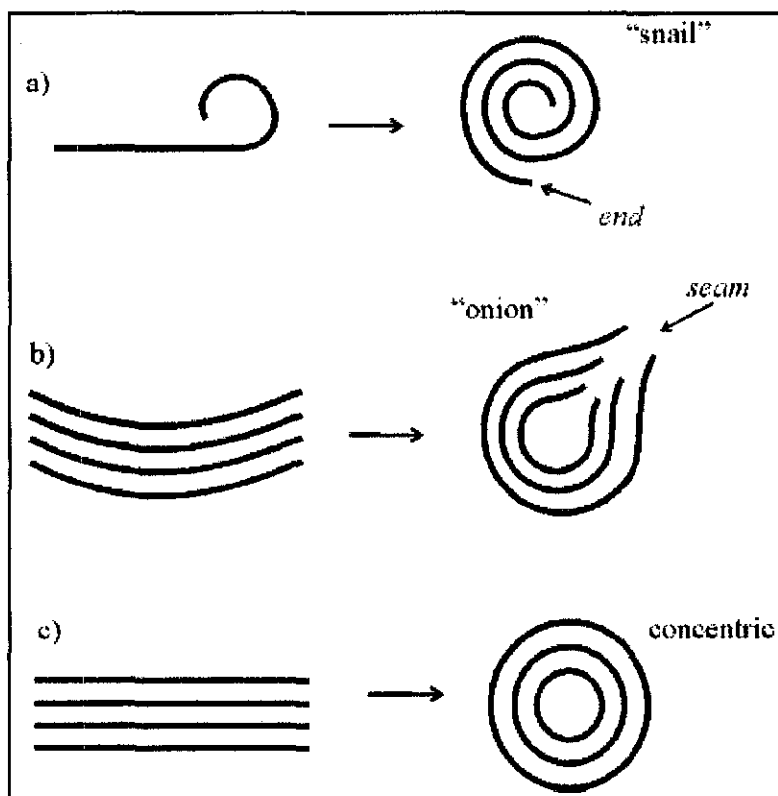


Figure 2.6: Schematic representation of possible mechanisms for the formation of multi-wall nanotubes through (a) helical scrolling, (b) curving and (c) direct production of a multi-walled nanotube as suggested by Bavykin et. al. [69].

However, out of all possible mechanism, the helical scrolling of a single-layer nanosheet process is the most favorable [69-71]. Under appropriate condition, a

single-layer TiO_2 could be scrolled along the [010] axis into a multi-wall nanotube. Besides, the nanotubes may also form through the wrapping of multilayered nanosheets. In a layered chemical compound, the interaction energy between atoms in neighboring layers is usually less than the interaction energy between atoms in the same layer. The driving force for the curving of the sheets can arise from the asymmetry and unsymmetrical surface forces due to locally high surface energy [69]. However, this method demands for high calcination temperature in order to eliminate the sodium impurities [35].

Comparing with the randomly ordered 1D nanostructure, a highly ordered nanostructure with vertically alignment could provide direct pathway for electron transport in DSC [29]. Basically, an anodic alumina membrane (AAM) template was used to produce a well aligned structure due to high pore density and controllable pore diameter and aspect ratio of the template by controlling the anodization process condition. The AAM also is much cheaper compared to lithographic polymer or carbon nanotube. Liu et. al. [72] did propose a combination of template-directing method and electrodeposition approach to produce highly ordered anatase TiO_2 nanowires. The template was firstly prepared through two-steps anodization process of electropolished aluminium foil as anode. The anodization process was carried out in 10wt% of phosphoric acid at 1°C for 5 hours with platinum electrode as the cathode. This process would produce well-arranged pores with diameter of about 200 nm. Electrodeposition was then chosen to develop the nanowires structure instead of sol-gel or chemical vapor deposition (CVD) in order to obtain a pure TiO_2 product. The pulsed electrodeposition step was executed in 100 mL of 0.2M TiCl_3 solution with controlled pH of 2. The quality of nanowires produced can be control by controlling the periods of positive and negative pulse, and the relaxation time of electrodeposition process.

Bwana [74] did a comprehensive study on the performance of dye solar cells based on different TiO_2 electrode nanostructures; nanoparticles, nanotubes and nanorods. In the study, the nanotubes and nanorods were prepared through template method. Controlling the immersion time of template in stock solution would result in different nanostructures obtained either nanotubes or nanorods. With 30 seconds of

immersion time, this approach can produce nanotubes array of 150 nm of external diameter with 80 nm of internal diameter whilst in 2 minutes immersion time, nanorods with diameter of 150 nm can be produced. At an identical film thickness (5 μm), integrated nanoparticles-based DSC exhibit performance efficiency of 4.7% with an average short-circuit current density of 14 mA/cm^2 and 0.43 V of open circuit voltage. Nanotubes-based DSC shows efficiency, short-circuit current density and open circuit voltage of 4.5%, 17 mA/cm^2 and 0.39 V, respectively. Whist, nanorods-based DSC shows an efficiency of 5.4% with short-circuit current density and open circuit voltage of 16 mA/cm^2 and 0.48 V, respectively. Based on the finding, nanotubes demonstrated higher short-circuit current density. Nevertheless, the most efficient cells were those based on ordered arrays of TiO_2 nanorods. This is attributed to the presence of thicker nanorods structure which results in the accumulation of the injected electrons in the trap states of inner TiO_2 molecules, thus preventing from recombination process.

The geometrical structure of 1D nanostructure plays an important role in achieving higher performance photoelectrode material. Tailoring the geometries could result in the formation of photoelectrode material with bigger specific surface area which allows for more dye absorption. A systematic study on the range of fundamental geometrical and structural features of TiO_2 nanotube layers and their effect on the solar cell conversion efficiency have been done by Ghicov et. al. [73] Based on their finding, the length and diameter of nanotubes can control the specific surface area of particular photoelectrode material. The required geometries could be synthesized by controlling the anodization time of Ti in ethylene glycol based electrolyte containing 0.5m HF. Through this method, nanotubes with a wide range of length (1-33 μm) and diameter in the range of 90-220 nm were produced. At an optimum dye immersion time (4 days), increasing the length of nanotubes will increase the thickness of the photoelectrode film, resulting in an increase in the short circuit photocurrent. However, nanotubes with more than 30 μm length were not possible to produce due to the poor stability and peeling of the film from the substrate upon calcination process. On the other hand, reducing the diameter of nanotubes, results in increasing the specific surface area for dye chemisorptions, thus improving the conversion efficiency of the integrated cells significantly. Even though 1D

structure demonstrate a promising enhancement on the performance of DSC due to their unique properties namely fast electron transport, the limited density and thickness may prevent even higher performance of DSC.

2.3.3 Light Scattering Effect in TiO₂ Photoelectrode Film

Light scattering effect in photoelectrode films of DSC have been theoretically proven to enhance the optical absorption [79-81] through the size of the scattering centers and the wavelength of incident light [82]. In a typical porous photoelectrode DSC films, the optical absorption of the films could be improved by utilizing thicker films. However, thicker films results in an increase probability of recombination as electrons must be transported across an increasing number of colloidal particles and grain boundaries [51]. Therefore, incorporating larger-sized of photoelectrode materials as scattering centers could promote optical absorption without compromising the film thickness. According to Ferber and Luther [79], TiO₂ particles of size of 250 nm to 300 nm are effective light scattering centers, which can enhance light harvesting efficiency.

Koo et. al. [82] did a study on the dependency of scattering centers size on the light scattering efficiency in DSC. To investigate the effect, Koo and co-workers integrated an additional scattering layer with two different rutile particles with size of 0.3 μm and 0.5 μm . The main layer was made up of 20 nm sized semitransparent anatase TiO₂. With the main layer film of 7 μm -thick, the performance of DSC was found to be 8.94% by incorporating with 0.3 μm -sized particles as the scattering layer whilst DSC efficiency of 8.74% were obtained when 0.5 μm -sized particles were integrated as the scattering layer. This accounted for about 18.4% and 16.3% increment, respectively. They suggested that the significant improvement in the performance of integrated DSC and size-dependence of scattering layer on the relatively thin main layer is related to the transmitted wavelength of the light and the difference in reflectivity of 0.3 and 0.5 μm -sized scattering particles.

Hore and co-workers [83] did study on the spherical void as light scattering centers in nanocrystalline TiO₂ films. This particular photoelectrode film structure

does not only serve as scattering centers but also allowing the electrolyte to permeate easily in the porous TiO₂ films. In their study, the spherical voids were prepared by utilizing carboxyl stabilized polystyrene spheres of radius 200 nm as a template. Upon sintering, the polystyrene spheres which serve as template will burn out, thus leaving spherical voids structure in the films. Based on their study, they found that utilizing the hollow scattering voids would help in increasing the fill factor and short-circuit current density of DSCs, thus enhancing the photovoltaic performance by 25% on large areas.

According to Zhang et. al. [29], when the size of the scattering center is about $k\lambda$, the scattering will reach a maximum. In the proposed relation, k is known as a constant and λ is the wavelength of incident light. Nevertheless, incorporating large-sized particles would reduce the specific surface area for dye chemisorptions resulting in lower amount of dye being adsorbed on the surface of TiO₂. This would lead to a decrease amount of excited electrons, thus reducing the short-circuit current density of the integrated DSCs.

2.3.4 Submicrons-size TiO₂ Aggregates

Submicron meter size aggregates formed by nanocrystallite are categorized as 3D structure. This kind of structure could take the advantage of large surface area and generate effective light scattering due to the presence of large structure comparable to the wavelength of light, resulting in an enhancement of photon harvesting. Recent development of oxide aggregates as phototelectrode material has demonstrated notable improvement on the performance of DSC [27-29, 38, 40, 84, 85]. Figure 2.7 shows the schematic representation of light scattering in submicrometer-sized aggregates films as suggested by Zhang et. al. [29].

Moreover, the high efficiency of the performance of submicron-sized aggregates-based DSC was also contributed by the improvement of electrolyte diffusion in between the aggregates and interstitial voids among the nanocrystallite which made up the aggregate structure. Figure 2.8 illustrate the electrolyte diffusion through the

external and internal pores of submicron-sized aggregates photoelectrode films as suggested by Kim et. al. [86].

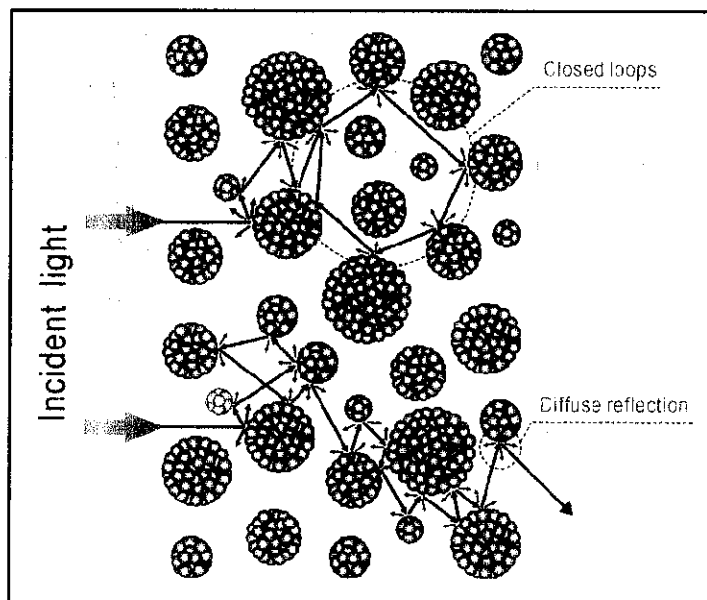


Figure 2.7: Schematic representation of light scattering in submicrometer-sized aggregates films as suggested by Zhang et. al. [29].

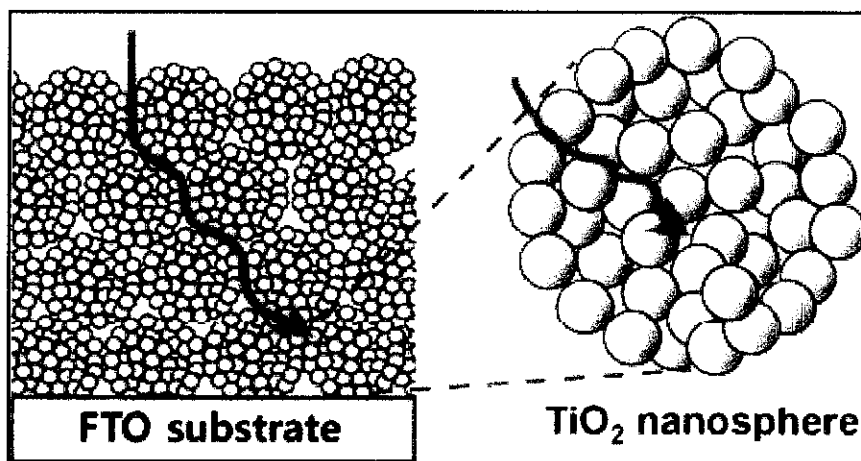


Figure 2.8: Illustrate the electrolyte diffusion through the external and internal pores of submicron-sized aggregates photoelectrode films as suggested by Kim et. al. [86].

Zhang and co-workers did a thorough study on the development of ZnO and TiO₂ aggregates as photoelectrode materials in DSC. In a typical reflux method, 0.01 mol of zinc acetate were hydrolyzed in 100 mL of ethylene glycol heated to 160°C for about 24 hrs [27, 28, 39]. Both monodisperse and polydisperse ZnO aggregates with a

diameter of approximately 300 nm consisting of about 20 nm nanocrystallite size could be synthesized through modifying the heating rate between 5°C to 10°C. The same method has been proposed by Zhang et. al. to produce TiO₂ aggregates [84]. A mixture of 1 ml titanium alkoxide and 30 mL ethylene glycol was mixed with a second solution containing 1 mL di-ionized water and 400 mL acetone under stirring condition. The stock solution was then refluxed at 120°C for 90 minutes in 500 mL de-ionized water containing 0.5 mL of acetate acid.

A remarkable achievement on the performance of DSC with more than 100% increment on the efficiency of ZnO aggregates-based DSC has been reported comparing with the one comprises of 100% nanoparticles structure. However, when the synthesized TiO₂ aggregates were incorporated in DSC, the performance efficiency was lower compared to TiO₂ nanoparticle-based DSC due to low porosity and unsuitable facets of nanocrystallites which made up the aggregates [84].

CHAPTER 3

METHODOLOGY

This chapter discuss mainly on the research methodology which covers material synthesis, characterization, cells integration and performance verification. The synthesized TiO₂ samples were characterized using thermogravimetry-differential thermal analysis (TG-DTA) to examine the samples decomposition and possible phase change during thermal event. Scanning electron microscopy (SEM) was used to determine the particle shape, state of agglomeration and aggregate size distribution while phases, crystallographic structure and crystallite size (grain size) of the samples were examined through X-ray diffraction (XRD) technique. The surface area, pore volume as well as size of the synthesized samples were determined using BET procedure whilst the UV-vis spectra were used to study the optical characteristic of the synthesized TiO₂ film. This chapter also describes in detail the film deposition method, DSCs assembly and performance verification techniques which includes *I-V* characterization. The overall flowchart of the methodology is illustrated in Figure 3.1.

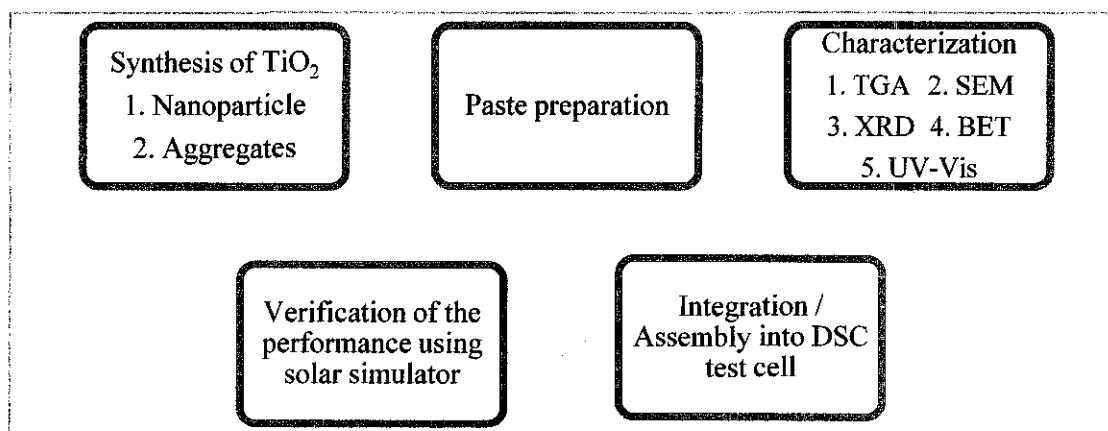


Figure 3.1: Flowchart of overall methodology

3.1 Synthesis and Paste Preparation of TiO₂ Photoelectrode Material

3.1.1 Synthesis of TiO₂ Photoelectrode Material

3.1.1.1 Synthesis of TiO₂ Nanoparticles

Pure anatase TiO₂ nanoparticle was prepared by precipitation of titanium alkoxide precursor by way of acid-catalyzed hydrolysis step followed by condensation reaction. The chemical used in making TiO₂ sol were titanium (IV) isopropoxide [Ti{OCH(CH₃)₂}₄], glacial acetic acid [CH₃CO₂H], isopropanol and deionized water. A stock solution was prepared by dissolving 15 mL of titanium (IV) isopropoxide in 85 mL of isopropanol. The solution was then refluxed at 80°C for 4 hrs under stirring condition. A solution containing 364 ml of isopropanol, 36 mL of deionized and few drops of acetic acid were prepared in a separate beaker. The solution was stirred for 1 hr before being added into refluxed-stock solution. White precipitate was immediately formed upon mixing. This was due to the precipitation of large aggregates in the presence of high water-to-titanium mole ratio resulting in a fast nucleation and growth stage [75].

The reflux process was then continued for another 20 hrs under stirring condition to disperse the large aggregates into primary nanoparticles. Finally, the colloidal was filtered, washed several times until the pH became neutral and then allowed to dry at 100°C for 24 hrs. TG-DTA of the TiO₂ precursor was then run to estimate the right calcination temperature for the synthesized TiO₂ samples. Based on the TG-DTA result, the calcination temperature was set at 420°C for 2 hrs. The flowchart of the process in producing TiO₂ nanoparticles is shown in Figure 3.2. The synthesized TiO₂ was then characterized using SEM, XRD and UV-Vis and the performance was compared with commercially available TiO₂ namely P-25 (Degussa) and TiO₂-MERCK. Table 3.1 below shows the specification of P-25 (Degussa) and TiO₂-MERCK used in this study:

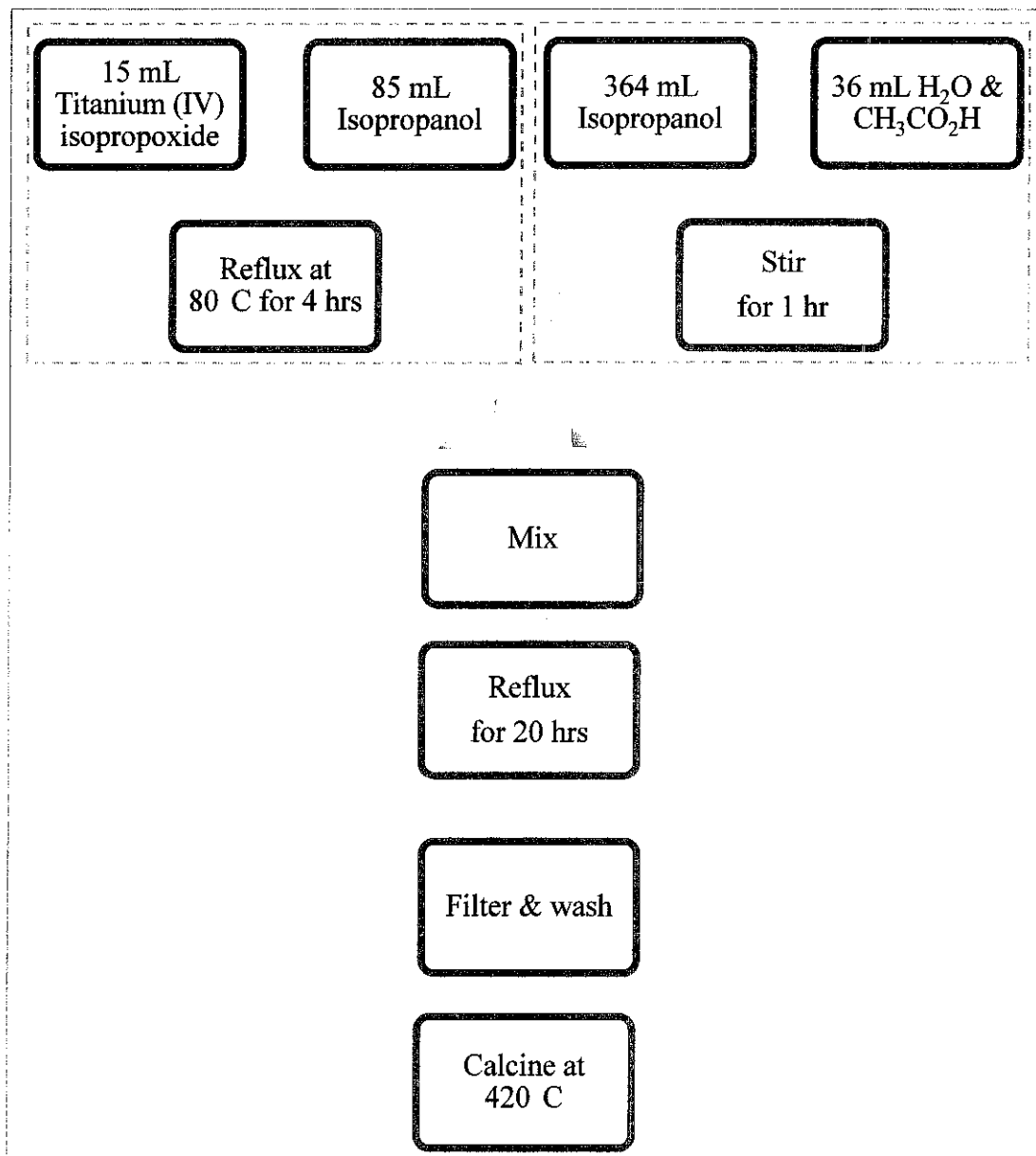


Figure 3.2: Flowchart of the process in producing TiO₂ nanoparticles

Table 3.1: Specification of P-25 (Degussa) and TiO₂-MERCK

Sample Name	Specification
P-25 (Degussa)	Degussa P-25, Frankfurt am Main, Germany Crystallite size: 20-50 nm Surface area: ~50 m ² /g Phase: 80% anatase and 20% rutile Apparent density: 130 kg/m ³
TiO ₂ -MERCK	Titanium dioxide for analysis EMSURE® Reag. Ph Eur CAS No.: 13463-67-7 Phase: anatase Apparent density: 850 kg/m ³

3.1.1.2 Synthesis of TiO₂ Submicron-size Aggregates

TiO₂ aggregate made up of primary nanocrystallite were prepared by controlling the hydrolysis of dilute titanium (IV) isopropoxide, Ti{OCH(CH₃)₂}₄ in ethanol. All chemicals in this study were used as received without further purification except for isopropanol and deionized water which were ultrafiltered through 0.22 μm pore size filters due to the requirement for high purity. In order to avoid any reaction of titanium precursor with the moisture in the environment, the synthesis process was done in glove box having argon environment with moisture content less than 100 ppm throughout the procedure.

The titanium precursor was dissolved in one-half of the total volume of ethanol while the other half is mixed with de-ionized water to prepare the desired aqueous isopropanol-water solution containing 0.2 M of titanium precursor and 0.9-3.6 vol% of deionized water. Throughout this study, the water content in ethanol solution is in volume percentage. Both solution were then mixing together and stirred at minimum stirring to prevent coagulation. The precipitation were controlled by the percentage of water contents and concentration of Ti(OC₂H₅)₄. At low water content, spherical with relatively monodisperse aggregates of nanocrystallites is obtained [75, 87-89]. The growth kinetics of the aggregates is determined by the stability of colloid. Within 30 minutes taken out from glovebox, the colloids were filtered and washed to avoid agglomerate formation in the alcohol by dissolution or reprecipitation process [87-89]. The surface precipitate formation can be reduced and prevented through twice ethanol washing, followed by vacuum drying and water washing techniques.

To study the effect of percentage of water content in ethanol solution, the sample was synthesized with 0.9 vol%, 1.8 vol%, 2.7 vol% and 3.6 vol% of water and calcined at temperature 420°C while to study the effect of water content, sample was synthesized with 0.9 vol% of water in ethanol solution and calcined at 4 different temperature; 400°C, 500°C, 600°C and 700°C for two hrs. Table 3.2 summarizes the condition used in synthesizing TiO₂ aggregates samples while Figure 3.3 shows the flowchart of the process in producing TiO₂ aggregates.

Table 3.2: Condition adopted in the preparation of TiO₂ aggregates samples

Sample No.	Percentage of water content (vol%)	Calcination temperature (°C)
1	0.9	420
2	1.8	
3	2.7	
4	3.6	
5		400
6	0.9	500
7		600
8		700

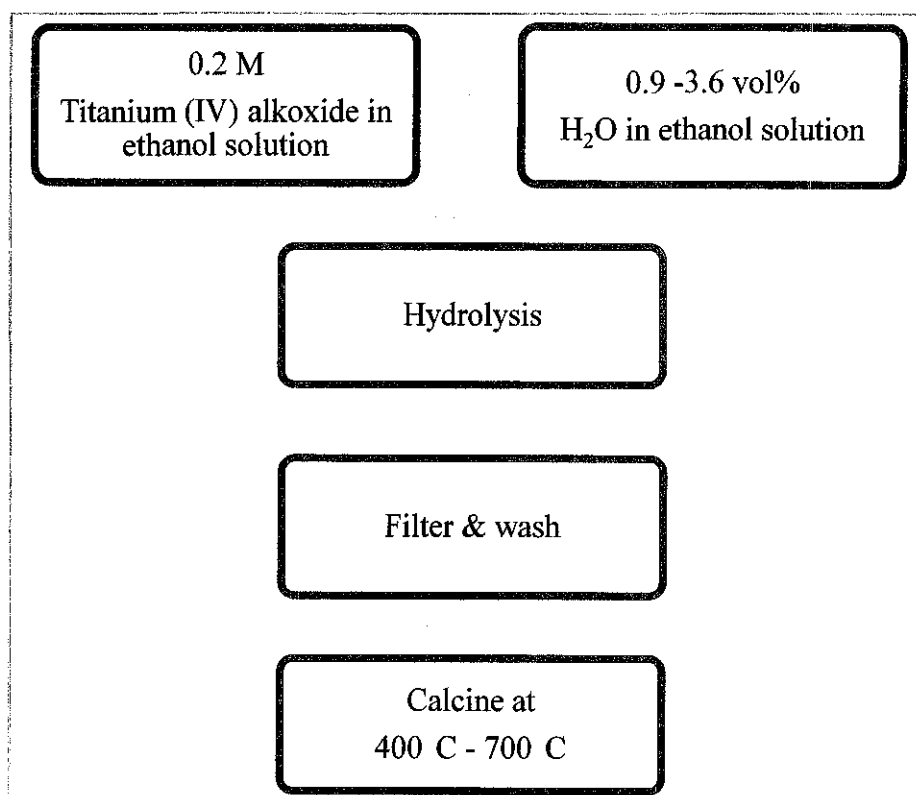


Figure 3.3: Flowchart of the process in producing TiO₂ aggregates

3.1.1.3 Preparation of TiO₂ Aggregates/Nanoparticles Composite

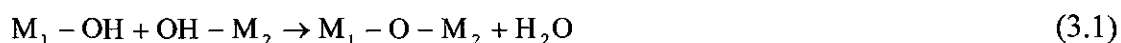
The aggregates/nanoparticles composite photoelectrode material was prepared by mixing synthesized TiO₂ nanoparticles with TiO₂ aggregates. The TiO₂ aggregates used in preparing composite photoelectrode material was synthesized by using 0.9 vol% of water in ethanol solution and calcined at 450°C which is the optimum temperature obtained by interpolating the graph of dependency of short circuit current and performance efficiency on calcination temperature (Figure 4.23 and Figure 4.24). The percentage of nanoparticles mixed with aggregates in the composite

photoelectrode films were varied from 0% to 100% of nanoparticles. The performance of the developed cells integrated with the prepared aggregates/nanoparticles composite photoelectrode films were validated using UV-Vis and IV-characterization.

3.1.2 Preparation of TiO₂ Photoelectrode Paste

The photoelectrode paste were prepared by using terpeneol, ethyl cellulose, acetic acid and ethanol absolute following the procedure reported by Ito et al. [90] with some modification. All chemical used in preparing the paste were used as received without further purification. 5 g of TiO₂ sample was grounded for about 5 minutes in porcelain mortar with addition of 1.0 mL of acetic acid. The proton (H⁺) of the acid can shift the Zeta potential of the TiO₂ particles surface to positive [90]. This will result in particles repelling from each other and act as good dispersion agent in preventing coagulation.

The paste was then diluted further by addition of 4.0 mL of distilled water under continuous grinding. The addition of distilled water prevents cracks and peeling off of the TiO₂ photoelectrode film from substrate after sintering process as suggested by Ito et al. [90] The hydroxide (OH) of distilled water added during paste preparation process can create a strong chemical bonding within the TiO₂ particles and between TiO₂ particle and fluorine-doped tin oxide (FTO) glass substrate as illustrated in Equation 3.1:



where, M₁ represent the Ti atoms on a surface of particle while M₂ represent the Ti atom on another surface particle or on FTO substrate.

After grinding for about 1 minute, an additional of 25 mL of absolute ethanol was added drop wise. Then, the paste was sonicated in ultrasonic bath for 1 minute followed by an addition of 25 g of 10-15 wt% of ethyl cellulose in terpeneol solution. Further grinding process and sonification was done until a well uniform paste formed. Figure 3.4 shows the flowchart of the overall process in preparing photoelectrode paste.

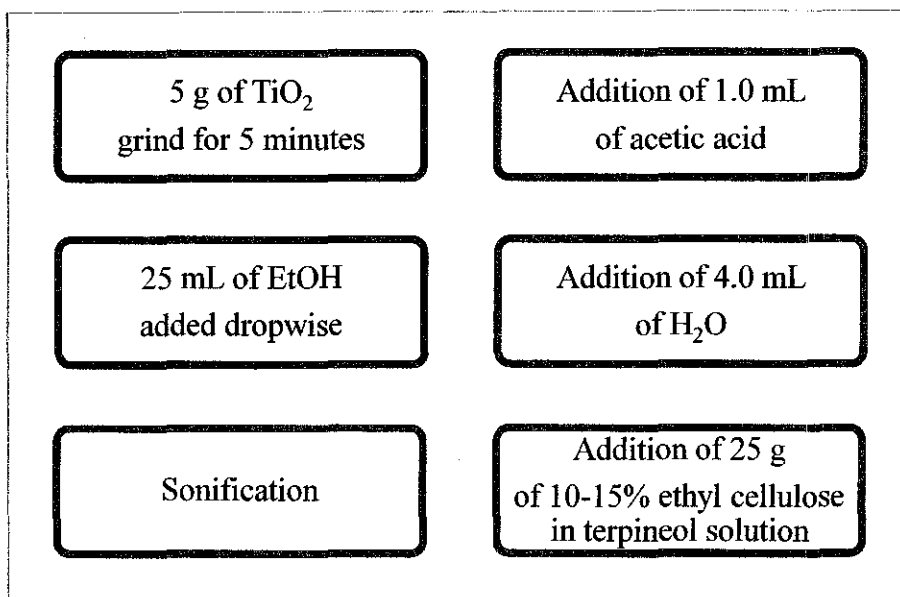


Figure 3.4: Flowchart of the process in preparing photoelectrode paste

3.2 Characterization of Synthesized Samples

3.2.1 Thermogravimetric-Differential Thermal Analysis (TG-DTA)

Figure 3.5 (Appendix A) shows the image of Perkin Elmer EXSTAR TG/DTA 6000 Series used in this study. The thermogravimetry (TG) was used to examine the decomposition of synthesized sample by monitoring the mass change with temperature while differential thermal analysis (DTA) was used to examine the possible phase changes in the sample. From the results, the calcination temperature for synthesized TiO_2 samples was set based on the transition temperature of amorphous to crystalline anatase phase. The transition temperature can be determined by measuring the intersection of the tangent to the maximum rising slope of the peak and the extrapolated sample baseline. In this study, a heating rate of $10^\circ\text{C}/\text{min}$, a nitrogen flow rate of $130 \text{ mL}/\text{min}$, sample sizes between 13 mg to 52 mg , pure $\alpha\text{-Al}_2\text{O}_3$ as reference material, and open Pt crucible was used. Figure 3.6 shows the heating profile of TG-DTA analysis.

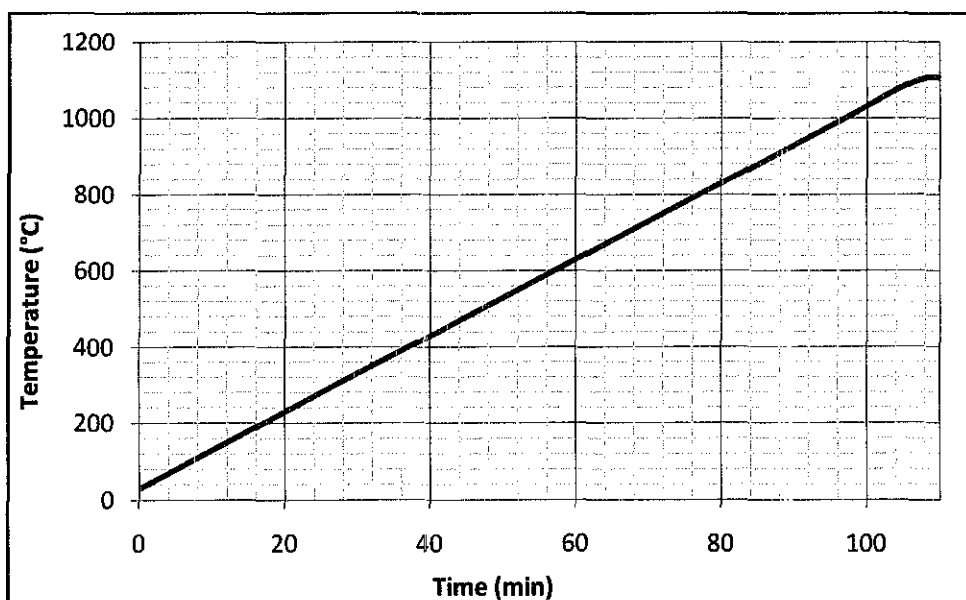


Figure 3.6: Heating profile of TG-DTA analysis.

3.2.2 Scanning Electron Microscopy (SEM)

Assessments of particle shape, state of agglomeration, and qualitative size distributions were obtained from Zeiss Supra 55VP Scanning Electron Microscopy in Central Analytical Lab of Universiti Teknologi PETRONAS (Figure 3.7 – Appendix A). Since TiO_2 is a semiconductor material, the synthesized samples can be examined in SEM with virtually no specimen preparation. Nevertheless, the samples need to be vacuumed properly before taking an image. The vacuum allows electron movement along the column without scattering and helps prevent discharges inside the instrument.

In this study, SEM characterization was run with accelerating voltages range from 5 to 10 kV at several magnifications. The particles sizes were then measured using electronic ruler at few spots. Quantitative number distributions were obtained for >100 measured size of aggregates from the obtained images by using a histogram method and fitted by log-normal distribution function. The data analysis will be used to estimate the mean synthesized TiO_2 aggregates diameter and standard deviation which will determine disparity of the aggregates diameter.

3.2.3 X-ray Diffraction (XRD)

X-ray diffraction (XRD) technique was used to evaluate and verify the phase, crystallographic structure and crystallite size [91] of the synthesized samples operated at 40 kV using a Ni-filtered Cu K α radiation ($\lambda = 1.54 \text{ \AA}$) of the step scan size of 0.02° with scan speed of 10s in the range 2θ of 2° to 80° . Figure 3.8 shows the image of X-Ray Diffractometer in Engineering Material Lab of Mechanical Engineering Department, Universiti Teknologi PETRONAS.

Identification of the crystalline phases of the synthesized samples was achieved by matching the peak positions and relative intensities, comparing the chemical composition as well as the samples spectrum with the spectra of known crystalline substance from *powder diffraction file* (PDF). Figure 3.9 and Figure 3.10 show the ideal peaks of two frequent existing phases of TiO₂ (anatase and rutile) as per PDF.

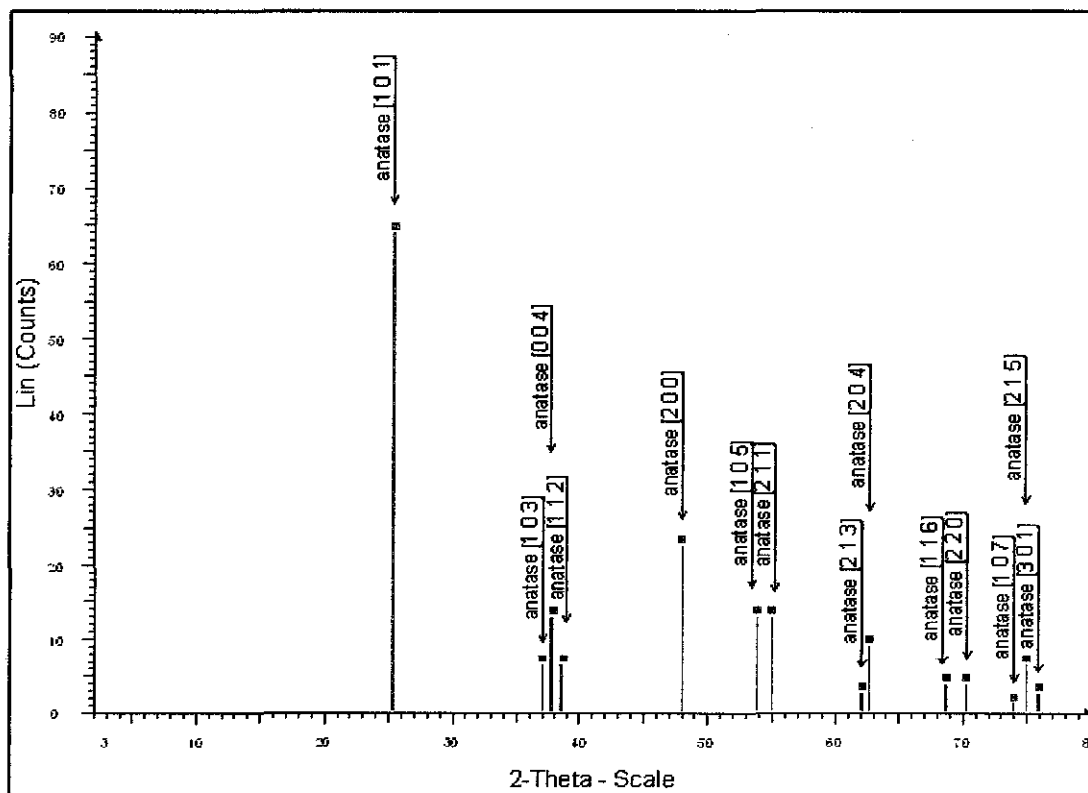


Figure 3.9: Ideal peaks of TiO₂ anatase phase based on PDF (21-1272)

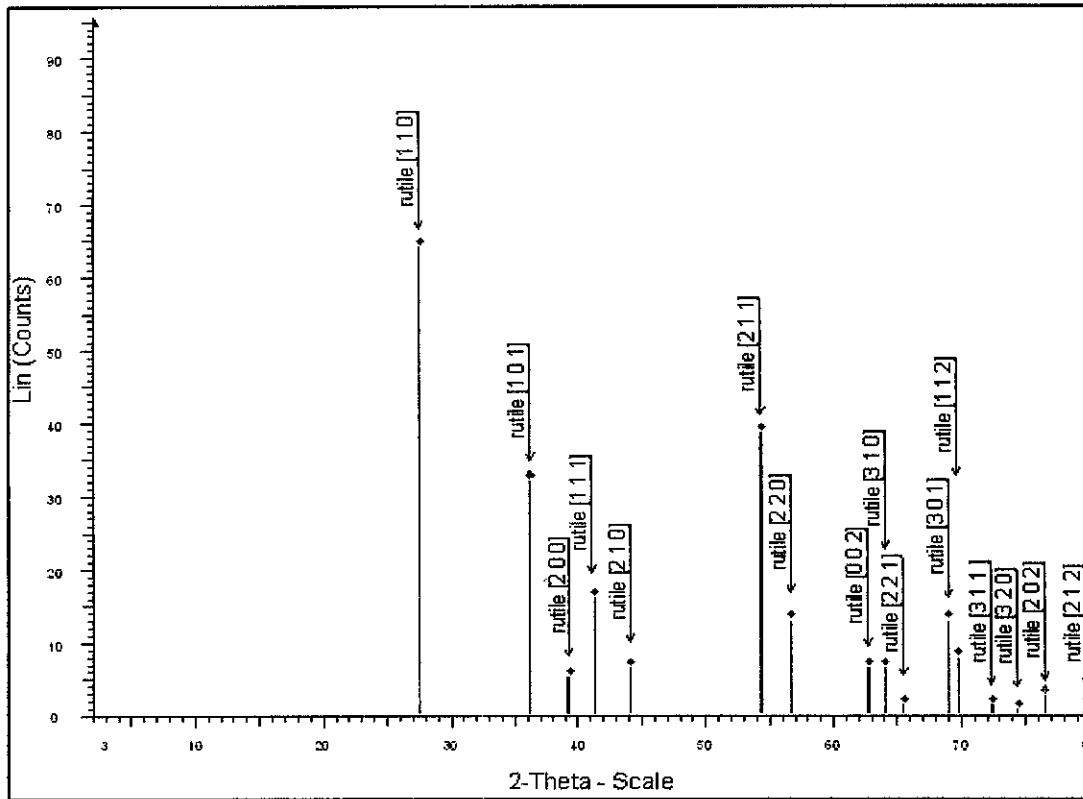


Figure 3.10: Ideal peaks of TiO₂ rutile phase based on PDF (21-1276)

If samples consist of phase mixtures, then qualitative analysis could be performed to determine the percentage of relative amounts of the phases in the sample. The qualitative analysis was done based on the weight fraction information by measuring the intensities of the peaks assigned to the particular phase since the intensity of diffraction peaks is dependent on the weight fraction of the particular phase in the mixture. The relationship could be expressed using the Spurr and Myers's method [92, 93] as in Equation 3.2:

$$W_r = \frac{1}{1 + 0.8 \left(\frac{I_a}{I_r} \right)} \quad (3.2)$$

where W_r is the weight percentage of rutile in synthesized sample, I_a and I_r are the peak intensity of anatase (d_{101}) and rutile (d_{110}) phase, respectively.

The width of the peak can vary depending on the crystallite size. Smaller crystallite size will result in a wider peak due to the incomplete destructive interference. The theory of dependency of peak broadening on the crystallite size, d of

a sample is explained by Scherer formula (Equation 3.3):

$$d = \frac{K\lambda}{\beta \cos\theta} \quad (3.3)$$

where, d is the crystallite size, K is the shape factor (0.94), λ is the wavelength of the diffraction peaks (1.542), β is the line broadening at half the maximum intensity (FWHM) in radians, and θ is the Bragg's angle. Equation 3.4 is the basic law of diffraction known as Bragg's Law which is used to find the Bragg's angle.

$$\sin\theta = \frac{\lambda}{2d_{hkl}} \quad (3.4)$$

Where, θ is half the angle between the diffracted beam and the original beam direction, λ is the wavelength of the X-rays while d_{hkl} is the interplanar spacing between the planes.

3.2.4 Brunauer-Emmett-Tellet (BET) Analysis

In this study, Surface Area and Pore Size Analyzer model Micromeritics ASAP 2020 (Figure 3.11) in Central Analytical Lab of Universiti Teknologi PETRONAS was used to acquire information on samples surface area based on physical adsorption of a gas (normally Nitrogen, Krypton and Helium) onto the surface of the sample at liquid nitrogen temperatures [91]. Prior to the analysis, the sample must be preconditioned to remove physically bonded impurities from the surface of the powder. This preconditioned was done by applying elevated temperature to the sample in conjunction with vacuum or continuously flowing inert gas. This step is important in order to get an accurate and repeatable result.

The nitrogen adsorption and desorption isotherms were measured using a surface area and porosity analyzer after the samples were degassed in vacuum at 300°C for 3 hrs. BET surface areas were calculated from the BET plot. The pore size distribution was determined from the desorption isotherm employing the BJH theory assuming cylindrical pore geometry. Pore volume was measured at the single point of $P/P_0 = 0.99$.

3.2.5 UV-Visible (UV-Vis) Analysis

In this study, UV-Vis spectroscopy was used to examine the ability of the sensitized TiO₂ photoelectrode films with dye to absorb light and also to determine the amount of dye absorbed by the photoelectrode films. According to Beer-Lambert's law, the absorbance of a solution is depending on the concentration of the absorbing species in the solution and the path length.

In order to examine the ability of the sensitized TiO₂ photoelectrode films to absorb light, the synthesized samples were firstly converted into paste and double printed on FTO glass to get 10 to 12 μm-thick films. After gradually sintered under air flow, the TiO₂ electrodes were dye-coated by immersing in N719 dye overnight and then rinsed to remove access dye. The UV-Vis spectra of the films were then obtained in the range of 800-380 nm with FTO glass as baseline. Figure 3.12 shows the image of UV-Vis Reflectance Spectrophotometer (Shimadzu UV-3150) and its sample holder used to characterize the dye-coated synthesized TiO₂ films.

The UV-Vis of desorbed-dye solution was also tested to examine the amount of dye being absorbed by respective TiO₂ photoelectrode films. In this analysis, the prepared films were firstly soaked overnight in N719 dye solution. The films were then wash with absolute ethanol to remove access dye and soaked in diluted ammonium hydroxide solution for desorption process of the dye from photoelectrode films. In preparing the diluted ammonium hydroxide solution, 10 mL of 30% ammonium hydroxide solution (CAS No. 1336-21-6) was mixed with 200 mL of distilled water to produce 0.85 M of diluted solution. 10 mL of the diluted ammonium hydroxide solution was then used to desorb the dye on each photoelectrode films. The solutions were placed in cuvettes and were scanned in analysis chamber from 900 nm to 200 nm with diluted ammonium hydroxide solution as baseline. Figure 3.13 shows the image of UV-Vis Spectrophotometer (Shimadzu UV-3150) and its sample holder used to characterize the dye solution.

3.3 Cells Integration and Performance Verification

3.3.1 Test Cells Integration

The fabrication and assembly parts were started by cutting the commercially available Fluorine-doped tin oxide (FTO) glasses into required dimension for both working electrode (WE) and counter electrode (CE) sides. Figure 3.14 shows the dimension of each WE and CE. The CE glasses were required to be sandblasted to produce hole for the purpose of injection of electrolyte later on. Then, both CEs and WEs were washed using detergent solution and cleaned firing to burn off any organics and ensure that the glass is clean to maximize the adhesion of the printed films.

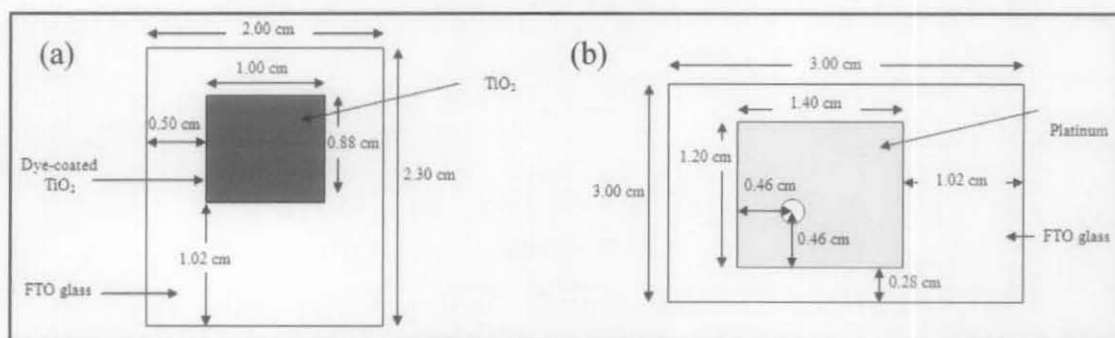


Figure 3.14: Dimension of (a) working and (b) counter electrode

WEs were then screen printed with TiO_2 layer while CEs were printed with platinum (Pt) layer. The TiO_2 layer on the WEs has a function to absorb the dye that can capture the light. Thus, the layer needs to be thick enough to optimize the efficiency. But, too thick of the TiO_2 layer will lower the voltage due to greater back reaction. The thickness of the TiO_2 layer can be controlled by controlling the number of layers and screen mesh counts. In this work, 43T (threads per cm) were used with two layers dried in between were practiced to get about 10-12 μm , which was the most optimum thickness as reported by Kang et. al [94] and Baglio et. al [95]. Proper drying process in between layer is important to avoid film cracking during firing because of rapid solvent escape from the film. In contrast to WE, CE which were printed with Pt layer works as catalyst by aiding in the regeneration of the dye molecules. Thus, one layer of Pt is enough to be printed. Then both WE and CE were fired in a belt furnace with the temperature profile as shown in Figure 3.15. This kind

of slow firing profile is important in order to keep the photoelectrode films and Pt layer from peeling off from the substrate during the process of removing the organic material.

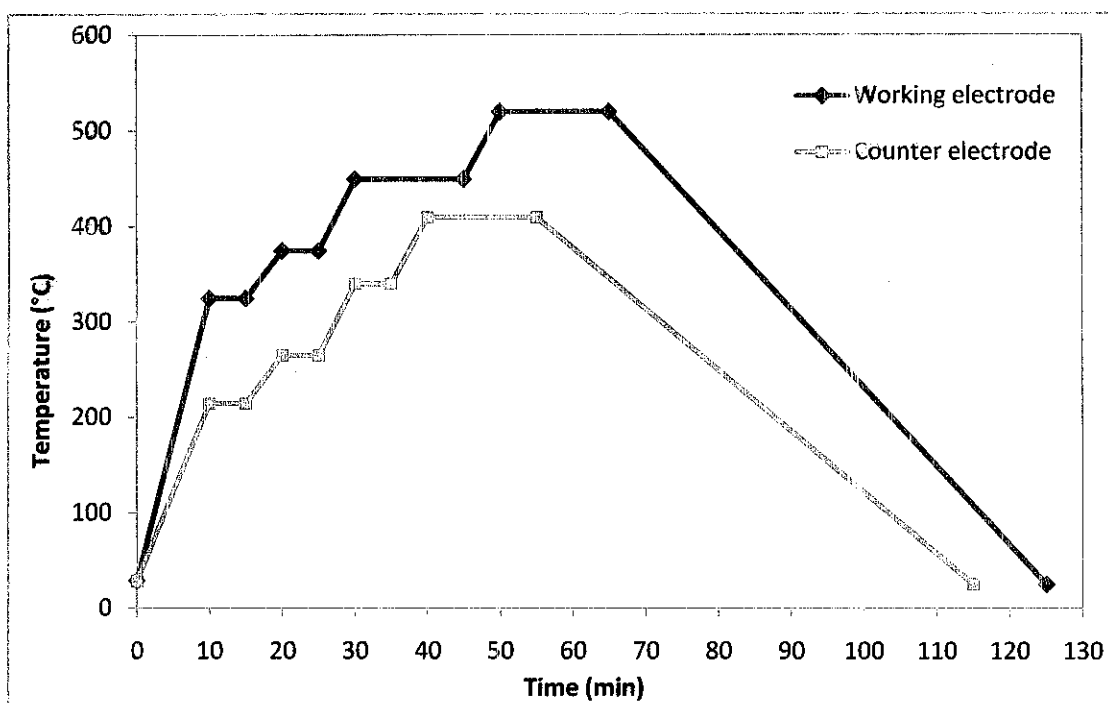


Figure 3.15: Temperature profile for firing CE and WE

The WEs printed with TiO_2 photoelectrode film were then immersed into a 0.5 mM of N719 dye in ethanol solution and keep at room temperature overnight to complete the sensitizer uptake. Dye-sensitized WEs were then rinsed with anhydrous alcohol to remove any non-bonded dye which may interfere with DSC performance. The dye-sensitized WE and CE were assembled into a sandwich layer and sealed with a hot-melt thermoplastic gasket using test cell assembly machine (TCAM). An electrolyte solution of iodide/tri-iodide redox couple system was then injected through the hole drilled on the CE earlier. Even though other electrolyte such as 1,3-dialkylimidazolium iodide shows chemically and thermally more stable, iodide/tri-iodide was choose as electrolyte due to its efficiency and in this study sealing is not an issue which usually a major problem occur in iodide/tri-iodide electrolyte based DSC. Finally, the hole was sealed using aluminum backed bynel. Figure 3.16 shows the process flow of DSC test cell assembly while Figure 3.17 shows the assembled DSC.

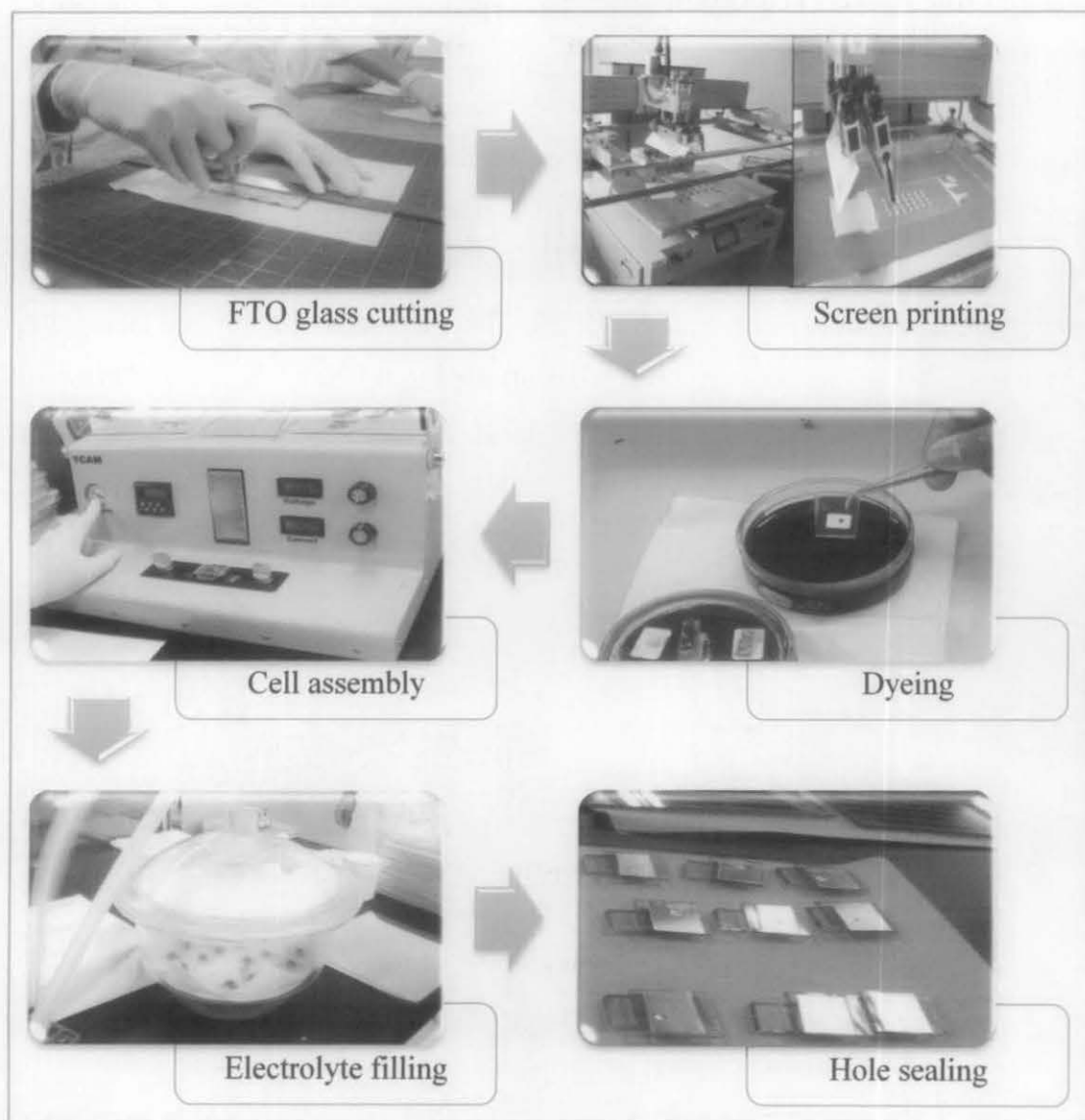


Figure 3.16: Overall process flow of the assembly of DSC test cell

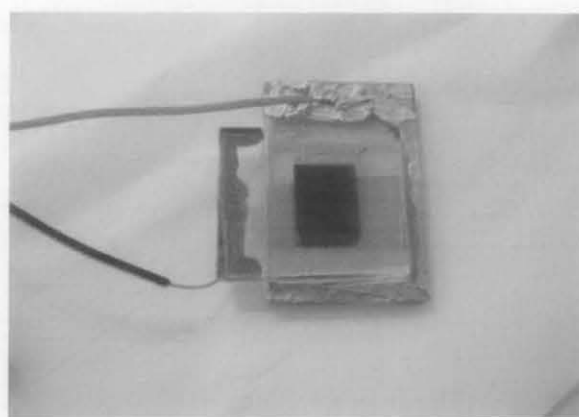


Figure 3.17: Image of assembled DSC

3.3.2 Performance Verification

3.3.2.1 *IV Characterization*

The performance of the integrated DSCs was verified using a Universal Photovoltaic Test System, Dyesol (Figure 3.18) under 1000 W/cm^2 intensity of illuminant Xenon lamp at an AM-1.5 radiation angle connected to a voltmeter and ampere meter (Model 2420, Keithly) with variable load. The parameter namely voltage limit, current max, delay, area and sun level were adjusted to 0.8 V for V_{max} and -0.1 V for V_{min} , 0.02 A , 0.1 sec , 0.88 cm^2 and 1 sun level, respectively. Figure 3.19 shows a typical current-voltage (*IV*) curve of DSC.

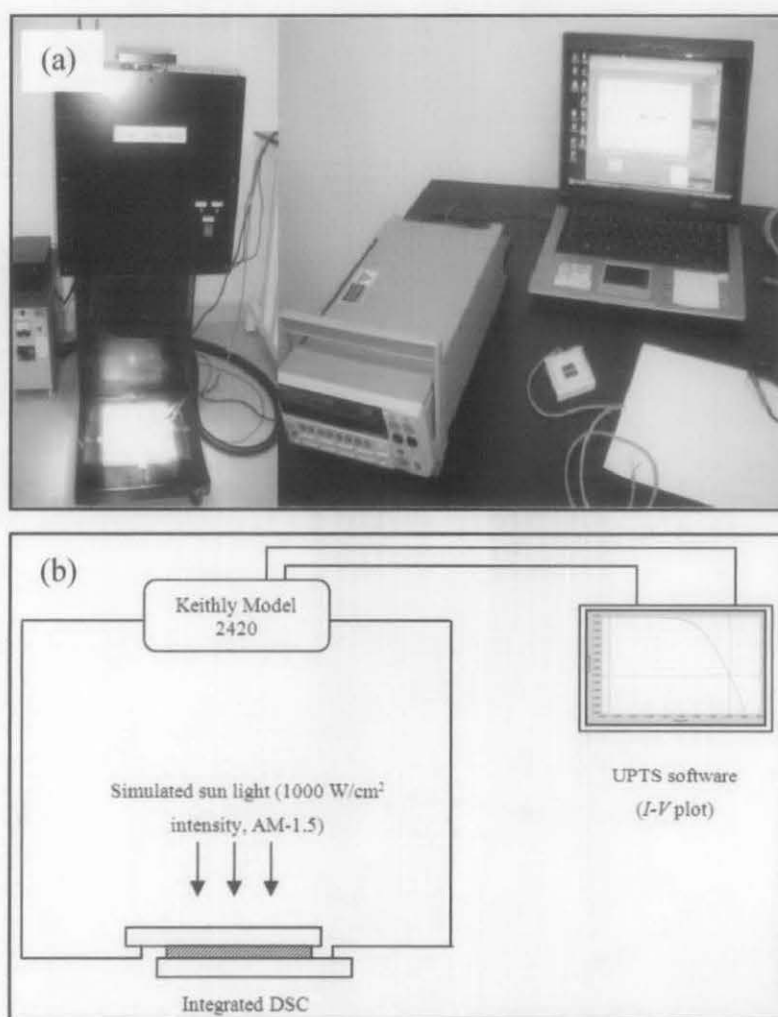


Figure 3.18: (a) Picture and (b) schematic diagram of Universal Photovoltaic Test System, Dyesol

Under illumination, the tested DSC is short circuited, generating maximum current (I_{max}) and short circuit current (I_{sc}) whilst a maximum voltage (V_{max}) was generated under open circuit conditions where no current can flow. On one side, the fill factor (FF) and solar energy conversion efficiency (%) of a DSC can be calculated according to Eqn. (3.5) and (3.6) respectively [29, 96]:

$$FF = \frac{I_{max} \times V_{max}}{I_{sc} \times V_{oc}} \quad (3.5)$$

$$\eta(\%) = \frac{P_{out}}{P_{in}} \times 100 = \frac{I_{max} \times V_{max}}{P_{in}} \times 100 = \frac{I_{sc} \times V_{oc} \times FF}{P_{in}} \times 100 \quad (3.6)$$

where P_{out} and P_{in} is the output and input power density. The P_{in} is taken as the intensity of incident light, in W/cm^2 , V_{oc} is the open circuit voltage (in V), I_{sc} is short-circuit current density (in A/cm^2) and V_{max} and I_{max} are the voltage and current at maximum power output.

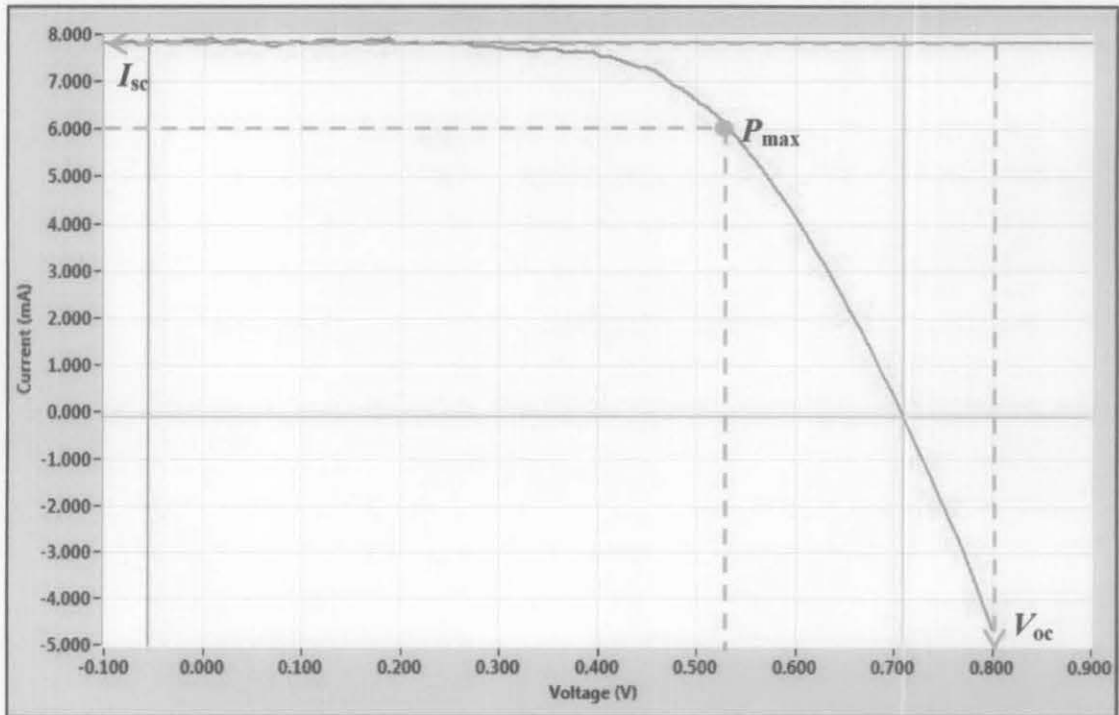


Figure 3.19: Typical IV -curve of a DSC

3.3.2.2 Photocurrent Action Spectra Analysis

The photocurrent action spectra analysis which displays the wavelength distribution of incident monochromatic photon to current conversion efficiency (IPCE) was done to verify the existence of scattering in the photoelectrode films. Table 3.3 shows the specification condition of the photocurrent action spectra analysis.

Table 3.3: Specification of photocurrent action spectra analysis

Light source	75 W Xenon lump
Power of irradiation	10 mW
Quality of light	Parallel light
Range of irradiation	300-1000 nm
Purity of monochromatic light	15 nm
Way of spectrum	Monochromatic
Controller for power of irradiation	Yes
Area of irradiation	5 x 5 mm
Attachable option (after set up)	To be AC type Spectra-radiometer Collar bias
Check for stray light	Yes

CHAPTER 4

RESULT AND DISCUSSION

A conventional DSC was made up of 10 microns thick film comprising of interconnected 15-20 nm-sized TiO₂ nanoparticles [30]. As the size, phase and morphology of TiO₂ vary, not only does the physico-chemical property change but also the performance of DSC which has become photoelectrode structure related. The specific surface area and surface-to-volume ratio increase dramatically as the size of particles reduce to nanometer scale. Films made up of smaller particles have an advantage in providing a larger surface area and have a greater number of contact points, allowing for greater dye adsorption. However, smaller particles exhibit a larger number of grain boundaries where electrons need to pass through, which results in a higher probability of electron trapping. On the other hand, utilizing bigger nanoparticles would take up volume, reducing the amount of dye being absorbed yet could introduce light scattering effect. Hence, a novel structure which takes the advantage of larger surface area and light scattering effect was introduced.

This chapter presents the result of the synthesized TiO₂ nanoparticles and submicron-sized aggregates photoelectrode material that can exhibit better characteristic and performance efficiency compared to commercially available TiO₂ namely P-25 (Degussa) and TiO₂-MERCK. The effect of two critical parameters on the morphology and microstructure of the synthesized TiO₂ aggregates have been studied and their structure-properties relationships were reported in section 4.2. Mixture of TiO₂ aggregates and nanoparticles photoelectrode materials were developed and the influence of their composite on the performance of fabricated DSCs was investigated under simulated AM1.5 sunlight illumination with 100 mW/cm² light output.

4.1 Synthesis of TiO₂ Nanoparticles for Dye Solar Cells (DSC)

In this subsection, solar cells integrated with three different types of TiO₂ nanoparticles (P-25, TiO₂-MERCK and synthesized TiO₂ nanoparticles) as photoelectrode material were studied and compared to determine the effect of their structure-properties on the overall performance of DSCs. P-25 and TiO₂-MERCK samples were used as received while the synthesized TiO₂ sample was calcined in order to obtain purely anatase phase.

4.1.1 Physico-chemical Properties of P-25, TiO₂-MERCK and Synthesized TiO₂ Nanoparticles

In order to select the right calcination temperature of the synthesized TiO₂, the thermal properties of the material was studied using thermogravimetry (TG) and differential thermal analysis (DTA). TG-DTA basically measures the changes in material properties as a function of temperature. Without pretreatment, the synthesized TiO₂ sample was tested with simultaneous TG-DTA, annealed at a scan rate of 10°C/min, in nitrogen environment. Sample weight with less than 10 mg was used in this characterization technique to ensure better heat transfer between the sample and the testing environment thus results in faster thermal equilibrium [97].

Based on the thermogram shown in Figure 4.1, the total weight loss in the temperature region up to 1000°C is about 70% of the initial sample weight which is nearly the same as the theoretical value, i.e., 71% in the case of 97% titanium alkoxide, corresponds to the formation of TiO₂ [98]. Decrease in sample weight mostly occurs below 200°C and there is no appreciable weight loss beyond 600°C. On the other hand, the DTA plot clearly shows one endothermic peak at about 110°C and two exothermic peaks at about 280°C and 420°C.

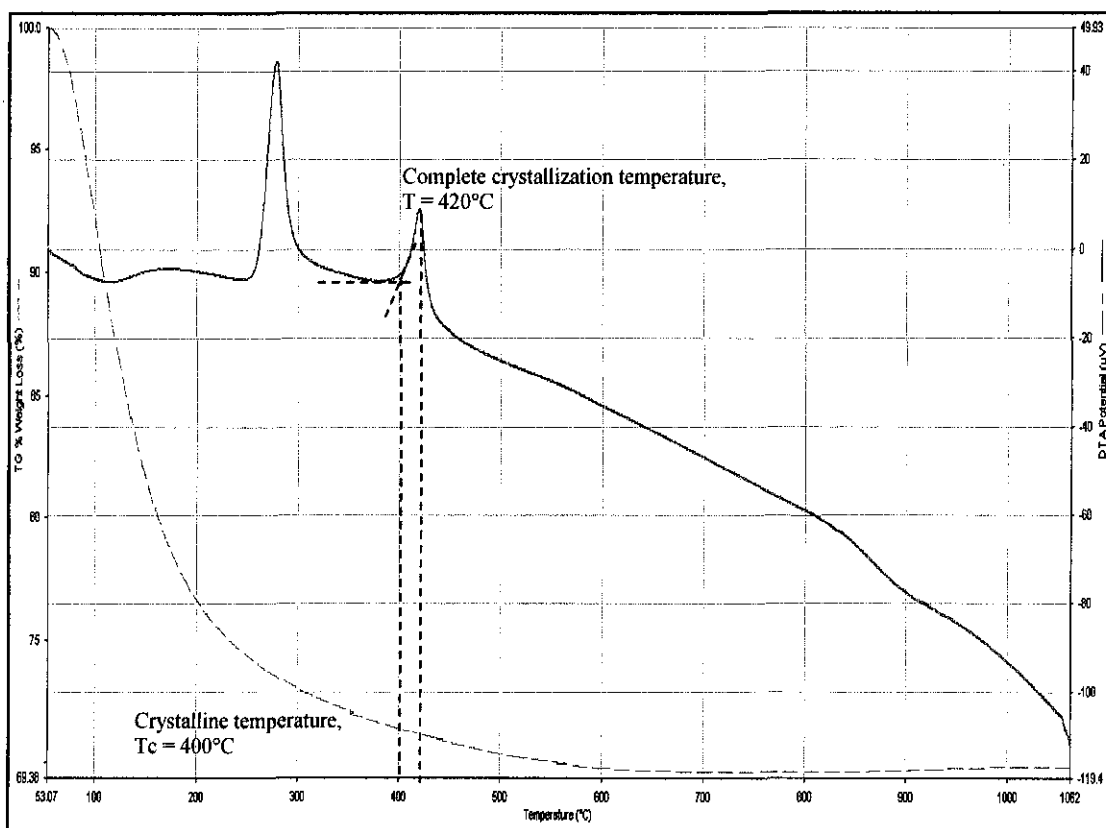


Figure 4.1: TG-DTA curve of the synthesized TiO_2 precursor at heating rate of $10^\circ\text{C}/\text{min}$ under flowing nitrogen gas.

The major part of weight loss appeared at temperature below 200°C together with small endothermic peak with an area of $1114.9 \mu\text{V}\cdot\text{sec}$ was due to the attribution of water molecules desorption [98-100]. Meanwhile, the corresponding exothermic peak examined at 280°C with an area of $-5769.9 \mu\text{V}\cdot\text{sec}$ indicates the decomposition of alkoxide bulky group. The DTA curve obtained also confirmed that the synthesized TiO_2 photoelectrode material was initially amorphous and transformed to crystalline form [98-100], showing small exothermic peak at about 400°C to 450°C and an area under the curve of $-2491.8 \mu\text{V}\cdot\text{sec}$. Hence, crystallization should have indeed occurred after heating at 400°C .

From the DTA curve obtained, the crystallization temperature (T_c) can be determined by measuring the intersection of the tangent to the maximum rising slope of the peak and the extrapolated sample baseline [97] which is about 400°C . The exothermic peak at 420°C with intensity of about $10 \mu\text{V}$ in the DTA curve indicating complete phase transition from amorphous to crystalline anatase phase. Hence,

referring to the TG-DTA data alone, the minimum calcination temperature to produce crystalline anatase phase of the prepared TiO_2 photoelectrode material is about 420°C . Nevertheless, XRD phase identification analysis need to be done to verified and support the finding.

SEM analysis was done to evaluate the morphology and microstructure of the samples. Figure 4.2 shows the images of P-25 (Figure 4.2a) at 100KX, TiO_2 -MERCK (Figure 4.2b) at 50KX and synthesized TiO_2 nanoparticles (Figure 4.2c) at 200KX obtained by SEM. Based on the images, it is clear that all samples reveal nanoparticles structure with different size. P-25 and synthesized TiO_2 shown approximately similar size while TiO_2 -MERCK exhibit an obviously bigger structure. Clear grain boundaries can also be observed for TiO_2 -MERCK sample which indicates better crystallite structure compared to other samples.

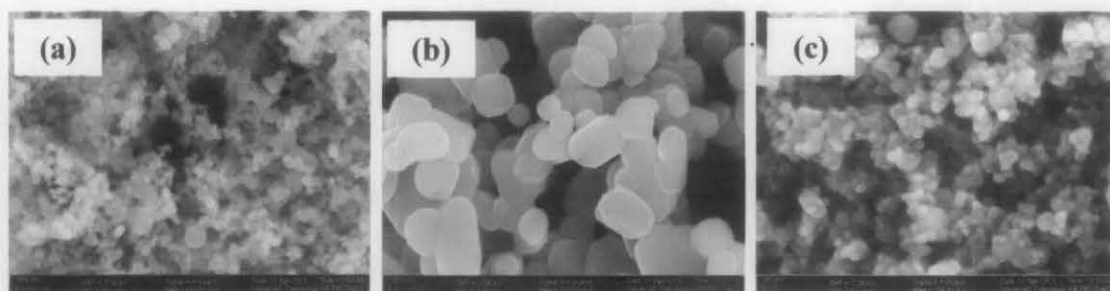


Figure 4.2: SEM images of (a) P-25 at 100KX (b) TiO_2 -MERCK at 100KX and (c) synthesized TiO_2 nanoparticles at 200KX.

The XRD patterns of all three types of TiO_2 nanoparticles (P-25, TiO_2 MERCK and synthesized TiO_2) are shown in Figure 4.3. Diffraction signal with Miller indices corresponding to the anatase structure; (d_{101}) at 25.3° , (d_{103}) at 36.9° , (d_{004}) at 37.8° , (d_{112}) at 38.6° , (d_{200}) at 48.1° , (d_{105}) at 53.9° , (d_{211}) at 55.1° , (d_{213}) at 62.1° , (d_{204}) at 62.7° , (d_{116}) at 68.7° , (d_{220}) at 70.3° and (d_{215}) at 74.1° [67, 101] is clearly observed in all three samples. The diffraction signal at 27.4° which correspond to rutile phase with Miller indices (d_{110}) [92] is not observed in other samples except for P-25. Based on the intensity ratio of P-25 diffraction peaks, it can be estimated that the content of rutile phase in the samples is approximately 20%.

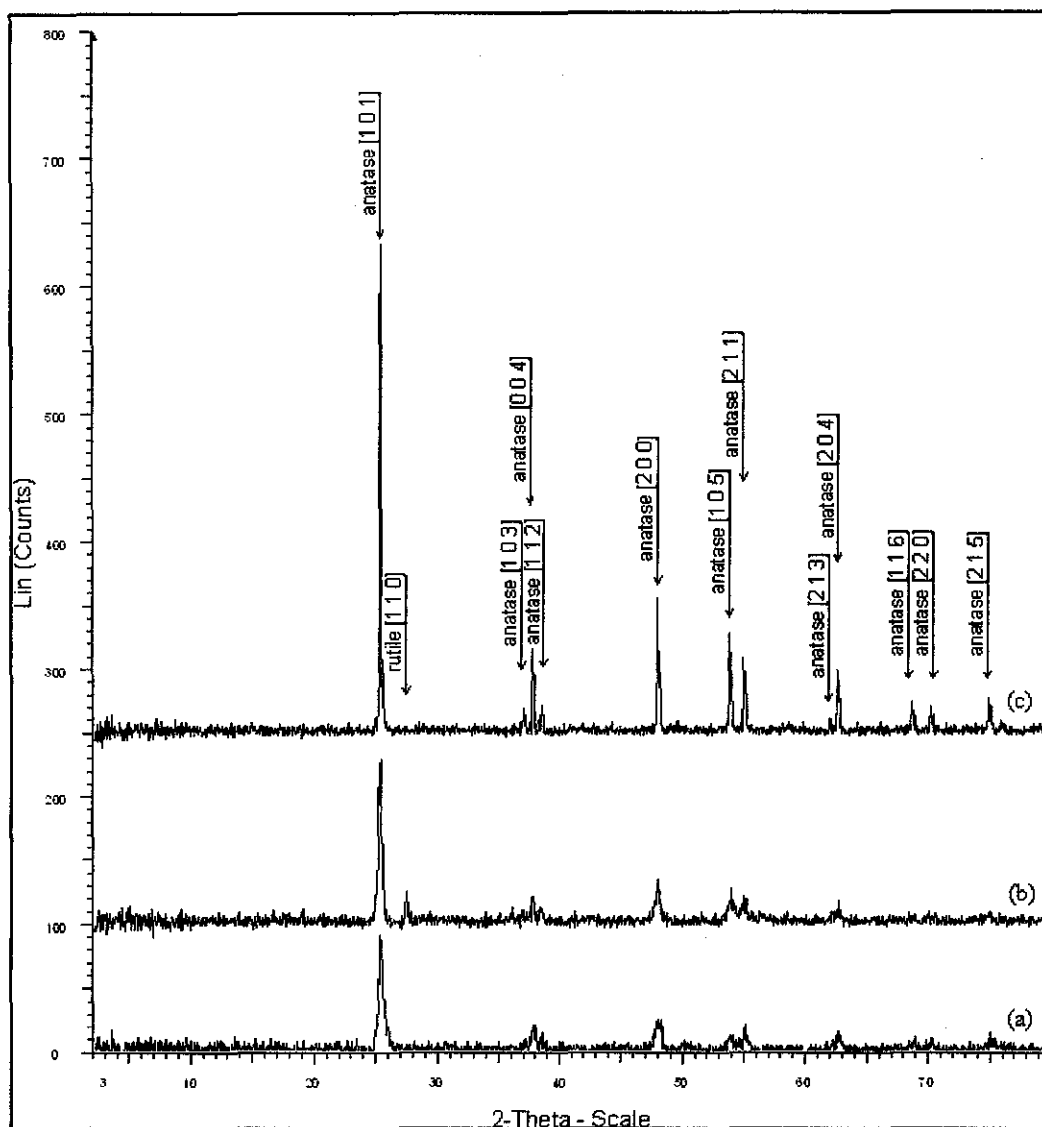


Figure 4.3: XRD pattern of (a) synthesized TiO_2 (b) P-25 and (c) TiO_2 -MERCK samples

Comparing the peaks width and intensity of samples diffraction signals, TiO_2 -MERCK reveal highest diffraction intensity followed by P-25 while synthesized TiO_2 shows the lowest intensity. This indicates that TiO_2 -MERCK sample have the highest crystallinity compared to other samples. However, the synthesized TiO_2 samples exhibit highest full-width half maxima (FWHM) of the diffraction peaks which correspond to the size of nanoparticle. The wider the FWHM, the smaller the sample size [102]. Table 4.1 summarized the data obtained from the XRD analysis together with the size of nanoparticles estimated using Scherer's formula. Based on the tabulated data, the P-25 and the synthesized sample exhibit approximately same size

of crystallite anatase. However, P-25 exhibit rutile phase with crystallite size of about 44.52 nm while TiO₂-MERCK are in the form of pure anatase phase with average size of about 56.0 nm. This result agrees well with the SEM images observed earlier.

Table 4.1: Intensity (counts), FWHM, d-spacing, and crystallite size of anatase TiO₂ at (*d*₁₀₁) plane while at (*d*₁₁₀) plane for rutile

Parameter	P-25		TiO ₂ -MERCK	Synthesized TiO ₂
Phase Present	Anatase	Rutile	Anatase	Anatase
Intensity (counts)	128	22.6	136.2	79.6
FWHM, β	0.354	0.192	0.152	0.485
d-spacing (Å)	3.510	3.252	3.524	3.524
Crystallite size (nm)	24.05	44.52	56.00	17.55

4.1.2 Optical Properties of P-25, TiO₂-MERCK and Synthesized TiO₂ Nanoparticles

Optical absorption spectra of all three types of TiO₂ nanoparticles films with adsorbed dye as shown in Figure 4.4 reflect the difference in their capabilities to absorb light. Based on the absorption spectra, the absorption wavelength below 390 nm for all samples was attributed to the intrinsic absorption of TiO₂ semiconductor material owing to electron transfer from valence band to the conduction band [28, 29]. In contrast, absorption wavelength above 400 nm corresponded to the dye molecules adsorbed on the surface of TiO₂ and is photoelectrode structure related [28, 29].

The photoelectrode film made from of TiO₂-MERCK shows the highest intensity above 400 nm. This was due to the presence of large nanoparticles, induces more effective photon capturing in the visible region. The phenomena also suggest the presence of strong scattering effect [28, 29]. Comparing P-25 and synthesized TiO₂ films, both photoelectrode films show similar absorption pattern with an absorption peak centered at about 530 nm, corresponding to the visible metal-to-ligand charge transfer (MTLC) transition (4d- π^*). Generally, the absorption band for the tetrahedral symmetry of Ti⁴⁺ appears at approximately 350 nm. However, based on the UV-Vis absorption pattern in Figure 4.4, the spectrum of P-25 film was stronger and red-shifted up to 530 nm of wavelength. The band gap of a semiconductor material is closely related to the wavelength range absorbed, where the band gap decreases with

increasing absorption wavelength [67]. Thus, this suggests that the band gap of P-25 sample is smaller than synthesized TiO_2 sample which result in better photoactivity.

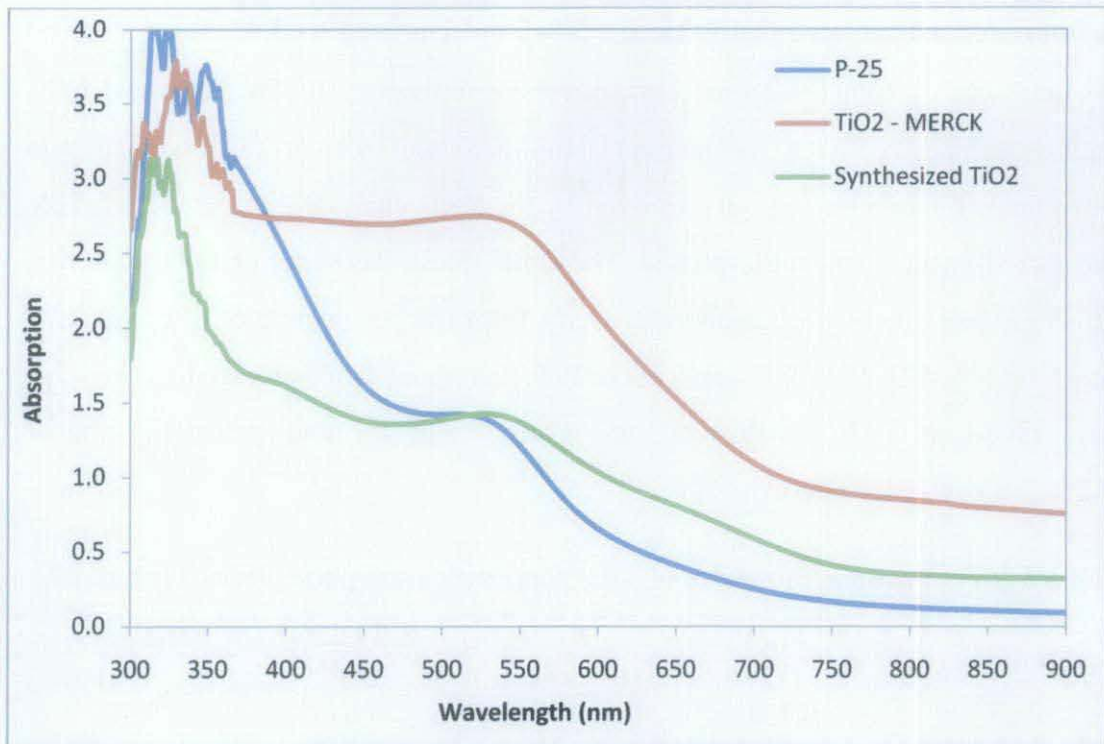


Figure 4.4: Optical absorption of N719 dye absorbed on TiO_2 films

4.1.3 Performance of DSC based on P-25, TiO_2 -MERCK and Synthesized TiO_2 Nanoparticles

To verify the performance of the DSCs, test cells consisting of P-25, TiO_2 -MERCK and synthesized TiO_2 nanoparticles as photoelectrode material were assembled and tested under illumination with 100 mW/cm^2 intensity. Figure 4.5 compares the I - V characteristics while Table 4.2 summarizes the measured data obtained from the I - V curves and calculated values based on Equation 3.5 and 3.6 of each solar cell. Based on the tabulated data, it can be seen that the most notable trend is short circuit current (I_{sc}) and efficiency (η), which correlate to the nanoparticles size and phases presence. On the other hand, there are not much difference in the open circuit voltage (V_{oc}) and fill factor (FF) of all samples as expected since all of the photoelectrode films were prepared in the same manner, therefore resulting in the same particles packing [103].

Based on Table 4.2 and Figure 4.5, the DSC integrated with synthesized TiO₂ nanoparticles showed higher I_{sc} (7.358 mA/cm²) and η (3.545%) compared with the one integrated with commercial P-25 (I_{sc} = 5.840 mA.cm⁻² and η = 3.421%) at identical film thickness of about ~12 μ m. The conversion efficiency of the integrated DSC based on synthesized TiO₂ nanoparticles was increased by over 3.6% compared to that of the cell based on P-25. It is proven by the XRD analysis that the P-25 sample have mixed anatase and rutile phases. The rutile phase has superior light-scattering characteristics, which is a beneficial property from the perspective of effective light harvesting [46, 92]. For DSC application, however, anatase is perceived as the most active phase of TiO₂ because of its surface chemistry and potentially higher conduction-band edge energy [46].

Table 4.2: Photovoltaic properties of TiO₂ nanoparticles as photoelectrode material.

Samples	V_{oc} (V)	I_{sc} (mA.cm ⁻²)	Fill Factor (FF)	Efficiency, η (%)
P-25	0.763	5.840	0.675	3.421
TiO ₂ -MERCK	0.798	2.181	0.543	1.073
Synthesized TiO ₂	0.720	7.358	0.589	3.545

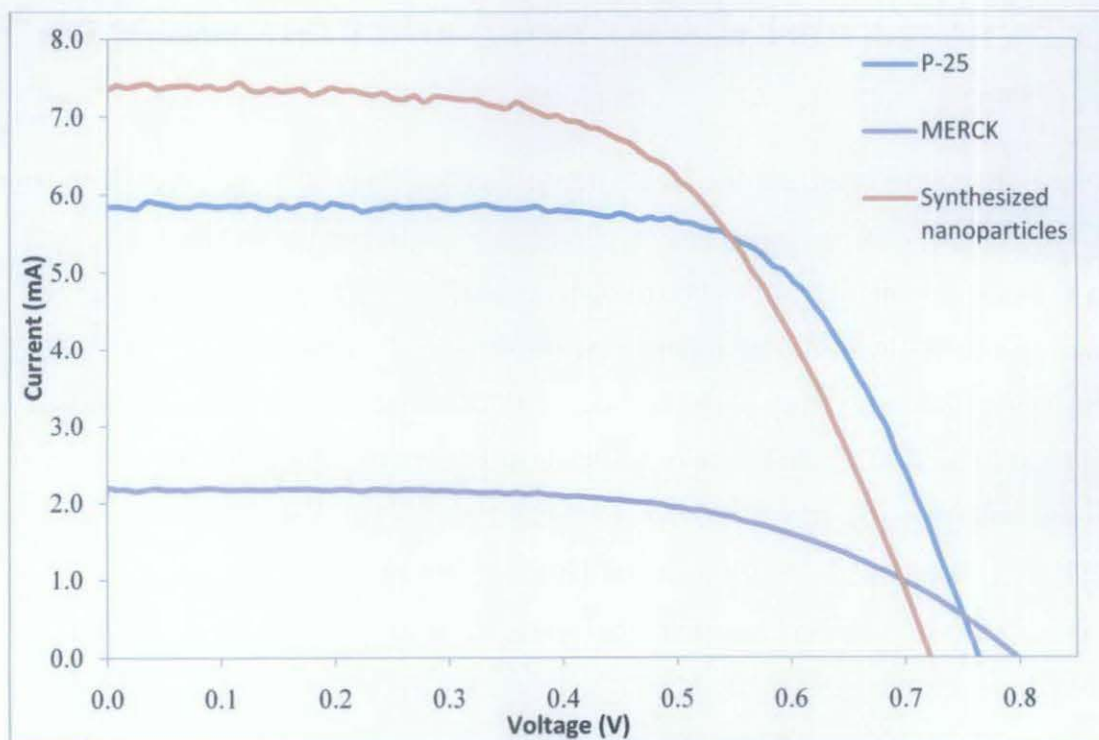


Figure 4.5: I - V plot of DSC integrated with different types of photoelectrode material.

Comparing the DSC integrated with TiO₂-MERCK and synthesized TiO₂ nanoparticles, it is clear that synthesized TiO₂ nanoparticles which have smaller nanoparticles size resulted in higher I_{sc} and η ; 7.358 mA/cm² and 3.545%, respectively. The decreasing in trend in I_{sc} and η relative to the increasing in particle size was due to the lower specific surface area available for dye chemisorptions. It is well known that the new physical and chemical properties emerge when the size of particles reduced to nanometers, which can result in dramatically increased surface area. Increasing specific surface area results in more dye adsorption due to the presence of larger contact points for easier access of the dye, which would increase the electron generation.

The TiO₂-MERCK based DSC shows the lowest performance efficiency even though it exhibits the highest light absorption intensity as illustrate in Figure 4.4. It is known that TiO₂-MERCK based photoelectrode film consists of larger nanoparticles compared to P-25 and synthesized TiO₂ nanoparticles, thus exhibit superior light scattering effect compared to the other samples as evidence in Figure 4.4. The light scattering could extend the travel distance of light in the photoelectrode films thus increase the chances of incidence photon being captured by the sensitized dyes. However, larger nanoparticles size will result in decreasing the specific area for dye chemisorptions which means the smaller the surface area of TiO₂, lesser the amount of anchored dye. Thus, not all incidence photon were used to excite the dye and produce free electrons which will then results in low performance efficiency of TiO₂-MERCK based DSC. This result clearly shows that both scattering effect and amount of anchored dye on the surface of photoelectrode films are important for high efficient DSC performance.

To prove that the surface area of photoelectrode films would affect the amount of anchored dye, the optical analysis of the N719 dye desorption from each printed TiO₂ nanoparticles films was done. The result is shown in Figure 4.6. It can be seen that all of these dye solutions present three absorption peaks at wavelengths of 310 nm, 372 nm and 509 nm, corresponding to the characteristic absorption of the N719 dye [104]. From the result, solution with desorbed-dye from synthesized TiO₂ film shows

the highest intensity followed with P-25 while TiO₂-MERCK sample exhibits the lowest absorption intensity.

It is known that, the absorption intensity was a result of dye concentration in the tested solution. Hence, from the optical absorption analysis, it is clear that the TiO₂-MERCK film absorb lesser dye compared to P-25, and synthesized TiO₂ nanoparticles due to the presence of larger particles size, that provide lower surface area for dye chemisorptions, resulting in lower electron generation. This decreasing in electron generation with increasing particles size is evident by the decreasing I_{sc} , as previously indicated.

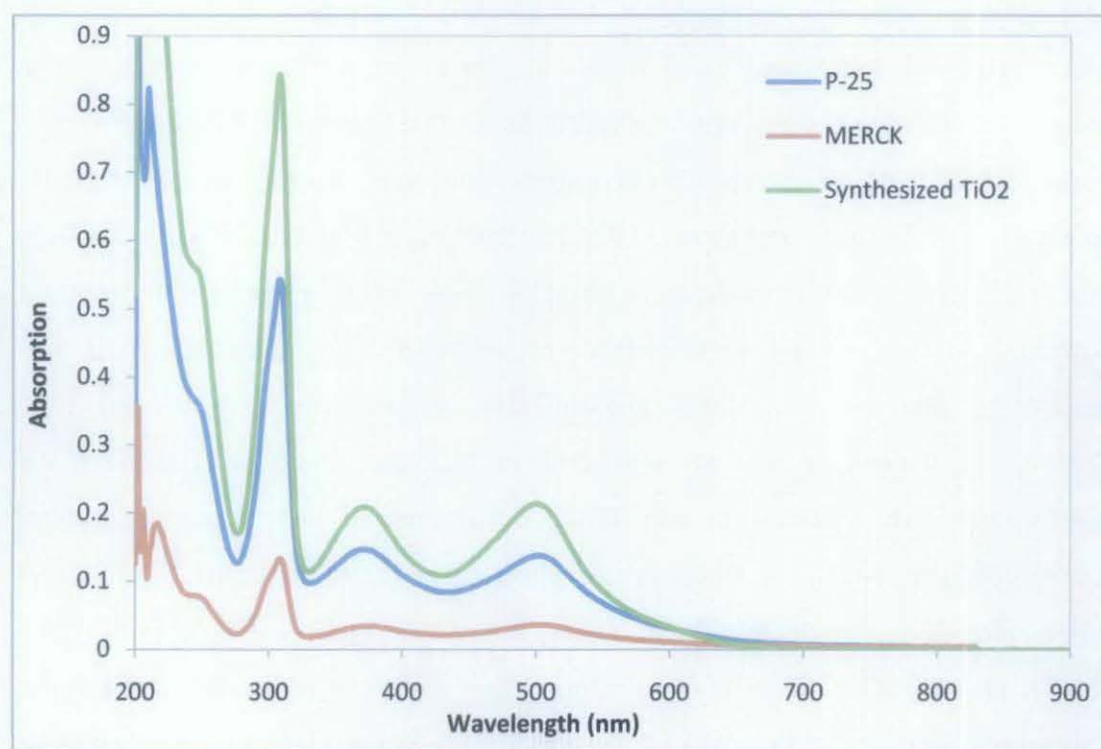


Figure 4.6: UV-Vis absorption of desorbed-dye solution

The performance of dye solar cells is highly influence by the scattering effect, specific surface area of TiO₂ photoelectrode material and the phase composition present. Photoelectrode films made up with smaller nanoparticels provide large surface area which allow for greater dye adsorption [30, 33, 34, 103]. On the other hand, by using TiO₂ with size ~100 nm as phototelectrode material have an advantage in introducing light scattering effect [22, 29, 35, 90]. However, utilizing either smaller or larger nanoparticles has disadvantages as well. TiO₂ photoelectrode films using

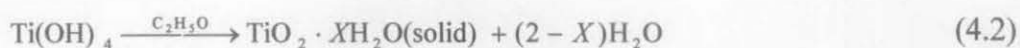
nanoparticles usually have high transparency and negligible light scattering due to the small particle size which results in poor light harvesting whilst, introducing larger particles with a lower specific surface area hinders dye adsorption and increases the electron diffusion path and consequently, increases the recombination rate of photogenerated carriers rather than enhancing the effect of light scattering [33, 34].

4.2 Development of TiO₂ Aggregates Photoelectrode Material in Dye Solar Cells (DSCs)

In this study, the TiO₂ aggregates were synthesized from diluted titanium alkoxide solution as precursor. The process is described by the following reaction [32, 75, 87, 89, 105]:



The reaction (4.1) will produce Ti(OH)₄. This will followed by condensation reaction as expressed by chemical reaction of (4.2), eliminating water to give TiO₂ colloid [32, 75, 87, 89, 105]:



The formation mechanism of the synthesized TiO₂ aggregates involves two stages which are nucleation and growth. Figure 4.7 shows the model of formation as suggested by Jongsoo and co workers [106]. During the initial stage, solutes are formed to yield a supersaturated solution, leading to nucleation. The formed nuclei were then further grow by diffusive mechanism resulting in formation of nanocrystallites. In an appropriate chemical condition (ionic strength), the submicron aggregates will form through diffusion-controlled process.

This subsection will discuss the influence of two critical process parameters; percentage of water content in ethanol solution and calcination temperature on the size of submicron aggregates and primary nanocrystallite, degree of aggregation, phase present, specific surface area and pore size distribution. The dependency of structure-properties relationship of the synthesized samples on the performance of DSCs was verified using IV-characterization.

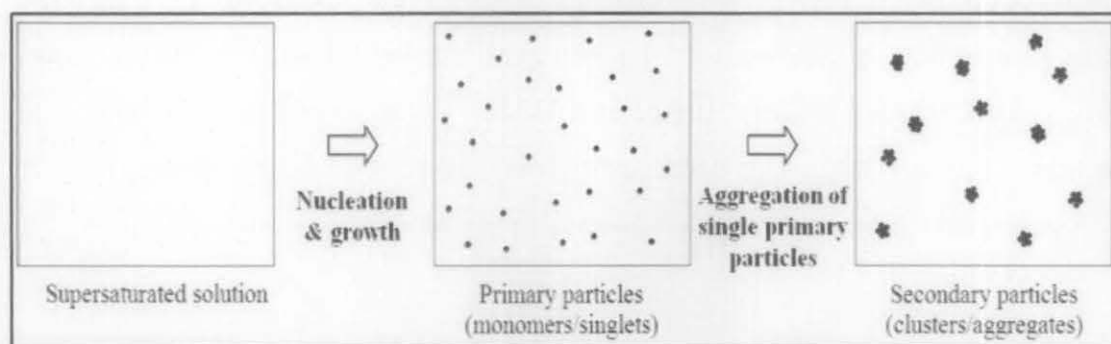


Figure 4.7: Illustration of formation mechanism of TiO₂ aggregates as suggested by Park et al. [106].

4.2.1 Effect of Water Content in Hydrolysis Process

To examine the effect of percentage of water in ethanol solution, the samples were synthesized by using 0.2 M titanium alkoxide in 0.9-3.6 vol% of water in ethanol solution. A water percentage of 0.9 vol% was taken as the lowest since reducing the reagent concentration will diminish the yield of precipitation below 70% [87, 88]. Moreover, the dilute alkoxide solution in ethanol is stable for months without the presence of water.

4.2.1.1 Physico-chemical Properties

The scanning electron microscopy (SEM) morphology and microstructure of TiO₂ aggregates synthesized at various percentage of water contents at two different magnification (10 KX and 150 KX) were shown in Figure 4.8Figure 4.11(a) and (b); Figure 4.8Figure 4.11(c) are the size distribution histogram fitted by log-normal distribution function of the respective synthesized samples.

It can be seen that the synthesized samples are in the form of submicron-sized aggregates and made up of smaller nanocrystallites. The aggregate size distribution correlates with the amount of water present during hydrolysis process in such a way that the size and standard deviation of the aggregates decrease with increasing percentage of water in ethanol solution. At low percentage of water content (0.9 vol% of water), aggregates with mean diameter of about 0.45 μm and standard deviation of 0.12 were clearly produced. With additional water content used to promote the

hydrolysis process, the aggregate size and standard deviation decreases to $0.39 \mu\text{m}$ and 0.09 at $1.8 \text{ vol}\%$, $0.29 \mu\text{m}$ and 0.06 at $2.7 \text{ vol}\%$, $0.20 \mu\text{m}$ and 0.05 at $3.6 \text{ vol}\%$ of water in ethanol solution, respectively. Smaller the value of standard deviation, narrower the aggregate size distribution.

Table 4.3 summarizes the mean size and standard deviation of the synthesized TiO_2 as a function of water content in absolute ethanol solution. Unlike aggregate, the size of primary nanocrystallites is too small to be determined by SEM, thus the need to be estimated by using XRD line broadening and Scherer formula.

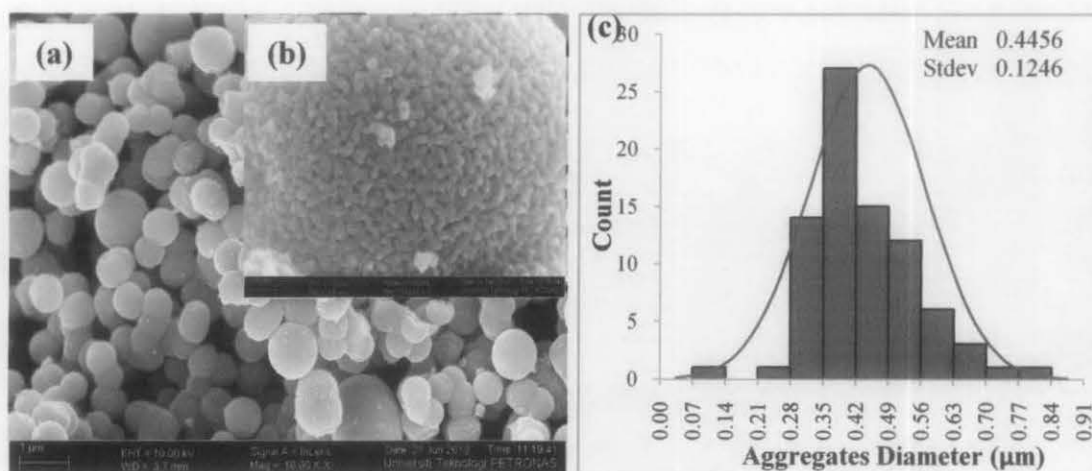


Figure 4.8: SEM image of synthesized TiO_2 with $0.9 \text{ vol}\%$ of H_2O at (a) 10 KX (b) 150 KX and (c) aggregates size distribution curve

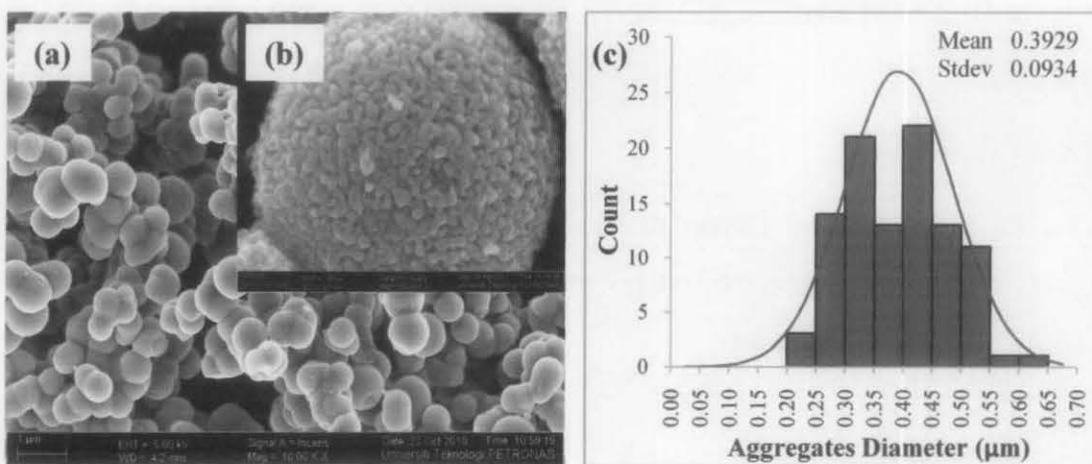


Figure 4.9: SEM image of synthesized TiO_2 with $1.8 \text{ vol}\%$ of H_2O at (a) 10 KX (b) 150 KX and (c) aggregates size distribution curve

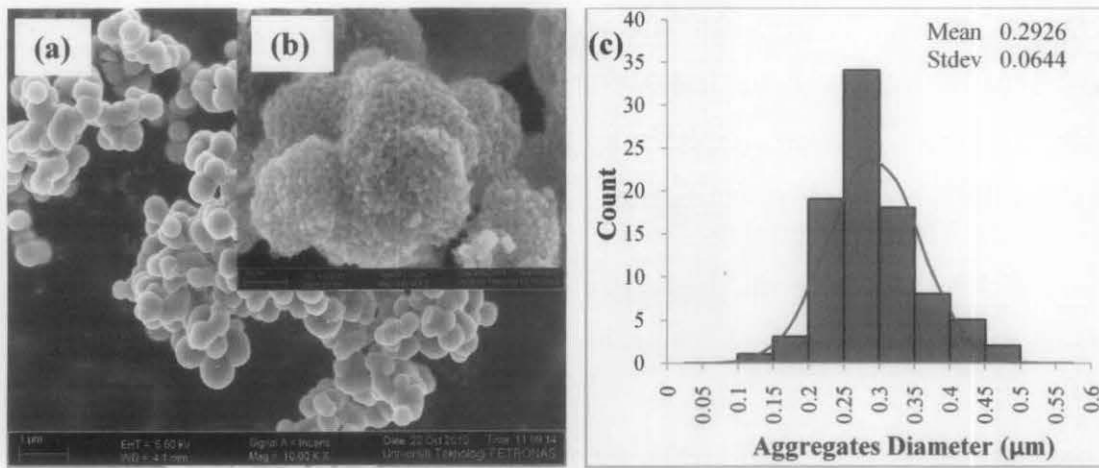


Figure 4.10: SEM image of synthesized TiO_2 with 2.7 vol% of H_2O at (a) 10 KX (b) 150 KX and (c) aggregates size distribution curve

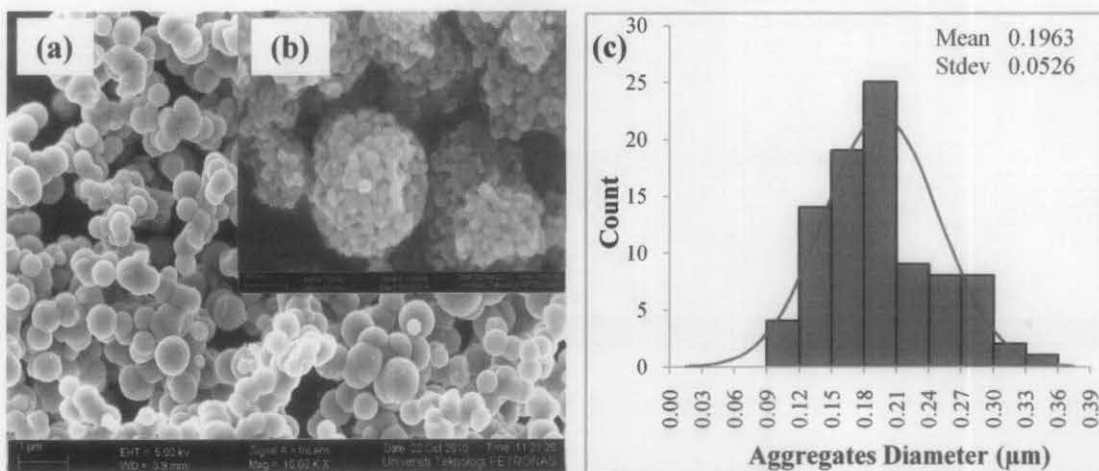


Figure 4.11: SEM image of synthesized TiO_2 with 3.6 vol% of H_2O at (a) 10 KX (b) 150 KX and (c) aggregates size distribution curve

Table 4.3: Mean size and standard deviation of the synthesized TiO_2 as a function of percentage of water content in ethanol solution.

Reagent		Mean Size (μm)	Standard Deviation
$\text{Ti}(\text{OC}_2\text{H}_5)_4$ (M)	H_2O (vol%)		
0.2	0.9	0.45	0.12
0.2	1.8	0.39	0.09
0.2	2.7	0.29	0.06
0.2	3.6	0.20	0.05

Another significant effect of the increasing water content is the deterioration of aggregation and the increase of the surface roughness as evident by SEM images in Figure 4.8, Figure 4.9, Figure 4.10 and Figure 4.11. Sample synthesized with 0.9 vol% water content exhibited aggregates with spherical shape and whilst sample prepared with higher percentage of water content demonstrated slight disintegration on the aggregation of nanocrystallites. Most of the TiO₂ aggregates samples produced with the highest percentage of water content (3.6 vol%) in hydrolysis, lost their spherical shape and likely decrease in the surface smoothness. This can be clearly seen in SEM image in Figure 4.11.

Figure 4.12 shows a typical XRD pattern of the TiO₂ aggregates made up of nanocrystallite synthesized through hydrolysis of diluted titanium alkoxide with 0.9 vol% to 3.6 vol% of water in ethanol solution. All of the samples were calcined at temperature 420°C according to TG-DTA result obtained earlier. The samples were soaked at 420°C for two hrs to ensure complete calcination process. The pattern confirmed the formation of anatase phase for all samples regardless of the different percentage of water content used during hydrolysis. They exhibit peaks corresponding to the formation of crystalline anatase TiO₂ phase with Miller indices of (*d*₁₀₁), (*d*₁₀₃), (*d*₀₀₄), (*d*₁₁₂), (*d*₂₀₀), (*d*₁₀₅), (*d*₂₁₁), and (*d*₂₀₄) at 25.3°, 36.9°, 37.8°, 38.6°, 48.1°, 53.9°, 55.1°, 62.1° and 62.7° of 2θ respectively [67, 101]. Table 4.4 summarizes the information obtained from the XRD characterization including phase present, intensity, FWHM and d-spacing as a function of percentage of water content in ethanol solution. The Scherer's formula and Bragg's law (Equation 3.3 and 3.4) together with XRD line broadening were used to estimate the nanocrystallite size of each sample.

It is shown that as water concentration increases, the intensity increases suggesting an increase in crystallinity. On the other hand, there is no significant difference in the width of the diffraction peaks as the percentage of water content increases. The peak width is a result of crystallites size [102]. This implies that the nanocrystallite size of the prepared samples was not affected by the percentage of the water content added during hydrolysis process. Based on Scherer's formula, calculated nanocrystallites size was estimated to be of about 10 nm with deviation of

± 3 nm as tabulated in Table 4.4. This result supported the earlier theory and proved that the initial water content used during hydrolysis process have no significant effect on the growth of nanocrystallites which made up the aggregates, yet affect the size and degree of spherical aggregation TiO_2 .

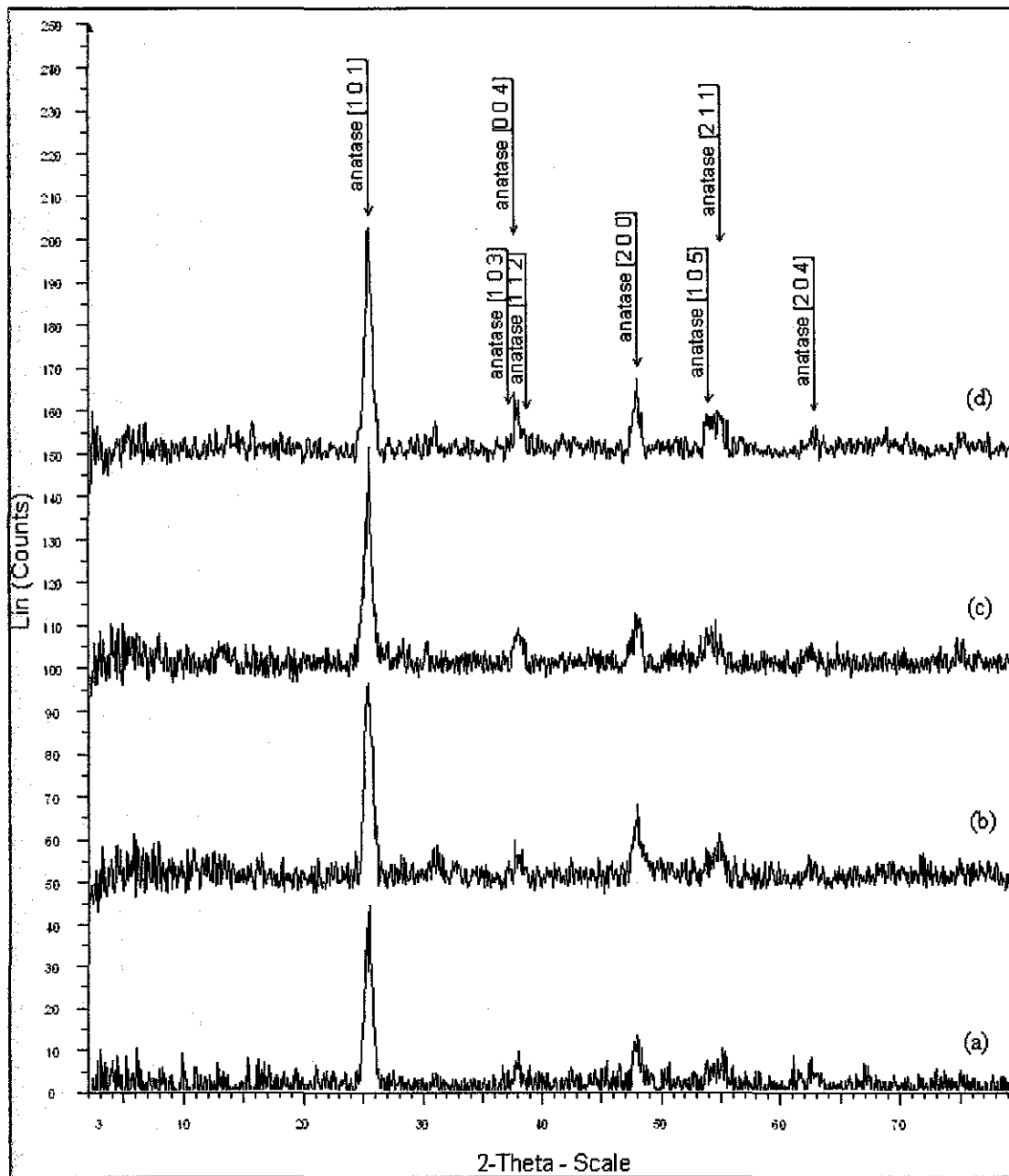


Figure 4.12: XRD pattern of synthesized TiO_2 photoelectrode material hydrolyzed with (a) 0.9 vol% (b) 1.8 vol% (c) 2.7 vol% and (d) 3.6 vol% of water in ethanol solution.

Table 4.4: Intensity (counts), FWHM, d-spacing, and crystallite size of anatase TiO₂ phase at (*d*₁₀₁) plane

Parameter	Percentage of Water (vol%)			
	0.9	1.8	2.7	3.6
Phase Present	Anatase	Anatase	Anatase	Anatase
Intensity (counts)	37.4	43.8	46.3	52.3
FWHM, β	0.774	0.856	0.645	0.694
d-spacing (Å)	3.507	3.515	3.504	3.508
Crystallite size (nm)	11	10	13	12

Surface area and porosity are two other factors that can influence the photovoltaic performance of DSCs. The large surface area is important for absorbing the dye while optimizing the size of pores could ensure that the redox electrolyte can efficiently penetrate and be present in the place of the dye. This condition will optimize the regeneration of the oxidized dye and charge transport [107]. Hence, BET-BJH analysis [108, 109] was performed and the result was tabulated in Table 4.5. Figure 4.13 compares the nitrogen sorption isotherms of synthesized TiO₂ aggregate at different water percentage while Figure 4.14 shows the corresponding pore size distribution of each sample.

Based on the typical nitrogen adsorption isotherms, all four synthesized TiO₂ aggregates showed a type IV pattern with an inflection of nitrogen adsorbed volume at a high relative pressure, P/P_0 of 0.7-0.9. This type of pattern indicates the nature of mesoporous TiO₂ structures [85, 110]. The BET surface area of the synthesized samples decreases from 75.56 m²g⁻¹ to 62.75 m²g⁻¹, 54.23 m²g⁻¹ and 49.14 m²g⁻¹ as the percentage of water content in ethanol solution increases from 0.9 vol% to 1.8 vol%, 2.7 vol% and 3.6 vol%, respectively. On the other hand, the average pore size of the synthesized samples is directly proportional to the percentage of water content used. At low percentage of water (0.9 vol%), the sample exhibits the lowest average pore size of 10.9 nm. The average pore size increase to 12.4 nm, 15.6 nm and 17.1 nm as the percentage of water increase to 1.8 vol%, 2.7 vol% and 3.6 vol%, respectively. Nevertheless, increase in the percentage of water had no significant influence on the samples pore volume.

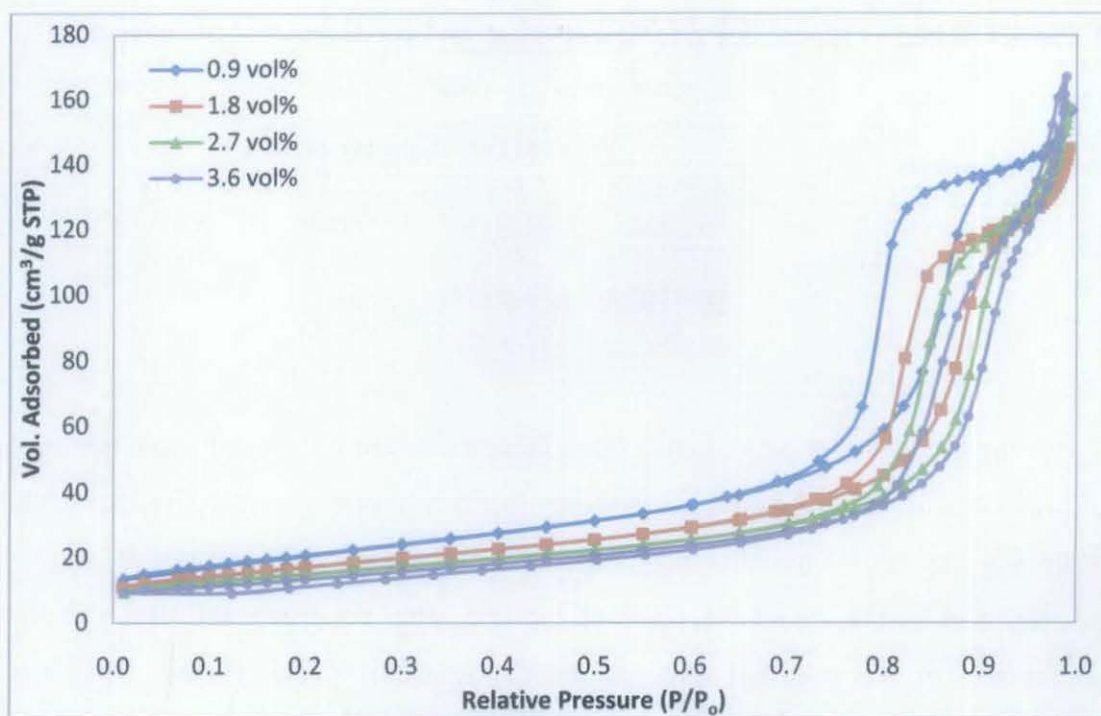


Figure 4.13: Nitrogen adsorption and desorption isotherm of synthesized TiO_2 aggregate at different water percentage.

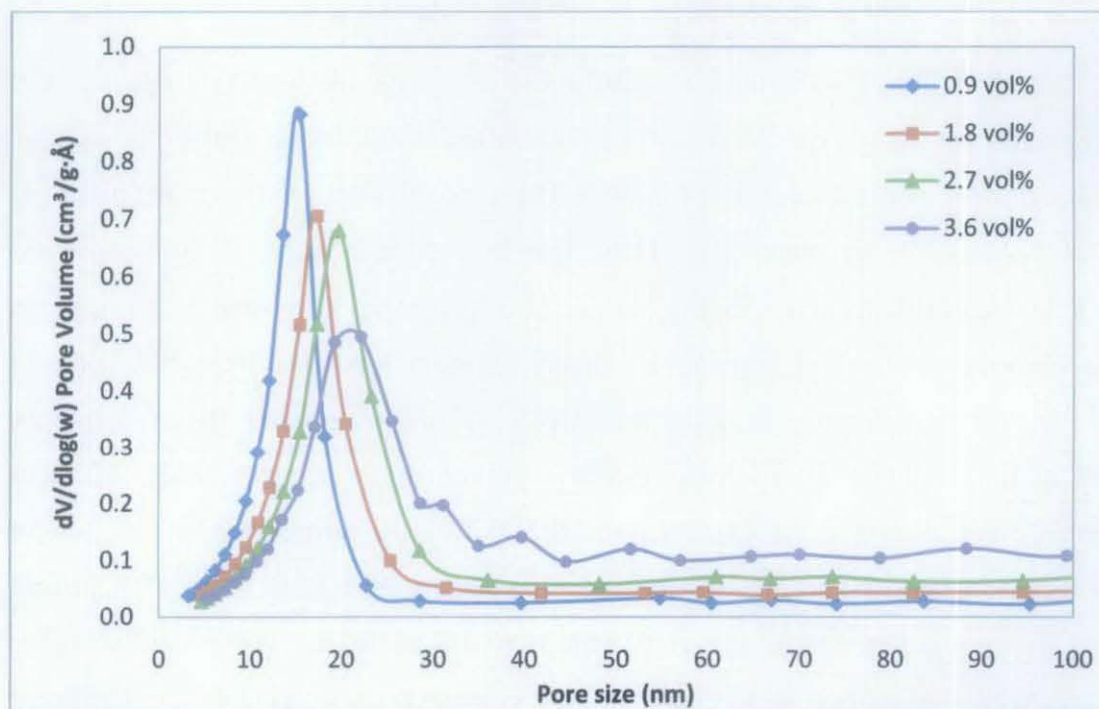


Figure 4.14: Pore size distribution of synthesized TiO_2 aggregate at different water percentage

Table 4.5: Surface area, pore volume and pore size of the synthesized TiO₂ as a function of water percentage in ethanol solution.

Percent of H ₂ O (vol%)	S _{BET} (m ² g ⁻¹)	Pore Volume (cm ³ g ⁻¹)	Pore Size (nm)
0.9	75.56	0.24	10.9
1.8	62.75	0.23	12.4
2.7	54.23	0.25	15.6
3.6	49.14	0.26	17.1

The corresponding pore-size distribution of the synthesized TiO₂ aggregates (Figure 4.14) shows the existence of bimodal pore size distribution; mesopores (2–50 nm) and macropores (50–193 nm). The bimodal structures signify the existence of the intra-aggregated pore (represented by the hysteresis loop in the lower P/P₀ range) and the inter-aggregated pore (hysteresis loop in the higher P/P₀ range) [111-115]. With increasing percentage of water content during hydrolysis process (from 0.9 vol% to 3.6 vol%), the maximum pore sizes of the intra-aggregated pores shift to larger mesopores regions, indicating the growth of pores [111] as shown in Table 4.5.

4.2.1.2 Performance Verifications

Figure 4.15 shows the *I-V* curve of DSCs based on photoelectrode films made of TiO₂ aggregates synthesized with 0.9-3.6 vol% of water in ethanol solution. The open circuit voltage (V_{oc}), short circuit current (I_{sc}), fill factor (FF) and performance efficiency (η) of the DSCs are also summarized in Table 4.6. Based on the results, increase in percentage of water content from 0.9-3.6 vol% forces the size of aggregates to reduce from 0.45 μm to 0.2 μm and losing the spherical aggregation, resulted in decreasing efficiency, η from 3.915% to 3.504%. Similarly, the same trend was observed for I_{sc} . DSC integrated with TiO₂ aggregates synthesized with 0.9 vol% of water content exhibits the highest I_{sc} (9.697 mA.cm⁻²) out of all samples. A result of 8.902 mA.cm⁻² is achieved by the sample prepared with 1.8 vol% of water content, 7.555 mA.cm⁻² by the sample of 2.7 vol% water content and 7.05 mA.cm⁻² by sample prepared with 3.6 vol% water content.

On the other hand, there is no significant difference for the measured V_{oc} of all integrated DSCs. V_{oc} is affected by the quasi Fermi level of electrons in the TiO₂ and

the energy of the iodide/tri-iodide redox couple system [16, 116]. Besides, the fill factor is another important parameter that can influence the performance efficiency of DSCs. Fill factor is closely related to the geometric structure of each individual cells and the transport mechanism of carriers through the device. Based on Table 4.6, the values of fill factor increased with the percentage of water content indicating better films packing. This trend is as expected since higher percentage of water content results in smaller standard deviation value (Table 4.3). Smaller deviation value of aggregates size will likely lead to a highly ordered structure and increased regularity in the assembly of films [39].

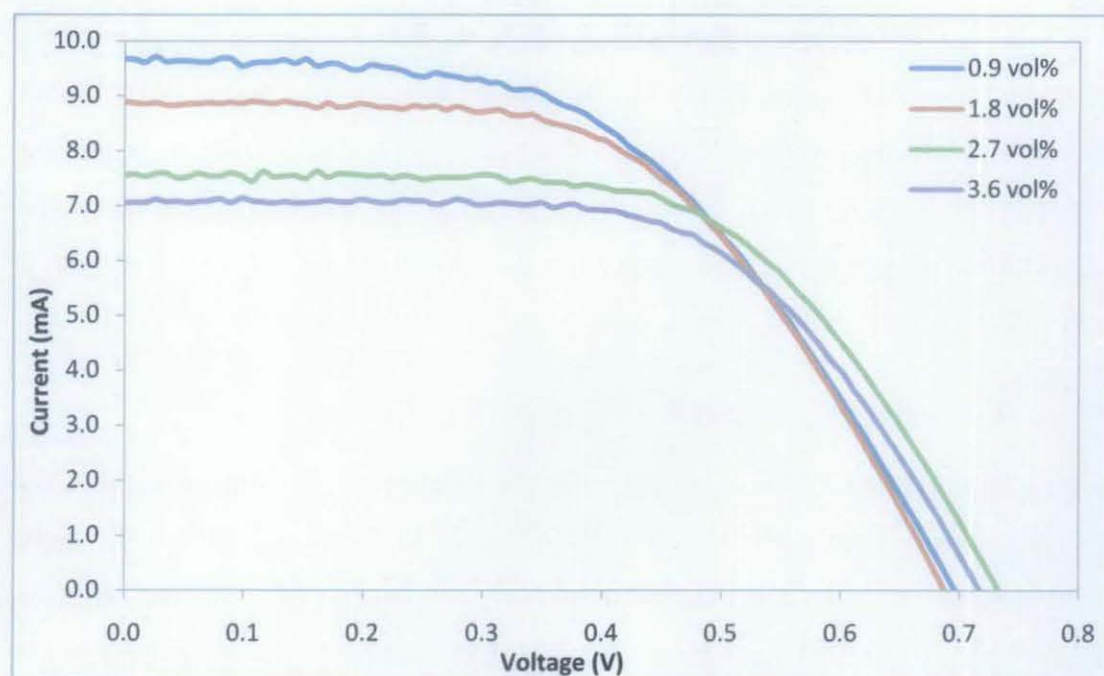


Figure 4.15: I - V curve of synthesized TiO_2 aggregates at various water percentage in ethanol solution.

Table 4.6: Photovoltaic properties of the synthesized TiO_2 aggregates as a function of water percentage in ethanol solution.

H_2O percentage (vol%)	V_{OC} (V)	I_{SC} ($\text{mA}\cdot\text{cm}^{-2}$)	Fill Factor (FF)	Efficiency, η (%)
0.9	0.698	9.697	0.510	3.915
1.8	0.685	8.902	0.554	3.837
2.7	0.733	7.555	0.597	3.757
3.6	0.715	7.050	0.612	3.504

Based on the theory and measured value, it is clear that the performance of the integrated DSCs was influenced by the I_{sc} , a direct result of the variant in aggregates size and degree of aggregation. The I_{sc} is dependent on the amount of photoexcited electron and charge recombination [39]. In the case of the integrated DSCs, the variation in the I_{sc} was contributed by the difference in the dye adsorption amount and/or the light harvesting efficiency of photoelectrode films. Based on the BET analysis, the specific surface area of the photoelectrode films decreased as the percentage of water content increases, resulting in decreasing amount of dye absorbed. Low amount of dye absorbed on the surface of TiO_2 films results in lower electron generation thus reducing the I_{sc} .

The light harvesting efficiency is another factor that could cause the difference in the I_{sc} , which basically depends on the extinction coefficient of the dye and the transport behavior of the light within the photoelectrode films. Since the same dye (N719) is used throughout the study, it is likely that the film structures with different aggregate size and degree of aggregation can lead to a significant impact on the light scattering which extend the light travelling within the films so as to affect the light harvesting efficiency [27, 29, 39]. To prove the presence of light scattering within the films, optical absorption spectra of the TiO_2 films consisting of aggregates with different size and degree of aggregation was analyzed using UV-Vis spectrophotometer. Figure 4.16 shows the optical absorption spectra of all four synthesized TiO_2 films sensitized with N719 dye with TCO glass as the baseline.

The result reveals that all of the samples exhibit an intrinsic absorption below 390 nm caused by the TiO_2 semiconductor with electron transfer from the valence band to the conduction band. On the other hand, absorption at wavelengths above 400 nm is due to the dye adsorbed on the surface of TiO_2 , and the difference in the absorption intensity implies that the absorption is structure related [27, 29, 39]. The highest intensity was obtained by the films made up of TiO_2 aggregates synthesized with 0.9 vol% of water content followed by 1.8 vol%, 2.7 vol% and 3.6 vol% which corresponding to the aggregate size of 0.45 μm , 0.39 μm , 0.29 μm and 0.20 μm , respectively.

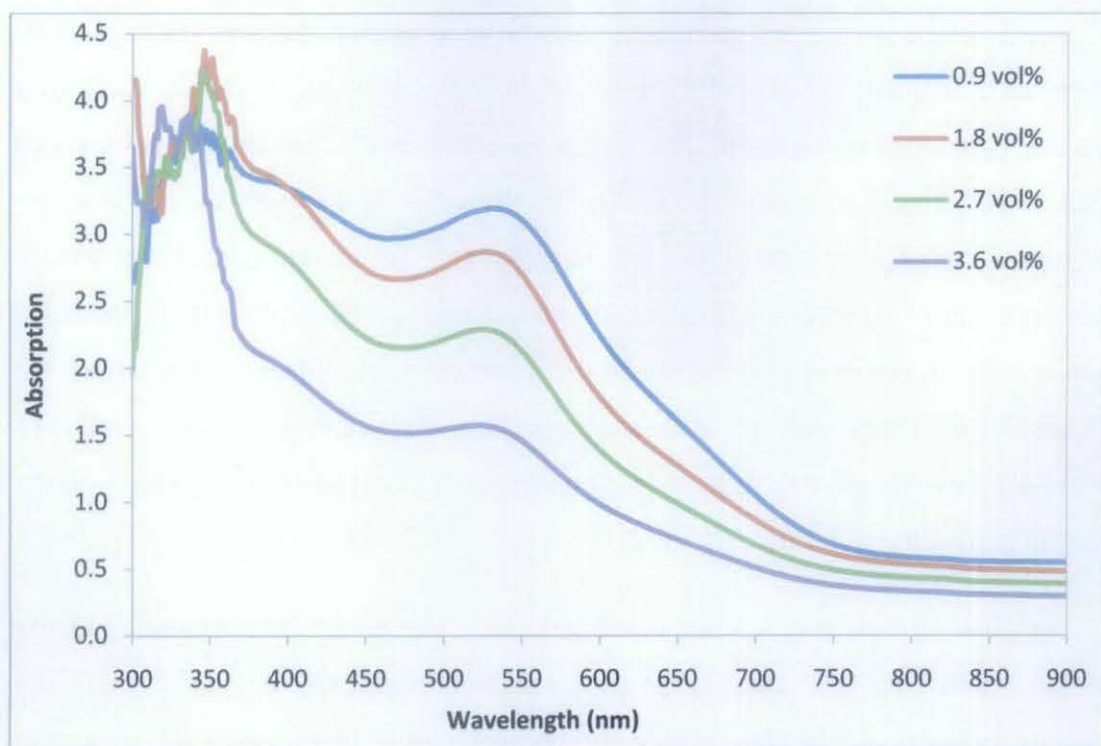


Figure 4.16: Optical absorption spectra of synthesized TiO_2 aggregates films

The difference in the absorption intensity in the visible region is attributed to the variation in the submicrometer-sized aggregates. Higher capability to absorb light weakens the transmittance of the films and causes pseudo absorption in the spectra [27, 29, 39]. The performance of the solar cell is improved due to the presence of light scattering in the integrated films, by which the traveling distance of light within the photoelectrode film can be significantly extended. As such, the opportunities for incident photons to be captured by the dye molecules are increased. The difference found in the optical absorption of the four types of film implies that improvement in the degree of aggregation of nanocrystallites would induce more effective light scattering in the visible region. A photon-localization effect may also occur in these films due to their highly disordered structure that confines the light scattering in closed loops [27, 29, 39].

To support the finding, the photocurrent action spectra analysis was done which display the wavelength distribution of incident monochromatic photon to current conversion efficiency (IPCE) and display in Figure 4.17. The photocurrent peaks occurring at approximately 340 nm, corresponding to energy of approximately 3.2 eV,

are due to direct light harvesting by TiO₂ semiconductor, in which the photon-generated electrons diffuse through TiO₂. The maxima of IPCE in the visible region contributed by the dye absorption are located at approximately 530 nm with values of 5.3%, 4.5%, 3.7% and 3.0% for samples synthesized with 0.9 vol%, 1.8 vol%, 2.7 vol% and 3.6 vol% of water, respectively. Comparing the action spectrum, samples synthesized with 0.9 vol% of water content shows a broader feature compared to other samples which was due to the effect of light scattering by the submicron-size aggregates [117]. The result of IPCE support the hypothesis of existing strong light scattering in the photoelectrode film made up with sample prepared at low water content (0.9 vol%) and as increasing the water content the scattering effect reduces.

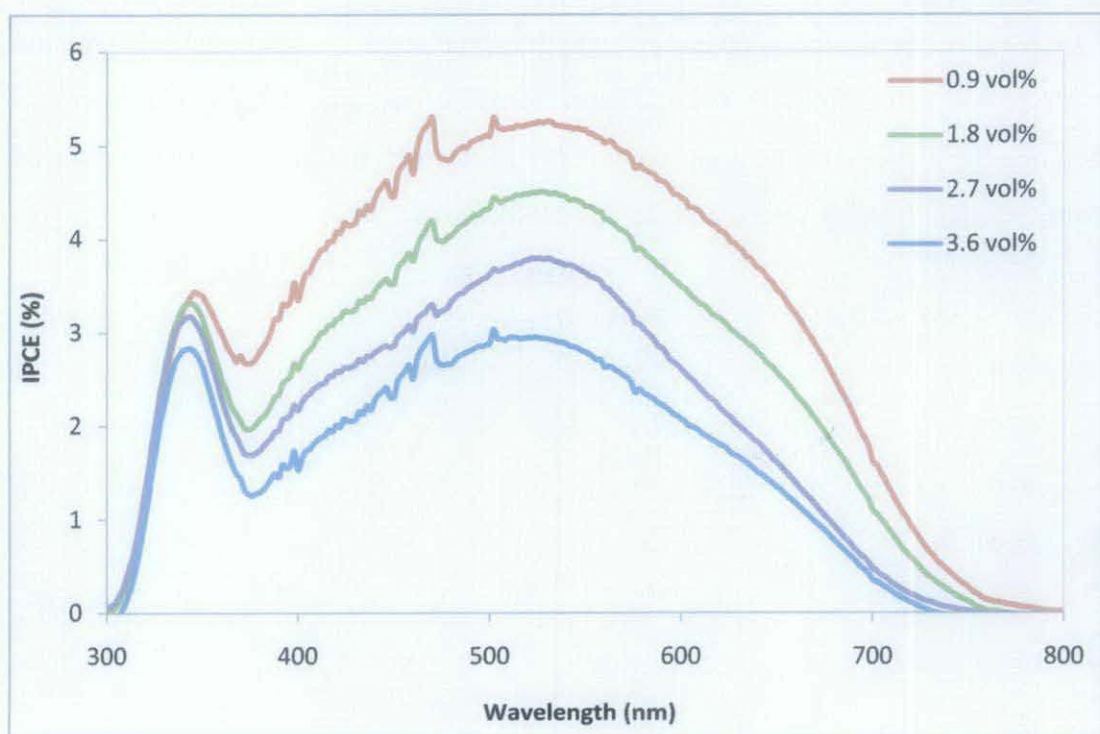


Figure 4.17: Photocurrent action spectra of the electrodes with synthesized TiO₂ aggregates structure

IPCE can be expressed in term of the light harvesting efficiency (LHE), the quantum yield of electron injection (ϕ_{inj}), and the collection means of injected electrons at the back contact (η_c) by mean of the Equation (4.3):

$$IPCE(\lambda) = LHE(\lambda) \cdot \phi_{inj} \cdot \eta_c \quad (4.3)$$

LHE at wavelength, λ can be estimated using the following equation (4.4) [118]:

$$LHE(\lambda) = 1 - 10^{-A} \quad (4.4)$$

where, A is the absorption of the dye on TiO_2 at the maximum wavelength.

Figure 4.18 shows the graph of LHE versus wavelength of corresponding synthesized TiO_2 aggregates films. Based on the result, the estimated LHE reach almost 100% up to 530 nm wavelength for all samples. Above 530 nm, the LHE decreases as the percentage of water content increases from 0.9 vol%, 1.8 vol%, 2.7 vol% to 3.6 vol% as a result of losing the spherical aggregation and decreasing in aggregate size from 0.45 μm , 0.39 μm , 0.29 μm to 0.20 μm , respectively. It is clear that, the variation in the LHE is due to the difference in the dye adsorption that contributes to an increase in the IPCE. The result signifies that improving the degree of aggregation of the photoelectrode would induce a better light scattering in the visible region and influences the transport behavior through changing the path and extending the distance of the light travel in the film which in turn increase the chances of interaction between photons and the dye molecules.

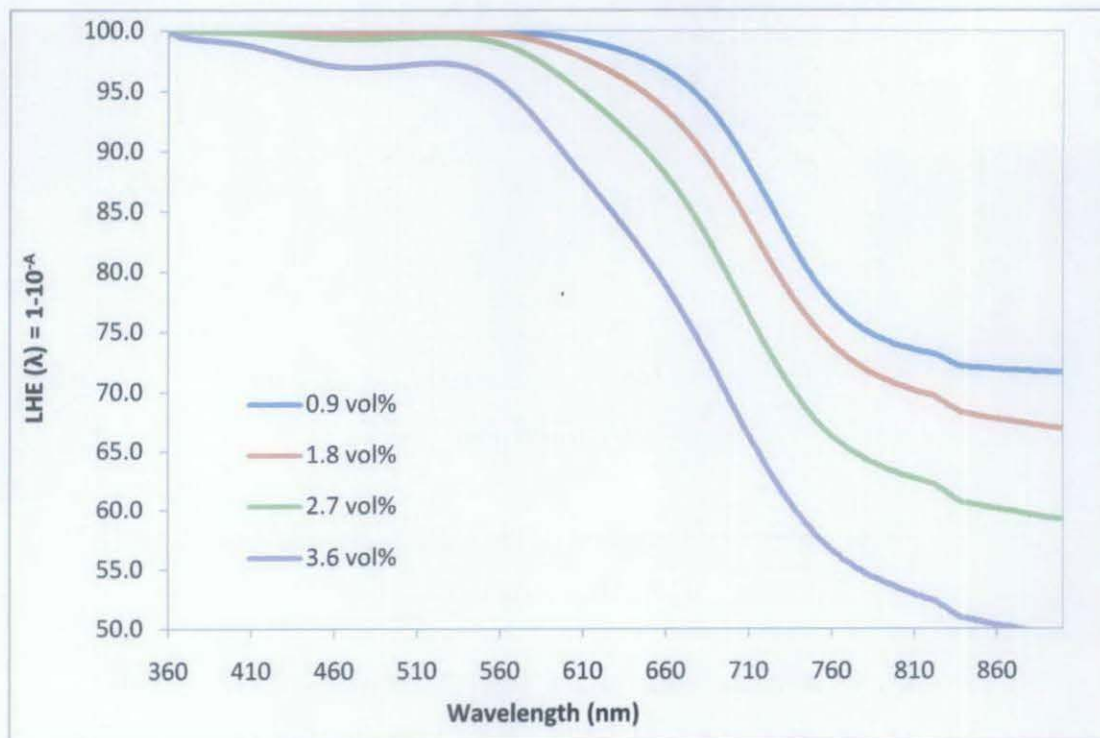


Figure 4.18: LHE versus wavelength

4.2.2 Effect of Calcination Temperature

To study the effect of calcination temperature, the samples were synthesized using 0.9 vol% of water in ethanol solution and calcined at four different temperatures, namely 400°C, 500°C, 600°C and 700°C for two hrs. The calcined samples were characterized and integrated into test cells to compare their performance efficiency. The aim of this study is to identify the optimum calcination temperature of TiO₂ aggregates photoelectrode material in order to develop an efficient TiO₂ aggregates-based DSC.

In this study, 400°C have been chosen as the lowest calcination temperature since based on the TG-DTA results discussed in previous section, the synthesized TiO₂ sample was in the form of amorphous and started to crystalline at the temperature of 400°C. According to Tang et al. [44], highly crystalline TiO₂-based DSC was more efficient in adsorbing dye compared to amorphous TiO₂-based DSC due to poor (101) facets to adsorb dye. The ability to absorb dye is one of the critical factors that need to be taken into consideration since it could affect the performance of DSCs. Thus, it is undesirable to calcine the samples below 400°C.

Calcined above 700°C is unfavorable for DSC application since high calcination temperature will favor the formation of rutile phase. Even though rutile phase has more stable crystal structure at high temperature, anatase phase performs better as photoelectrode in DSC. A comparative study on DSC made up of anatase and rutile-based photoelectrode conducted by National Renewable Energy Laboratory (NREL) [119] confirmed that the short-circuit current, I_{sc} of rutile-based DSC is about 30% less than anatase-based at identical film thickness. In addition, the surface area and adsorption spectra of the rutile film also are remarkably less than anatase with about 25% and 35%, respectively [46, 119].

4.2.2.1 Physico-chemical Properties

The morphology and microstructure of the synthesized TiO₂ samples calcined at 400°C, 500°C, 600°C and 700°C at magnification of 100K are shown in Figure 4.19(a)-(d), respectively. All four samples exhibit submicron-sized aggregates with almost same mean aggregates diameter, of about 0.45 μm with deviation of ±0.02 μm.

Despite the increase in calcination temperature, most of the synthesized TiO_2 aggregates still keep their original spherical morphology, indicating the prepared samples having high mechanical strength [112]. This indicates that calcination temperatures have no significant influence on the surface morphology of the prepared samples.

Close inspection showed that there is an increase in the size of nanocrystallites and improved formation of grain boundaries as the calcination temperature increases. In the case of synthesized TiO_2 aggregates calcined at 700°C , the nanocrystallites fused together and formed larger nanocrystallites. In addition, almost no pore present between the nanocrystallites structure as indicated by the arrow in Figure 4.19(d).

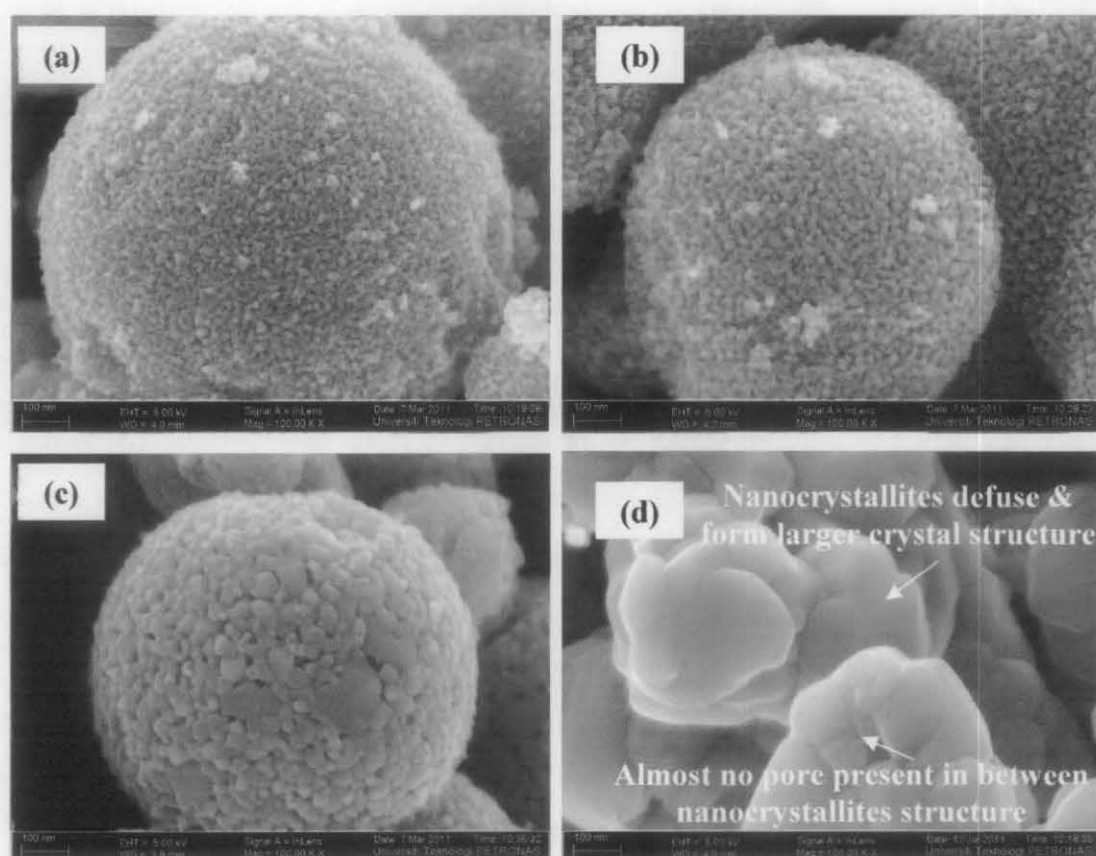


Figure 4.19: SEM image of synthesized TiO_2 aggregates calcined at (a) 400°C (b) 500°C (c) 600°C and (d) 700°C for 2 hours at 100 KX of magnification.

Clear boundaries between particles which appeared at higher calcination temperature is a good indication of the formation of well crystalline TiO_2 samples. However the resolution of SEM images was not sufficient to distinguish between

nano-sized particles and pores. Therefore, XRD analysis was used to estimate the size of nanocrystallite which made up the aggregates [103, 112] while BET method was used to estimate the pore size and specific surface area. Based on the observation of the SEM images obtained, it is proven that the calcination temperature had insignificant effect on the aggregates size, yet promoted the grain growth of the primary nanocrystallites.

XRD was used to investigate the changes of phase structures and crystallite sizes of the calcined samples. Figure 4.20 shows the typical XRD pattern of the synthesized TiO₂ photoelectrode materials subjected to various calcination temperatures. XRD analysis revealed that all samples exhibit peaks corresponding to the formation of crystalline anatase TiO₂ phase with the highest intensity obtained at (*d*₁₀₁) plane for all samples, despite different calcination temperature. This intense sharp peak indicated that the hexagonal crystalline phase of anatase TiO₂ was successfully formed [67]. Nevertheless, when the sample was calcined at 700°C, rutile phase started to form which is clearly shown by the diffraction signal at 27.4°, corresponding to rutile phase with Miller indices (*d*₁₁₀) [92]. Based on the Equation 3.2, the estimated weight percentage of rutile over anatase phase in the sample was about 8%.

In term of peaks width and intensity of diffraction signals, the spectrum shows that as calcination temperature increases, the peak width become narrower and intensity slightly increases, which suggests the increase in crystallinity and particle size. Table 4.7 summarizes the information from the XRD patterns such as phase present, intensity, FWHM, d-spacing and crystallite size at different calcination temperature. As shown by the tabulated data, the crystallites size increases with increasing calcination temperature.

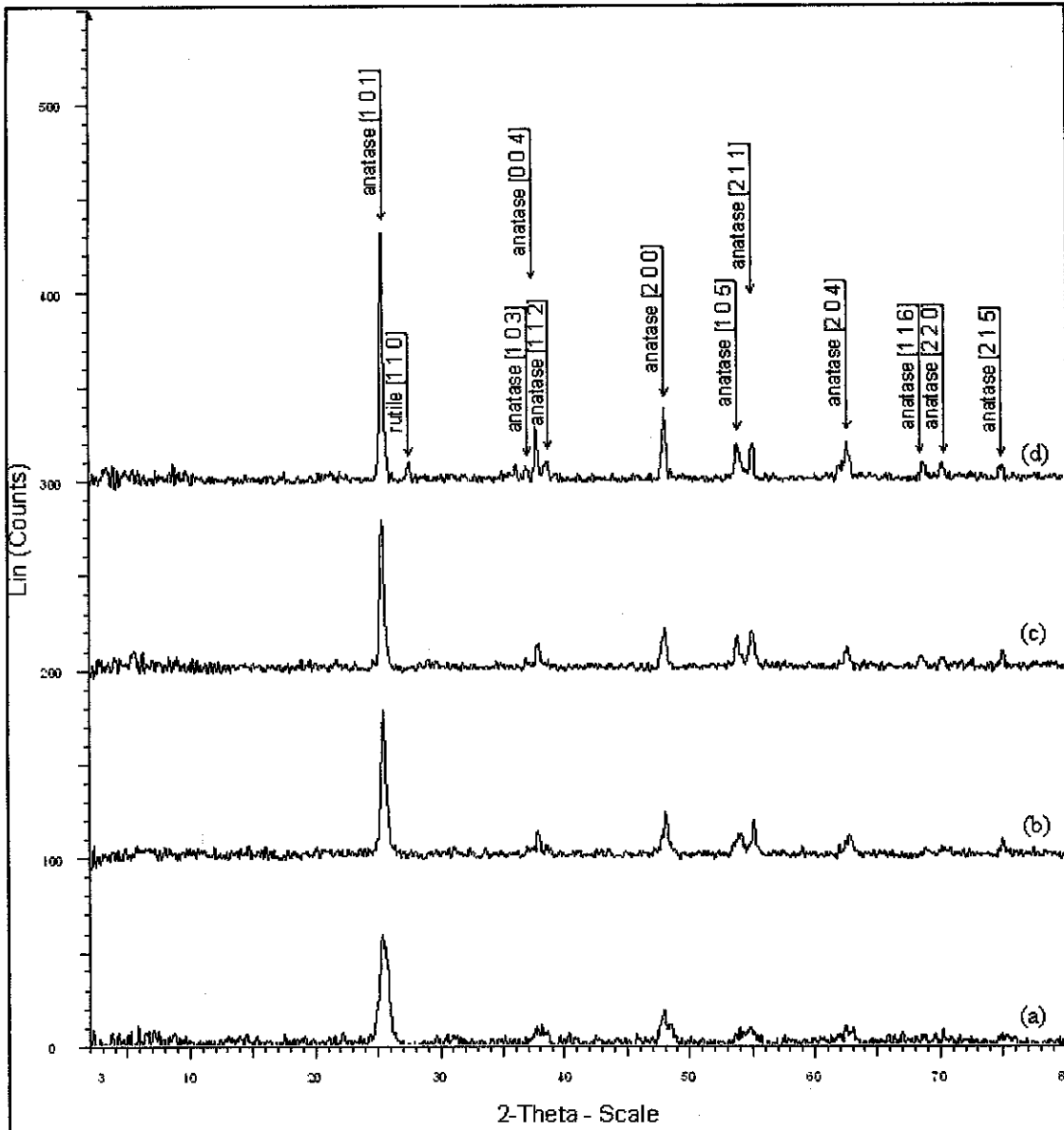


Figure 4.20: XRD pattern of synthesized TiO₂ photoelectrode material subjected to various calcination temperatures (a) 400°C (b) 500°C (c) 600°C and (d) 700°C

Table 4.7: Intensity (counts), FWHM, d-spacing, and crystallite size of anatase at (*d*₁₀₁) plane while at (*d*₁₁₀) plane for rutile TiO₂

Parameter	Calcination Temperature (°C)				
	400	500	600	700	Rutile
Phase Present	Anatase	Anatase	Anatase	Anatase	Rutile
Intensity (counts)	55.4	75.4	91.1	127.0	9.03
FWHM, β	0.688	0.409	0.340	0.305	0.283
d-spacing (Å)	3.510	3.507	3.517	3.514	3.245
Crystallite size (nm)	12.38	20.82	25.03	27.92	30.21

During calcination, the anatase phase could grow through three possible ways; direct aggregation of smaller amorphous titania particle, atom-by-atom recrystallization of smaller anatase particles and solid-state aggregation of adjacent small anatase particles as they adopt appropriate crystallographic orientations [78, 120]. Once anatase is formed through interface nucleation and rapid growth, amorphous titania particles can crystallize onto existing anatase particles by diffusion of atoms, forming bigger anatase particles [77]. This process is also known as ‘Ostwald ripening’. This result showed a good agreement with SEM images obtained earlier, suggesting that the thermal energy caused by the thermal treatment had promoted grain growth causing the crystallites to become larger.

Anatase phase is more thermodynamically stable than rutile phase [77]. This arises from the fact that when the particle size is too small; approximately 14 nm, the molar free energy (J/mol) of rutile becomes higher than that of anatase [77]. This is because rutile has a higher average surface free energy ($\sim 1.9 \text{ J/m}^2$) than anatase ($\sim 1.3 \text{ J/m}^2$) [77]. As a consequence, more thermal energy is needed to break and rearrange bonds to nucleate rutile at nanoparticle surfaces [121]. Thus, at lower calcination temperature, the interface nucleation and growth of anatase nuclei predominates, yet at higher calcination temperature ($>600^\circ\text{C}$), surface nucleation of rutile become dominant.

Nitrogen sorption isotherm and corresponding pore size distribution of all synthesized samples calcined at four different temperatures were compared in Figure 4.21 and Figure 4.22. Characteristic properties such as specific surface area, pore volume and average pore size were determined using BET and BJH method and tabulated in Table 4.8 [108, 109]. Figure 4.21 shows that samples calcined at temperature 400°C to 600°C demonstrate types IV of nitrogen sorption isotherms pattern volume at a high relative pressure, P/P_0 of 0.6-0.9 which represents mesoporous structure [111-115]. However, at 700°C of calcination temperature, a more complicated pore structure present as indicated in the nitrogen sorption isotherm plot (Figure 4.14) where it exhibits linear region at high relative pressure; a type I hysteresis loop [115]. This indicates that sample calcined at 700°C has microporous structures. The outcome is agreeable with the SEM images obtained earlier.

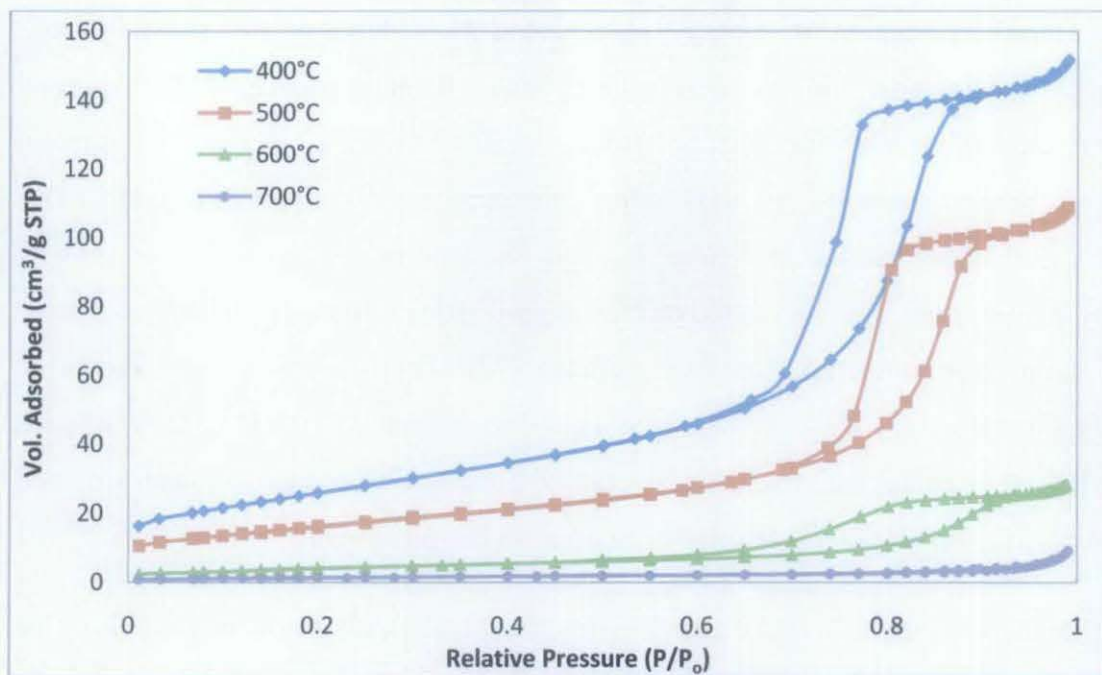


Figure 4.21: Nitrogen sorption isotherm of synthesized TiO_2 aggregate at different calcination temperature.

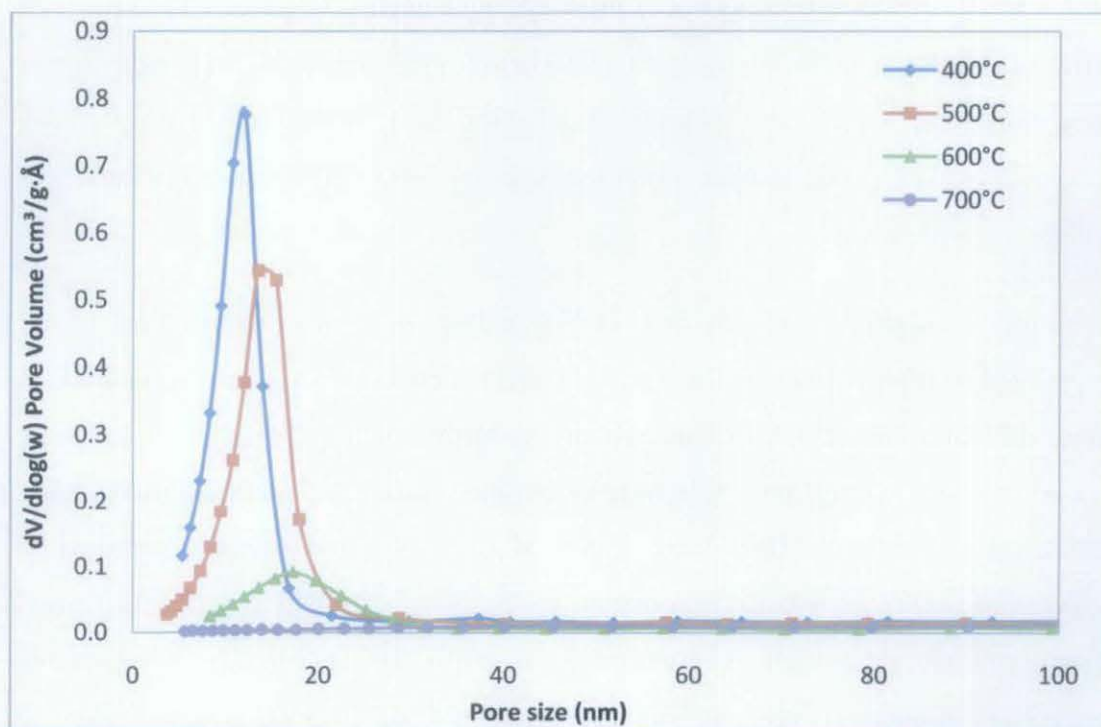


Figure 4.22: Pore size distribution of synthesized TiO_2 aggregate at different calcination temperature.

Table 4.8: Surface area, pore volume and pore size of the synthesized TiO₂ as a function of calcination temperature.

Calcination Temperature (°C)	S _{BET} (m ² g ⁻¹)	Pore Volume (cm ³ g ⁻¹)	Pore Size (nm)
400	94.25	0.24	8.3
500	59.28	0.17	9.9
600	15.34	0.04	10.0
700	5.34	0.01	11.2

Moreover, with increasing calcination temperatures, the positions of the hysteresis loops gradually decrease suggesting the decrease in the specific surface areas. At 400°C, the sample exhibits the largest surface area of 94.25 m²g⁻¹. The available specific surface area of the sample further reduce to 59.28 m²g⁻¹, 15.34 m²g⁻¹ and 5.34 m²g⁻¹ as the calcination increases to 500°C, 600°C and 700°C. Besides, the average pore volume of the synthesized samples also decreases as the calcination temperature increases. This result is in good agreement with SEM images with crystallite size determined by XRD analysis where it is believed that the calcination temperature had forced nanocrystallites to fuse together and form a larger crystal structure, thus reducing the surface to volume ratio and average pore volume of the synthesized samples.

Based on the Figure 4.22, with increasing of the calcination temperature from 400°C to 700°C, the maximum pore size slightly shifted towards larger mesopores regions, indicating the growth of pores as summarized in Table 4.8. This is due to the enhancement of crystallization of TiO₂ samples and the growth of the anatase crystallites [111] as evidence in Figure 4.19. On the other hand, there are no significant different in the pore volume of the inter-aggregated pore region (>50 nm) of each calcined samples as shown in Figure 4.22. This phenomenon proves that the samples have high mechanical strength and keep their original spherical aggregation morphology regardless of calcination temperature.

4.2.2.2 Performance Verifications

The performances of the integrated DSCs were verified by measuring the *I-V* behavior when the cells were irradiated under AM-1.5 radiation and 100 mW/cm² of illumination. Table 4.9 summarizes the open circuit voltage (V_{oc}), the short circuit

current (I_{sc}), the fill factor and the overall performance efficiency of all assembled DSCs integrated with synthesized TiO_2 aggregates as obtained from the $I-V$ analysis.

DSC integrated with photoelectrode made up of TiO_2 aggregates and calcined at $400^\circ C$ has recorded I_{sc} of 9.487 mA.cm^{-2} and efficiency of 3.734%. When the calcination temperature is increased from $500^\circ C$ to $600^\circ C$ and $700^\circ C$, the I_{sc} registered the value of 9.685 mA.cm^{-2} , 5.86 mA.cm^{-2} and 1.195 mA.cm^{-2} , respectively. The same trend was also observed in the efficiency of the integrated DSCs where DSC made of TiO_2 aggregates calcined at $500^\circ C$ shows an efficiency of 3.867%, while calcined at $600^\circ C$ and $700^\circ C$ exhibit efficiency of 2.422% and 0.495%, respectively. Unlike I_{sc} , V_{oc} and fill factor, FF values recorded are in a small range of 0.66 V to 0.72 V and 0.50 to 0.52, respectively with no obvious decreasing or increasing trend.

Table 4.9: Photovoltaic properties of the synthesized TiO_2 aggregates as a function of calcination temperature.

Calcination Temperature ($^\circ C$)	V_{oc} (V)	I_{sc} (mA.cm^{-2})	Fill Factor (FF)	Efficiency (%)
400	0.668	9.487	0.518	3.734
500	0.677	9.685	0.519	3.867
600	0.724	5.860	0.502	2.422
700	0.721	1.195	0.505	0.495

Figure 4.23 and Figure 4.24 illustrate the behavior of the I_{sc} and efficiency as a function of calcination temperature, respectively. Both graph demonstrate the same behavior where the value increasing as the calcination temperature increases from $400^\circ C$ to an optimum temperature and then drop down with further increase in the calcination temperature. The same trend in the overall efficiency of the cells is expected since it is partly dependent on the I_{sc} . Extrapolating in the graph indicate that $450^\circ C$ is the optimum calcination temperature for the TiO_2 aggregates photoelectrode material of DSCs.

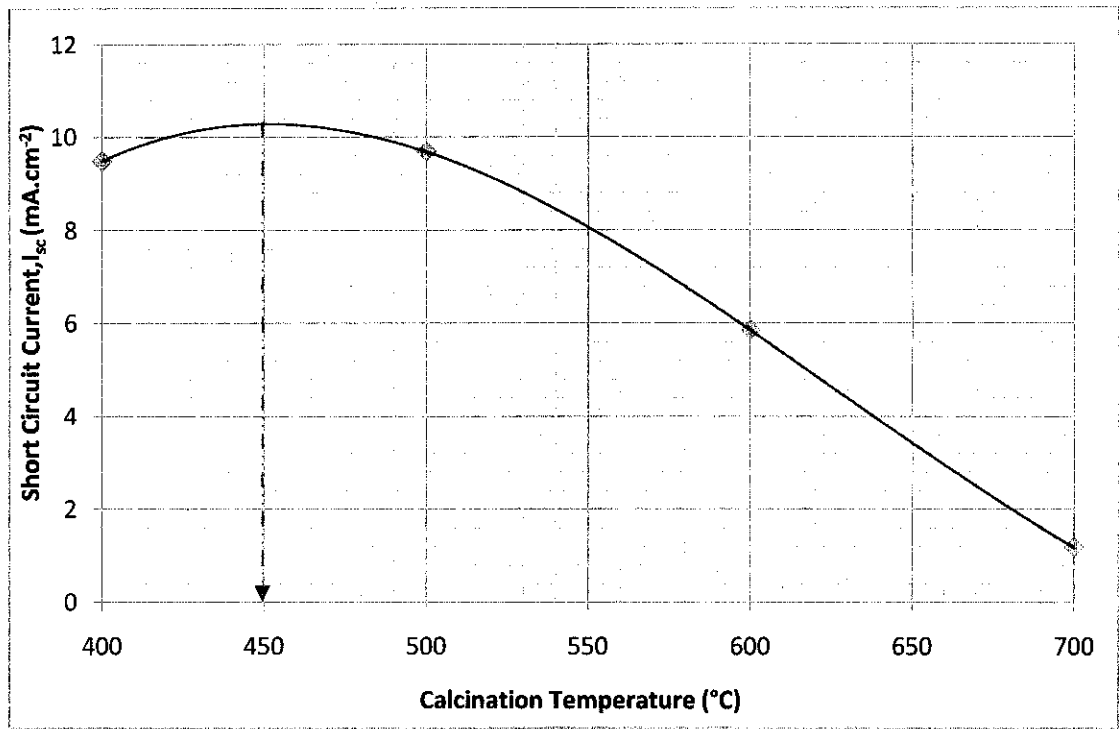


Figure 4.23: Dependence of short circuit current on calcination temperature

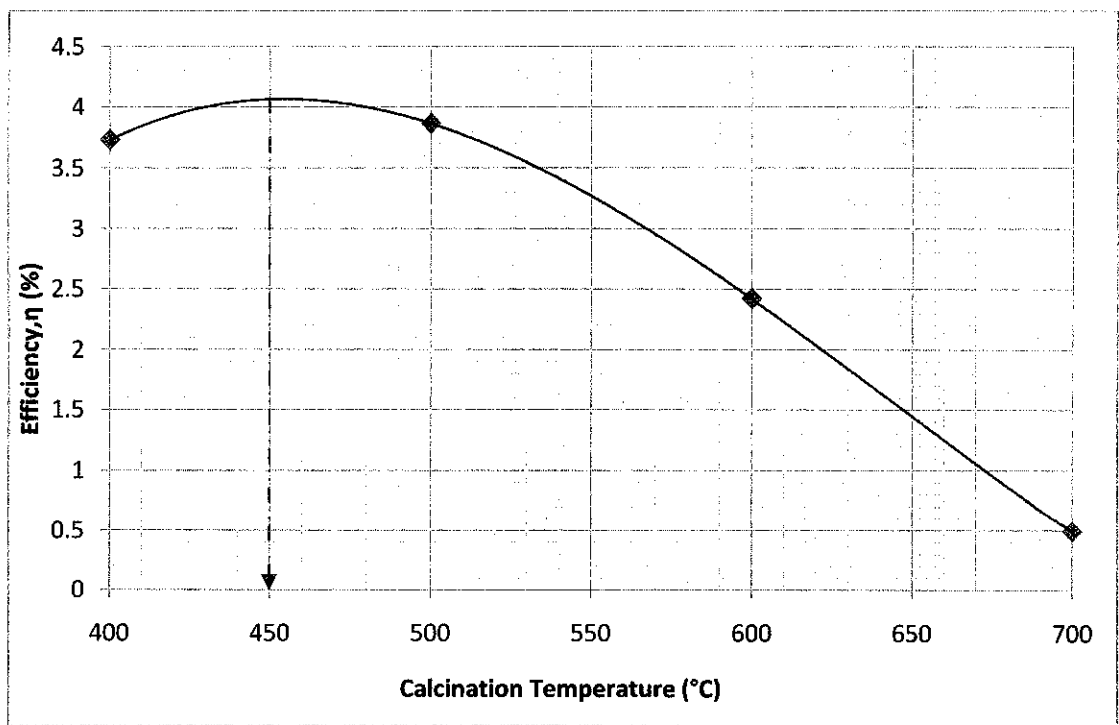


Figure 4.24: Dependence of performance efficiency of DSC on calcination temperature

According to Zhang et al. [28], there are three factors that could affect the I_{sc} of a DSC; the initial number of photogenerated carriers, the injection efficiency of electrons from dye molecules to semiconductor and the recombination rate between the injected electrons and oxidized dye or redox species in the electrolyte. In this study, it is reasonable to assume that there is no significant difference in the injection efficiency and recombination rate of each prepared TiO₂/N719/electrolyte cells. Hence, the initial number of photogenerated carriers may be significantly affected by the capability of the respective cells to harvest light radiance, which is closely related to the specific surface area of the photoelectrode film. Higher surface area would result in higher dye absorption.

Based on the result of the surface area from BET, increasing the calcination temperature would result in decreasing the surface area of the synthesized TiO₂ photoelectrode material. Sample calcined at 400°C has the biggest surface area, thus is expected to be occupied with a large amount of dye. In order to prove the theory, the difference in the dye absorption of each respective calcined samples were further explored by a dye-desorption experiment. In this test, ammonium solutions were used to desorb dye from the TiO₂ films. The solutions were then characterized by using UV-Vis spectroscopy. High optical absorption indicate the presence of large amount of dye in the solution. Optical absorption spectra of the desorbed-dye solution are shown in Figure 4.25.

The result clearly shows that all of the desorbed-dye solutions present three absorption peaks (310 nm, 372 nm, 509 nm) in the range of 200 nm to 900 nm, corresponding to the characteristic of N719 dye absorption. The desorbed-dye solution of sample calcined at 600°C and 700°C show no significant difference in the optical absorption intensity which indicate same amount of dye loading. However, the I_{sc} and performance efficiency of cells build up with samples calcined at 700°C shows a much lower I_{sc} and performance efficiency. This is attributed to the presence of rutile phase of the samples calcined at 700°C. It is reported [46] that at the same value of short-circuit current density, the effective diffusion coefficient, D_n of rutile phase is one order of magnitude lower than that of anatase phase, implying that electron transport is slower in the rutile phase than in the anatase phase.

The sample calcined at 400°C exhibit the highest absorption intensity, indicating the highest amount of dye being absorbed due to the presence of large surface area as shown by BET analysis obtained earlier. Calcination at 500°C has force the formation of larger nanocrystallite as calculated by Scherer formula, thus reducing the surface area for dye chemisorption. Nevertheless, DSCs integrated with samples calcined at 500°C shows higher I_{sc} and performance efficiency compared to the one calcined at 400°C. It is a well known fact that specific surface area and crystallinity are two conflicting factors influencing the performance efficiency of TiO_2 -based DSCs. The TiO_2 photoelectrode material with a large surface area are usually associated with a large amount of crystalline defects or weak crystallization, which favor the recombination of photo-generated electrons, causing a low performance efficiency [111]. Therefore, a large surface area is a requirement, but not a decisive factor [112].

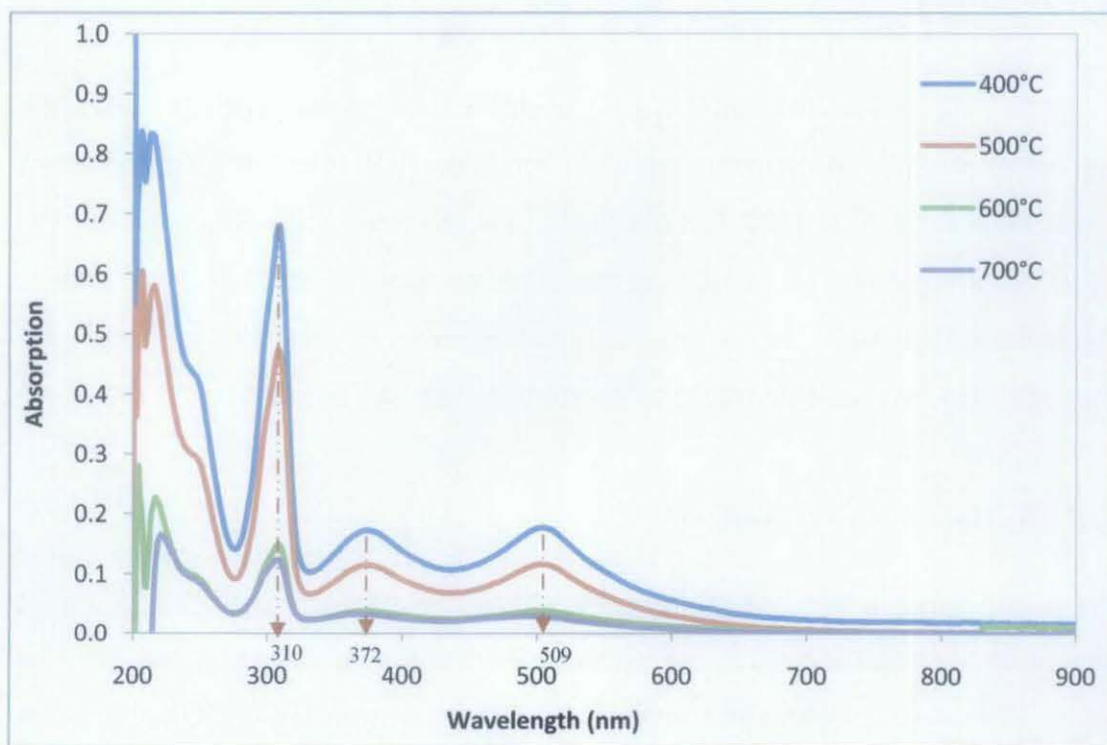


Figure 4.25: Absorption spectra of the desorbed-dye from the TiO_2 photoelectrode material at different calcination temperature.

4.3 TiO₂ Aggregates/Nanoparticles Composite Based DSC

In most conventional DSCs, the photoelectrode material are made up of TiO₂ nanoparticles with sizes of about 15-20 nm which is much smaller than the wavelength of visible light. This made the films transparent with little light scattering. Incorporation of large nanoparticles (>100 nm) has been employed as light-scattering centers to increase the optical length in the film, where enhanced light-harvesting has been demonstrated both experimentally and theoretically [35]. As discovered in the previous section, the photoelectrode material made up of TiO₂ aggregates can scatter light and thus enhance the light harvesting efficiency. Therefore, the aggregates/nanoparticles composites can represent a very versatile structure. The submicron-sized aggregates can enhance the light harvesting while the incorporated nanoparticles can reduce the void and improve the connectivity within the composite film.

In this subsection, the composite of synthesized TiO₂ nanoparticles and TiO₂ aggregates prepared at optimum synthesis condition (0.9 vol% of water in ethanol solution and calcined at 450°C) as obtained in the previous section (section 4.2.1 and 4.2.2) were used as photoelectrode to fabricate DSCs. The effect of relative aggregates/nanoparticles ratio on the performance of integrated DSCs was investigated systematically using UV-Vis spectroscopy and IV-curve.

4.3.1 Performance Verification

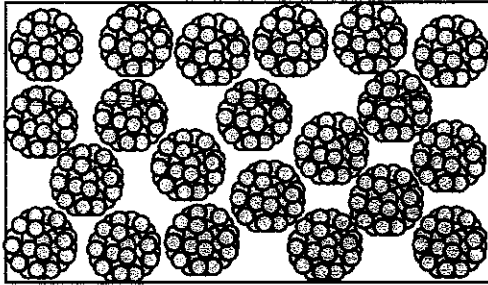
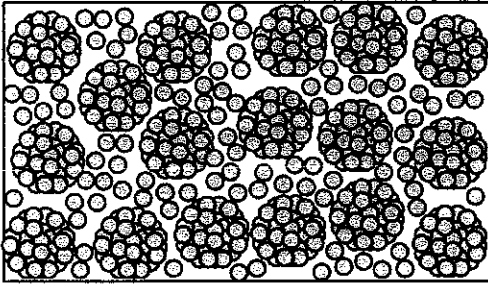
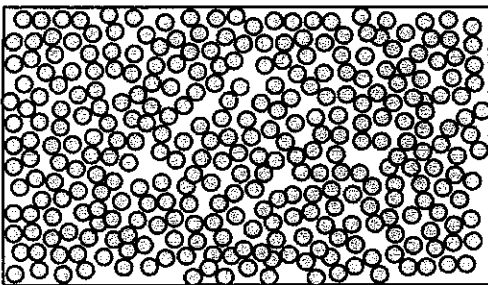
The performance of the DSCs integrated with nanoparticle/aggregate composite as photoelectrode material were measured under illumination of simulated AM 1.5 solar lights. Table 4.10 compares photovoltaic properties of synthesized TiO₂ aggregates, composite and nanoparticles based DSC. Based on the tabulated data, all parameter except open circuit voltage, V_{oc} show increasing and/or decreasing trend with increasing percentage of nanoparticles incorporated in the photoelectrode TiO₂ aggregates films. As expected, open circuit voltage, V_{oc} exhibit almost the same value of 0.72 ± 0.03 V for all samples, considering that the open-circuit voltage was

generally determined by the difference between the Fermi level of the oxide semiconductor and the redox potential of the electrolyte [39].

Fill factor, FF reflect the packing of the TiO_2 photoelectrode structure of each individual integrated solar cell and the transport mechanism of carriers through the DSC. Higher fill factor, FF value attributed to better photoelectrode structure packing and lesser charge recombination at the TiO_2 /redox electrolyte interface [39]. Based on Table 4.10, it is clear that increasing the percentage of nanoparticles present in the photoelectrode films result in improved fill factor, FF which indicates better photoelectrode packing (as illustrated in Table 4.10) thus improve the connectivity between photoelectrode TiO_2 for better electron transport.

The short-circuit current, I_{SC} is another parameter affected by the configuration of photoelectrode structure and directly result in the variation of performance efficiency of integrated DSCs. The short-circuit current density, I_{sc} and performance efficiency plotted versus percentage of nanoparticles in the integrated photoelectrode films are displayed in Figure 4.27 and Figure 4.28, respectively. Based on Figure 4.26 and Figure 4.27, highest performance efficiency can be obtained by incorporating 20% of nanoparticles in photoelectrode film which exhibits I_{sc} of $9.444 \text{ mA}\cdot\text{cm}^{-2}$ with over 4% of performance efficiency.

Table 4.10: Comparison of photovoltaic properties of aggregates, composite and nanoparticles based DSC.

Integrated DSC	V_{oc} (V)	I_{sc} (mA.cm ⁻²)	Fill Factor (FF)	Efficiency, η (%)	Illustration	
Purely Aggregates (0% Nanoparticles)	0.710	9.444	0.514	3.916		
Composite	20% Nanoparticles	0.691	9.557	0.539	4.040	
	40% Nanoparticles	0.737	8.077	0.567	3.839	
	60% Nanoparticles	0.734	7.741	0.579	3.736	
	80% Nanoparticles	0.743	7.537	0.584	3.715	
Purely Nanoparticles (100% Nanoparticles)	0.720	7.358	0.589	3.545		

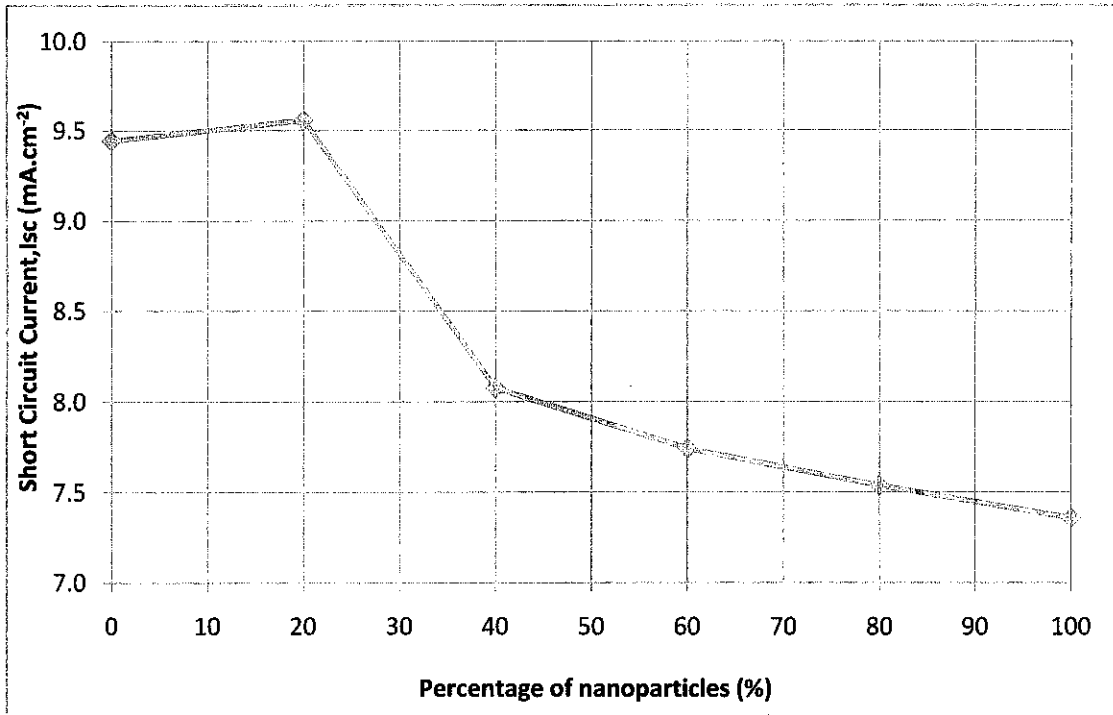


Figure 4.26: Dependence of short-circuit current on percentage of nanoparticles in photoelectrode films

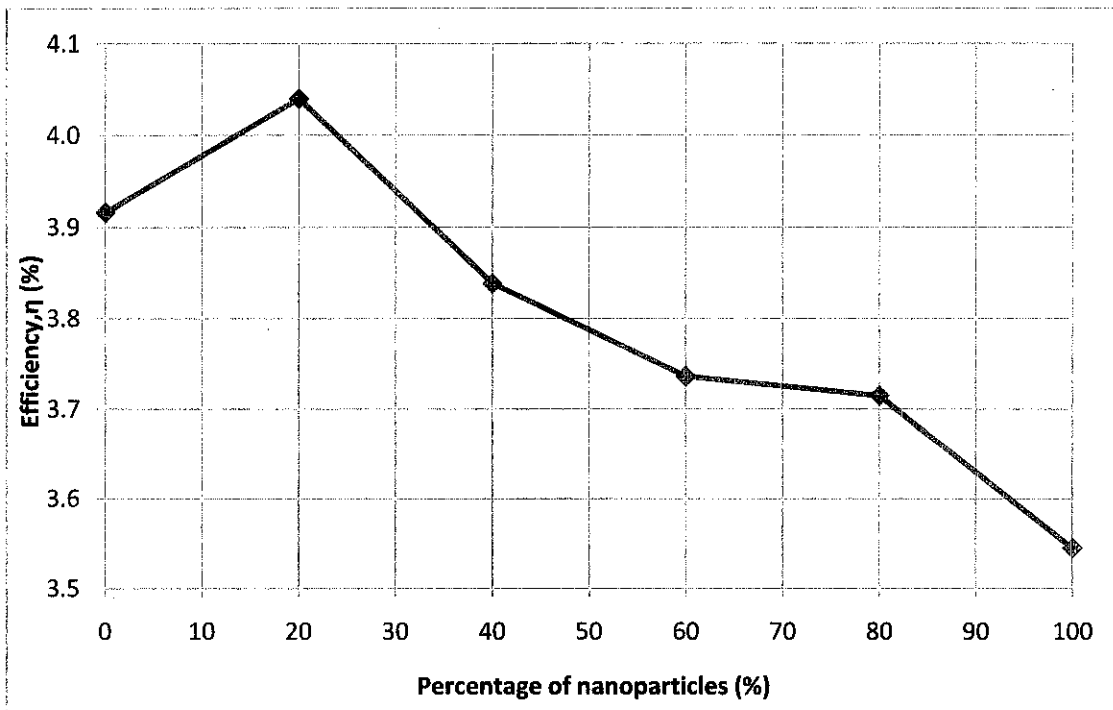


Figure 4.27: Dependence of performance efficiency of integrated DSCs on percentage of nanoparticles in photoelectrode films

The I_{sc} and performance efficiency of the DSCs displayed similar trend with an increase of percentage of incorporated nanoparticles where they slightly increase with amount of nanoparticles present, then decline when the percentage of nanoparticles in the films is beyond 20%. There are two possible reasons to support the finding; the capability of the films to anchor dye molecules and the light scattering effect of the composite photoelectrode film.

In order to study the amount of dye loading on the prepared TiO_2 films, optical absorption of the desorbed dye were tested using UV-Vis spectrum in the range of 900 nm to 200 nm. The absorption spectra of desorbed dye are shown in Figure 4.28. Based on the results, it is clear that all samples exhibit peaks at about 310 nm, 390 nm and 530 nm, corresponding to the ligand-centered charge transfer (LCCT) transitions ($\pi - \pi^*$) as well as metal-to-ligand charge transfer (MLCT) transitions ($4d-\pi^*$) that can be observed in the typical UV/Vis spectra of N-719 dye [104]. Nevertheless, there are obvious different in intensity of the respective samples which implies the variation in the amount of dye absorbed by the prepared TiO_2 films. Increase the percentage of nanoparticles in the films results in increasing the intensity of the absorption spectrum with the highest absorption intensity in the range of 900 nm to 200 nm obtained by desorbed dye solution of purely nanoparticles (100% nanoparticles) films. This indicates that films made up of 100% nanoparticles TiO_2 exhibit the largest surface area and better porosity, thus could anchor large amount of dye. In contrast, films made up with purely TiO_2 aggregates (0% nanoparticles) structure show the lowest absorption intensity which signifies the lowest amount of dye being anchored by the films. This phenomenon was due to the configuration of aggregates itself which limit the accessibility of dye to be anchored by each and every single nanocrystallite that made up the aggregates.

Even though the films integrated with 100% nanoparticles structure have the ability to anchor the largest amount of dye, their performance efficiency is the lowest among others when they are being integrated as DSC. This could be due to the absence of scattering effect in the films. Hence, in order to examine the light scattering effect of the TiO_2 films, the UV-Vis absorption of sensitized TiO_2 composite films were employed [39] with FTO glass as baseline and the result is

shown in Figure 4.29.

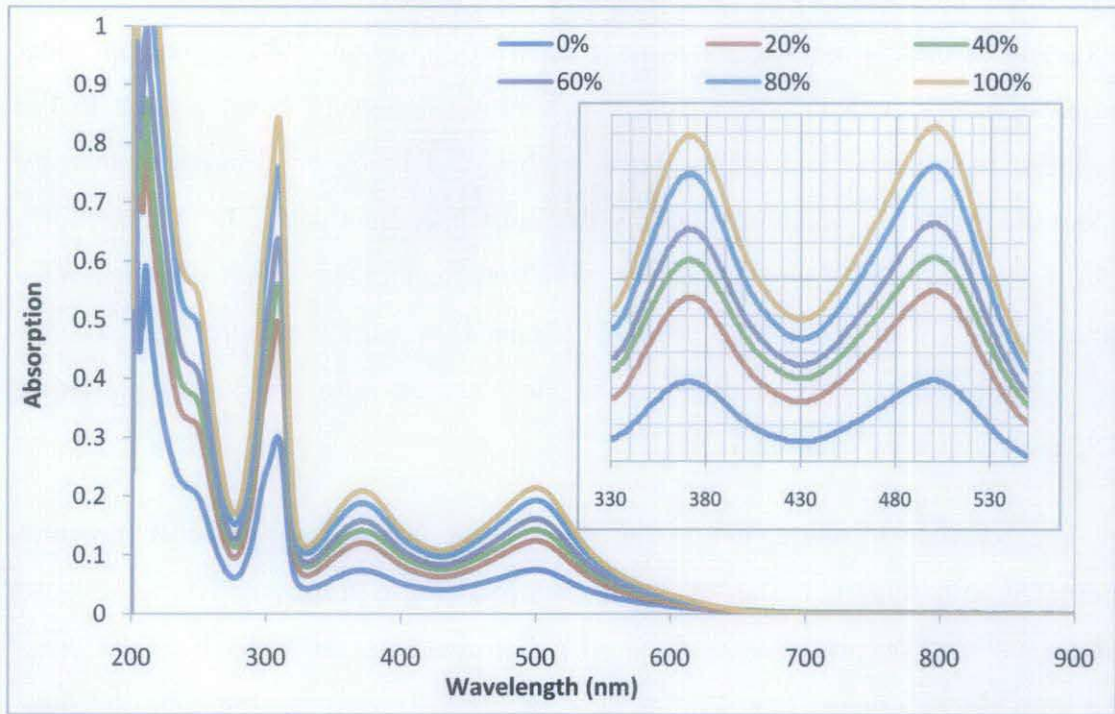


Figure 4.28: UV-Vis spectra of desorbed dye at different percentage of nanoparticles

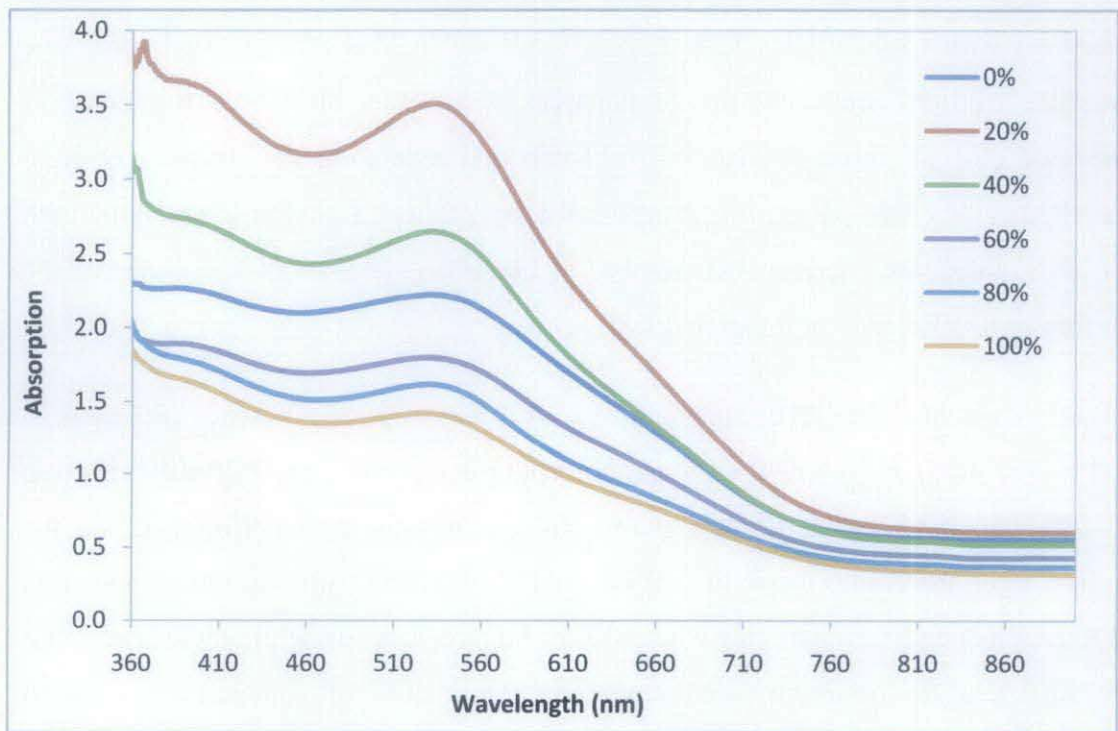


Figure 4.29: Nominal optical spectra of dyed TiO₂ aggregates films mixed with different percentage of nanoparticles

The nominal optical absorption spectra (Figure 4.29) indicate the difference in light-absorption capability of each integrated TiO₂ photoelectrode material. Based on the graph of optical spectra, films made up with more than 50% aggregates show strong optical spectra which suggest that a strong scattering effect present in the photoelectrode films. The graph shows a clear difference of absorption intensity where the highest intensity obtained by the films integrated with 20% nanoparticles film, followed with 40% nanoparticles, purely aggregates, 60% nanoparticles, 80% nanoparticles while the lowest intensity obtained by purely nanoparticles (100% nanoparticles) film. This proves that the nanoparticles film has lowest scattering efficiency compared with other films.

The presence of aggregates in the films likely to lead to a disorder structure compared with films made up of purely nanoparticles as illustrated in Figure 4.30. Previous study [39] proved that a less-ordered structure exhibit better light scattering and form closed loops of light confinement. Figure 4.30 compares the light travelling in aggregates and nanoparticles films. The films made up with aggregates structure have higher tendency of light scattering and formation of closed loop whist films made up with nanoparticles have higher tendency to loss the light radiance. The presence of light scattering in the photoelectrode films influences the transport behavior of light through changing the path and extending the distance of light travelled. This could results in increasing the possibility of photon interactions with the dye molecules, increase the number of electrons generation thus improve the performance efficiency of integrated DSC.

Based on the Table 4.10, the graph of I_{sc} and performance efficiency (Figure 4.26 and Figure 4.27) as well as the optical absorption spectra (Figure 4.29), the addition of 20% nanoparticles in the aggregates film exhibits the best performace and the highest light absorption capability. This could be the result of optimum composition of aggregates and nanoparticles where 80% of aggregates in the photoelectrode film are sufficient for optimum scattering effect while 20% of nanoparticles help in reducing the voids, increasing the surface area for dye chemisorption and improving the connectivity between the composite films for better electrons transportation.

Incorporating nanoparticles in aggregates films also could improve the packing of

the films and at same time provide bigger specific surface area for dye chemisorptions. Increasing the amount of dye absorbed would enhance the probability of photon being captured; results in higher electron generation while improvement in films packing would reduce the possibilities of recombination of generated electrons thus improve the performance of integrated DSCs. However, large specific surface area is a requirement but not a decisive factor. The scattering effect is another factor that need be taken into consideration in preparing high performance photoelectrode films of a DSC. Hence, based on the finding, it is critical to optimize the composition of aggregates/nanoparticles composite in order to optimize the light scattering effect and at the same time providing better connectivity and large surface area for anchoring the sensitized dye molecules, thus improve the performance of the integrated DSCs.

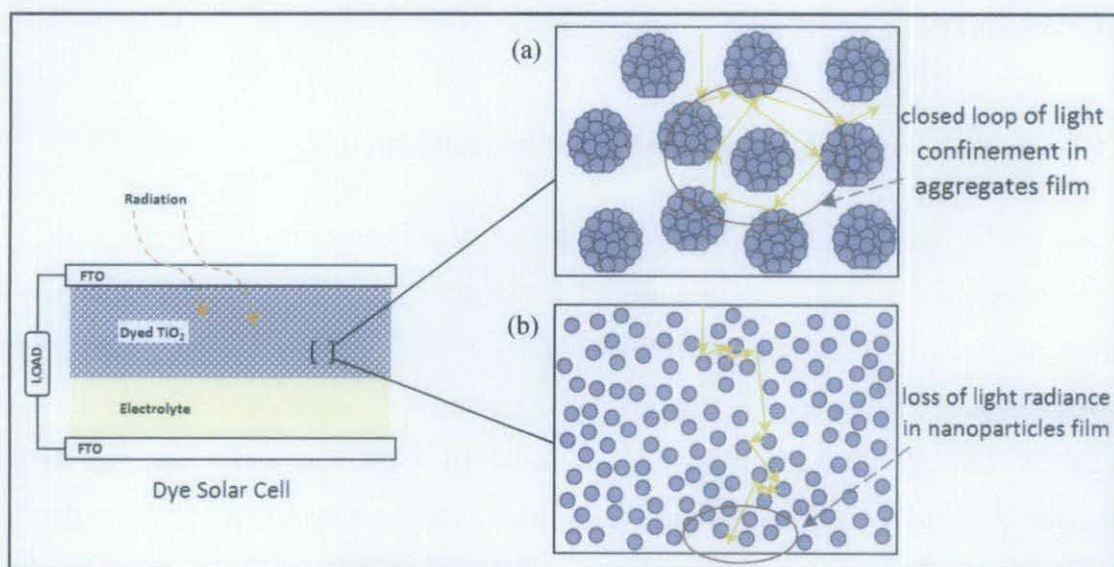


Figure 4.30: Illustration of light travelling in photoelectrode TiO₂ films of (a) aggregates and (b) nanoparticles structure

CHAPTER 5

CONCLUSION

This chapter starts with the summary of the outcome of the each part of the research work, followed by conclusion, benefit and recommendation for future work. The outcome of research work in the form of patent filed, awards, publication and conference/exhibition/seminar are listed in Appendix B.

5.1 Summary

5.1.1 Synthesis of TiO₂ Nanoparticles for Dye Solar Cell

Based on the result obtained from the first part of this research work, synthesized TiO₂ nanoparticles with crystallite size of 17.55 nm recorded the highest efficiency compared with two commercially available TiO₂; P-25 (Degussa) and TiO₂-MERCK. XRD characterization reveals that both synthesized TiO₂ nanoparticles and TiO₂-MERCK were in the form of anatase phase whilst, P-25 was in the form of well crystalline mixed anatase and 20% rutile. However, the particle size of TiO₂-MERCK is more than two times bigger than synthesized TiO₂ nanoparticles.

I-V characterization proved that synthesized TiO₂ nanoparticles-based DSC demonstrated the best performance with I_{sc} of 7.358 mA/cm² and η of 3.545% at identical film thickness of ~12 μ m whilst P-25 and TiO₂-MERCK based DSC recorded an efficiency of 3.421% and 1.073%. Although the synthesized TiO₂ nanoparticles and P-25 samples have about same particles size, the presence of rutile phase has limited the efficiency of P-25 based DSC. In contrast, the low efficiency of DSC printed with TiO₂-MERCK as photoelectrode is due to the large particles size, resulting in smaller surface area and contact point for dye chemisorptions which would then decrease the potential of electron generation.

5.1.2 Development of TiO₂ Aggregates Photoelectrode Material in Dye Solar Cell

TiO₂ aggregates samples were successfully synthesized through hydrolysis reaction of diluted titanium alkoxide solution with alcohol-water solution. Two parameters studied are percentage of water content in ethanol solution and calcination temperature. Through the study on the effect of water content on the physico-chemical properties of synthesized TiO₂ aggregates, it is clear that there is a correlation between the amount of water content and the size of aggregates. Increase the percentage of water content from 0.9-3.6 vol% results in decreasing the aggregates size from 0.39 μm to 0.20 μm with qualitative deterioration in aggregates structure. In addition, BET analysis confirmed that the surface area of the synthesized samples decrease from 75.56 m²g⁻¹ to 62.75 m²g⁻¹, 54.23 m²g⁻¹ and 49.14 m²g⁻¹ as the percentage of water content in ethanol solution increase from 0.9 vol% to 1.8 vol%, 2.7 vol% and 3.6 vol%, respectively. However, the average pore size of the aggregates is directly proportional to the percentage of water content; increasing from 10.9 nm to 17.1 nm as the percentage of water content increases from 0.9 vol% to 3.6 vol%.

The short-circuit current, I_{sc} and efficiency, η show the same trend were I_{sc} decrease from 9.679 mA.cm⁻² to 7.05 mA.cm⁻² while the η decrease from 3.915% to 3.504% as the percentage of water content increase from 0.9-3.6 vol%, the. This is clear that the performance of the integrated DSCs has a strong relationship with I_{sc} which measures the capability of TiO₂ photoelectrode films to anchor dye molecules and harvest light radiance efficiently. BET analysis reveals that specific surface area of the photoelectrode films is decreasing as the percentage of water content increases, which causes the reduction in the amount of dye absorbed. This is proven by the optical absorption characterization of desorbed dye of each cell. The highest light absorption intensity is obtained for the desorbed dye solution of TiO₂ films synthesized with 0.9 vol% of water in ethanol solution. The absorption intensity decreases with increasing amount of water content indicating the decrease in the amount of dye absorbed by TiO₂ films.

The efficiency of light harvesting is another factor that influences the performance

of integrated DSCs. The presence of large aggregates in the sample synthesized with low amount of water content (0.9 vol%) has induce more light scattering, thus extending the traveling distance of light within the photoelectrode films and increasing the opportunities for incident photons to be captured by the dye molecules. The photocurrent action spectra analysis show that sample synthesized with 0.9 vol% of water content exhibit broader feature compared to other samples indicating the occurrence of better light scattering in the photoelectrode films. The result signifies that aggregate size and degree of aggregation would induce better light scattering in the visible region and influences the transport behavior through changing the light path and extending the distance of travel in the film which in turn increases the chances of interaction between photons and the dye molecules. Based on this study, it can be concluded that, 0.9 vol% of water content in ethanol solution is the optimum percentage of water content for synthesizing TiO₂ aggregates for the best performance of DSC.

In the study of the effect of calcination temperature, all samples calcined at 400°C, 500°C, 600°C and 700°C exhibit submicron-sized aggregates with almost the same mean aggregates diameter, about 0.45 μm with deviation of ±0.02 μm. However, it is observed that there is an increase in the size of nanocrystallites and formation of well crystalline anatase TiO₂ samples as the calcination temperature increases from 400°C to 700°C. In addition, calcining the sample at 700°C has promoted the formation of rutile phase to about 8%. BET analysis also reveals that the surface area decrease from 94.25 m²g⁻¹ to 59.28 m²g⁻¹, 15.34 m²g⁻¹ and 5.34 m²g⁻¹ as the calcination increased from 400°C to 500°C, 600°C and 700°C, respectively. Besides, the average pore volume of the synthesized samples also decreases as the calcination temperature increases.

The short circuit current, I_{sc} of 9.487 mA.cm⁻² and performance efficiency, η of 3.734% of the sample calcined at 400°C to the highest value when subjected to optimum calcination temperature of 450°C. Further increase in calcination temperature results in decreasing the performance of DSCs. Sample calcined at 500°C, 600°C and 700°C exhibit the I_{sc} of 9.685487 mA.cm⁻², 5.86487 mA.cm⁻² and 1.195487 mA.cm⁻² and efficiency of 3.867%, 2.422% and 0.495%, respectively.

Sample calcined at low temperature exhibit larger surface area, thus can be accommodate large amount of dye molecules. However, low calcination temperature usually associated with a large amount of crystalline defects or weak crystallization. Broad band gap energy of sample calcined at low temperature (400°C) is another factor that limit their performance efficiency. This would favor the recombination of photo-generated electrons, causing a low performance efficiency of DSC. On the other hand, increasing the calcination temperature would force the formations of larger nanocrystallite, thus reducing specific surface area for dye chemisorptions. The presence of rutile phase would also decrease the effective diffusion coefficient to a magnitude lower compared to the purely anatase phase of TiO₂ films. Therefore, a large surface area of TiO₂ nanoparticles is a requirement, but not a decisive factor. Based on the study, the optimum calcination temperature obtained is 450°C with the overall highest conversion efficiency of 3.916%.

5.1.3 TiO₂ Aggregates/Nanoparticles Composite Based Dye Solar Cell

Photoelectrode composite films were prepared by incorporating nanoparticles into the aggregates samples synthesized with 0.9 vol% of water in ethanol solution and calcined at an optimum temperature of 450°C. I-V characterization tested under simulated AM 1.5 solar lights shows that the short-circuit current, I_{sc} and efficiency, η increases with the amount of incorporated nanoparticles reaching the highest value when the amount is 20%. Beyond 20% of nanoparticles, I_{sc} and η reduce significantly. Higher than 4% performance efficiency of DSC can be achieved by incorporating 20% of nanoparticles in photoelectrode films which exhibits highest I_{sc} value of 9.444 mA.cm⁻².

TiO₂ photoelectrode film made up of purely nanoparticles has an advantage in absorbing large amount of sensitized dye. However, low scattering effect has restrained the performance of DSC. In contrast, photoelectrode TiO₂ of pure aggregates which compose of nanocrystallite could introduce light scattering effect. However, aggregates with submicron size introduced large voids that cause poor connection within the atomic structure of the film. This affects the performance of aggregates based-DSC. Hence, integrating aggregates/nanoparticles composite could

overcome the weaknesses of purely nanoparticles and aggregates based-DSC.

Based on the finding, it is critical to optimize the composition of aggregates/nanoparticles composite in order to optimize the light scattering effect, improve connectivity and at the same time providing large surface area for anchoring the sensitized dye. Increasing the amount of dye absorbed would enhance the probability of photon being captured, resulting in higher electron generation, while improving the connectivity for transporting the generated electrons which contribute to an increase in the performance of DSC. Based on the study, the highest performance efficiency of DSC can be achieved by integrating 20% of nanoparticles in aggregates films which exhibit I_{sc} of 9.444 mA.cm^{-2} with over 4% of performance efficiency.

5.2 Conclusion

In conclusion, the objective of this research is achieved. TiO_2 photoelectrode material (aggregates/nanoparticles composite) with desired characteristic such as large surface area, better light scattering and improve connectivity has been successfully synthesized. Highest performance efficiency of solar cell is achieved by incorporating 20% nanoparticles in aggregates films composite wherein, nanoparticles are having an average size of $\sim 20 \text{ nm}$ and aggregates having micron size ranging $0.4\text{-}0.6 \mu\text{m}$ which are made up of $10\text{-}20 \text{ nm}$ nanocrystallites. Incorporating 20% nanoparticles have reduce the voids in the photoelectrode films, improve surface area for dye chemisorption and provide better connectivity for faster electron transport. The 80% aggregates that made up the films can provide efficient light scattering thus extending the travel distance of light radiance and at the same time increasing the possibility of photon being captured causing more electrons to be excited. These phenomena results in increasing the short circuit current and performance efficiency of the integrated solar cells.

Overall conversion efficiency of over 4% has been achieved by DSCs integrated with photoelectrode TiO_2 composite (20% nanoparticles and 80% aggregates) which is about 18% and over 270% improvement compared to P-25 and $\text{TiO}_2\text{-MERCK}$ based

DSCs, respectively.

4% efficiency achieved in this study is less than half of highest conversion efficiency of 11.1% (active area = 0.219 cm², I_{sc} = 4.57 mA, V_{oc} = 0.736 V) recorded by Chiba et. al. [26]. In different with this study, they used hazed TiO₂ photoelectrode material sensitized by black dye with tin coated-oxide (TCO) as substrates. It is known that TCO substrate has lower resistance compared to the FTO substrate used in this study. In addition, black dye used in their research study also has higher absorption in the red region compared with N719 dye. Chiba and co-workers also added deoxycholic acid in the dye solution at concentration of 20 mM as coadsorbent. They used dimethyl propyl imidazolium iodide (0.6 M), lithium iodide (0.1 M), iodine (0.05 M), and tert-butylpyridine (0.5 M) as the electrolyte solution for the integrated DSC. Besides, active area of the cell plays an important role in determining the efficiency of the cell, smaller the active area would result in fewer defects thus lead to higher performance efficiency.

5.3 Benefit

This achievement has resulted in the synthesized TiO₂ photoelectrode material being integrated in dye solar module of size 100 mm x 180 mm (V_{peak} of 4.2 V and I_{peak} of 220 mA) which is capable of operating a small fan when exposed to the sunlight (Figure 5.1). The breakthrough in this noble hierarchical structured photoelectrode material could spur the development of higher performance DSC to challenge the high cost of commercially available silicon-based solar cells.

DSC is currently the most efficient third-generation solar technology and one of the promising sources of alternative energy. In comparison to the existing silicon based photovoltaic system, DSC is made of low-cost materials, cheaper to manufacture and can be printed on any flexible surface. It is also works in cloudy weather and defuses light condition without much impact on its efficiency. Due to this characteristic, DSC is suitable for the building integrated photovoltaic (BIPV) which uses solar cells not only mounted on top of roof but also integrated as walls or glass windows of building to power up consumer appliances (charging, lighting, etc.).



Figure 5.1: Dye solar module of size 100 mm x 180 mm

5.4 Recommendation for Future Work

Development of right nanostructure photoelectrode materials is not the only way to optimize the performance of DSC. There are many other characteristics of photoelectrode materials that need for improvement in the near future. The improvement should include the modification of the optical characteristic and crystallinity of photoelectrode materials. Besides, right composition and methods in preparing the photoelectrode paste is also important since it could affect the porosity, connectivity and stability of the prepared films.

The application of TiO_2 as photoelectrode material in DSC basically related to its optical characteristic namely band gap. It is proven that TiO_2 has band gap energy of 3.2 eV for anatase phase and 3.0 eV for rutile phase. Even though band gap is a requirement, but sometimes it prevents a much higher performance efficiency of a DSC. Thus, future improvement can be directed towards improving the optical properties of TiO_2 photoelectrode material. This can be achieved by doping TiO_2 with some other elements either metal or nonmetal component. Optical characteristic of a material is generally influenced by its underlying electronic structure which is related to its atomic arrangement, chemical composition and its physical dimension.

Other than the optical properties and TiO_2 phase, the crystallinity of the photoelectrode material also plays an important role in the performance of DSC. Due

to low surface energy, the well developed (d_{101}) facets of highly crystalline anatase structure could help in dye anchoring and electrons transfer and at same time provide mesoporous inner structure for the film, which are the primary advantages to the performance of DSCs. The easiest way of improving the crystallinity is through calcination at high temperature. However, it is not favorable due to the possibility of the mesoporous structure to collapse and the consequent loss of surface area. Thus, other ways have to be implemented such as utilizing surfactant during the synthesis process, using other synthesis method namely hydrothermal and chemical vapor deposition as well as controlling the pressure, heating rate, ramping temperature and environment of calcination process.

Another way of improving the performance efficiency of DSC is by optimizing the paste formulation. The right composition and preparation method of TiO_2 paste would affect the deposition of the films which strongly influence the porosity of electrode, surface area, roughness, pore size as well as film thickness. All of these properties will determine the surface and electronic properties of deposited films. Besides, the viscosity of the paste also can be controlled by the optimization of the paste formulation. Right viscosity is important for better deposition especially when inject printing technique is deployed which is essential in establishing a rapid film deposition technique that can be adopted for industrial needs in the upscale application of DSC.

REFERENCES

- [1] R. Leete, "Malaysia generating renewable energy from palm oil wastes," United Nations Development Programme (UNDP), Kuala Lumpur, Malaysia 2007.
- [2] A. R. Mohamed and K. T. Lee, "Energy for sustainable development in Malaysia: Energy policy and alternative energy " *Energy Policy* vol. 34, pp. 2388–2397, 2006.
- [3] S. Selamat and C. Z. A. Abidin, "Renewable energy and kyoto protocol: Adoption in Malaysia," UniMAP The School of Environmental Engineering, 2011.
- [4] L. Y. Seng, G. Lalchand, and C. M. S. Lin, "Economical, environmental and technical analysis of building integrated photovoltaic systems in Malaysia," *Energy Policy*, vol. 36, pp. 2130-2142, 2008.
- [5] J. E. Boercker, "Synthesis of titanium dioxide and zinc oxide nanowires for excitonic solar cells," in *Faculty of the Graduate School* vol. Doctor of Philosophy Minnesota, United States: University of Minnesota, 2009.
- [6] S. A. Kalogirou, *Solar energy engineering: processes and systems*. Oxford: Academic Press, 2009.
- [7] H.-H. Rogner, Z. D., R. B. P. Crabbé, E. O., H. B. (Australia), K. L., and Y. M., "Climate Change 2007: Mitigation," in *Contribution of Working Group III to the Fourth Assessment Report of the Intergovernmental Panel on Climate Change*, B. Metz, O. R. Davidson, P. R. Bosch, R. Dave, and L. A. Meyer, Eds. Cambridge, United Kingdom, New York, USA: Cambridge University Press, 2007.
- [8] W. Moomaw, F. Yamba, M. Kamimoto, L. Maurice, J. Nyboer, K. Urama, and T. Weir, "Introduction," in *IPCC Special Report on Renewable Energy*

- Sources and Climate Change Mitigation*, O. Edenhofer, R. Pichs-Madruga, Y. Sokona, K. Seyboth, P. Matschoss, S. Kadner, T. Zwickel, P. Eickemeier, G. Hansen, S. Schlömer, and C. v. Stechow, Eds. Cambridge, United Kingdom and New York, NY, USA.: Cambridge University Press, 2011.
- [9] IPCC, "Summary for policymakers," in *IPCC Special Report on Renewable Energy Sources and Climate Change Mitigation*, O. Edenhofer, R. Pichs-Madruga, Y. Sokona, K. Seyboth, P. Matschoss, S. Kadner, T. Zwickel, P. Eickemeier, G. Hansen, S. Schlömer, and C. v. Stechow, Eds. Cambridge, United Kingdom and New York, NY, USA: Cambridge University Press, 2011.
- [10] P. Gipe, "Malaysia's 2011 proposed solar, biomass, biogas and hydro tariffs," *RenewableEnergyWorld.com*, 2010.
- [11] A. H. Haris and J. Ding, "The final report on national renewable energy policy and action plan," Pusat Tenaga Malaysia, Selangor, Malaysia 2009.
- [12] I. W. Asma, S. Mahanim, H. Zulkafli, S. Othman, and Y. Mori, "Malaysian palm oil biomass," Osaka, Japan: Global Environment Centre Foundation (GEC), 2010.
- [13] P. O. R. A. o. M. (PORAM), "Annual report for the year ending 31 December 2010," Selangor, Malaysia 2010.
- [14] M. D. Archer, *Clean electricity from photovoltaics* vol. 1. UK: Imperial College Press, 2001.
- [15] T. M. Razykov, C. S. Ferekides, D. Morel, E. Stefanakos, H. S. Ullal, and H. M. Upadhyaya, "Solar photovoltaic electricity: Current status and future prospects," in *Solar Energy*, 2011.
- [16] M. Pagliaro, G. Palmisano, and R. Ciriminna, *Flexible Solar Cells*. Germany: Wiley-VCH, 2006.

- [17] V. S. Murthy, "Third generation solar cells: An overview," in *Technical Insight Alert* Kuala Lumpur: Frost & Sullivan, 2008.
- [18] G. F. Brown and J. Wu, "Third generation photovoltaics," *Laser & Photon. Rev.*, vol. 3, pp. 394-405, 2009.
- [19] M. Gratzel, "Mesoporous oxide junctions and nanostructured solar cells," *Current Opinion in colloid & interface Science*, vol. 4, pp. 314-321, 1999.
- [20] M. Gratzel, "Dye-sensitized solar cells," *J. Photochem. Photobiol. C*, vol. 4, pp. 145-153, 2003.
- [21] M. Gratzel, "Conversion of sunlight to electric power by nanocrystalline dye-sensitized solar cells," *J. Photochem. Photobiol. A*, vol. 164, pp. 3-14, 2004.
- [22] M. Grätzel, "Solar energy conversion by dye-sensitized photovoltaic cells," *Inorg. Chem.*, vol. 44, pp. 6841-6851, 2005.
- [23] K. Hara and H. Arakawa, "Dye-sensitized solar cells," in *Handbook of Photovoltaic Science and Engineering*, A. Luque and S. Hegedus, Eds.: John Wiley & Sons Ltd., 2003, pp. 663-699.
- [24] B. A. Gregg, "Excitonic solar cels," *J. Phys. Chem. B*, vol. 107, pp. 4688-4698, 2003.
- [25] B. O'regan and M. Gratzel, "A low-cost, high-efficiency solar cell based on dye-sensitized colloidal TiO₂ films," *Nature*, vol. 353, pp. 737-740, 1991.
- [26] Y. Chiba, A. Islam, Y. Watanabe, R. Komiya, N. Koide, and L. Han, "Dye-sensitized solar cells with conversion efficiency of 11.1%," *Japanese Journal of Applied Physics*, vol. 45, pp. L638-L640, 2006.
- [27] T. P. Chou, Q. F. Zhang, G. E. Fryxell, and G. Z. Cao, "Hierarchically structured ZnO film for dye-sensitized solar cells with enhanced energy conversion efficiency," *Adv. Mater.*, vol. 19, pp. 2588-2592, 2007.

- [28] Q. F. Zhang, T. P. Chou, B. Russo, S. A. Jenekhe, and G. Z. Cao, "Aggregation of ZnO nanocrystallites for high conversion efficiency in dye-sensitized solar cells," *Angew. Chem. Int. Ed.*, vol. 47, pp. 2402-2406, 2008.
- [29] Q. F. Zhang, C. S. Dandeneau, X. Y. Zhou, and G. Z. Cao, "ZnO nanostructures for dye-sensitized solar cells," *Adv. Mater.*, vol. 19, pp. 4087-4108, 2009.
- [30] S. Nakade, Y. Saito, W. Kubo, T. Kitamura, Y. Wada, and S. Yanagida, "Influence of TiO₂ nanoparticle size on electron diffusion and recombination in dye sensitized TiO₂ solar cells," *J. Phys. Chem. B*, vol. 107, pp. 8607-8611, 2003.
- [31] J. Yu, J. Fan, and L. Zhao, "Dye-sensitized solar cells based on hollow anatase TiO₂ spheres prepared by self-transformation method " *Electrochimica Acta*, vol. 55, pp. 597-602, 2010.
- [32] X. Chen and S. S. Mao, "Synthesis of titanium dioxide (TiO₂) nanomaterial," *Journal of Nanoscience & Nanotechnology*, vol. 6, pp. 906-925, 2006.
- [33] J. Jiu, S. Isoda, M. Adachi, and F. Wang, "Preparation of TiO₂ nanocrystalline with 3-5 nm and application for dye-sensitized solar cell," *J. Photochem. Photobiol. A*, vol. 189, pp. 314-321, 2007.
- [34] J. Jiu, S. Isoda, M. Adachi, and H. Wang, "Dye-sensitized Solar Cell based on Nanocrystalline TiO₂ with 3-10 nm in Diameter," *J. Mater Sci: Mater. Electron.*, vol. 18, pp. 593-597, 2007.
- [35] B. Tan and Y. Wu, "Dye-sensitized solar cells based on anatase TiO₂ nanoparticle/nanowire composites," *J. Phys. Chem. B*, vol. 110, pp. 15932-15938, 2006.
- [36] J. Jiu, S. Isoda, F. Wang, and M. Adachi, "Dye-sensitized solar cells based on a single-crystalline TiO₂ nanorod film," *J. Phys. Chem. B*, vol. 110, pp. 2087-2092, 2006.

- [37] G. K. Mor, K. Shankar, M. Paulose, O. K. Varghese, and C. A. Grimes, "Use of highly-ordered TiO₂ nanotube arrays in dye-sensitized solar cells," *Nano Letter*, vol. 6, pp. 215-218, 2006.
- [38] J. Liu, G. Cao, Z. Yang, D. Wang, D. Dubois, X. Zhou, G. L. Graff, L. R. Pederson, and J. G. Zhang, "Oriented nanostructures for energy conversion and storage," *ChemSusChem*, vol. 11, pp. 676-697, 2001.
- [39] Q. F. Zhang, T. P. Chou, B. Russo, S. A. Jenekhe, and G. Z. Cao, "Polydisperse aggregates of ZnO nanocrystallites: A method for energy-conversion-efficiency enhancement in dye-sensitized solar cells," *Adv. Funct. Mater.*, vol. 18, pp. 1654-1660, 2008.
- [40] G. Cao, Q. F. Zhang, and J. Brinker, "Dye-sensitized solar cells based on nano-structured zinc oxide," in *Annual Review of Nano Research*. vol. 3 Singapore: World Scientific Publishing Co. Pte. Ltd, 2009, pp. 385-440.
- [41] D. A. Tryk, A. Fujishima, and K. Honda, "Recent topics in photoelectrochemistry: achievements and future prospects," *Electrochimica Acta*, vol. 45, pp. 2363-2376, 2000.
- [42] K. Sayama, H. Sugihara, and H. Arakawa, "Photoelectrochemical properties of a porous Nb₂O₅ electrode sensitized by a ruthenium dye," *Chem. Mater.*, vol. 10, pp. 3825-3832, 1998.
- [43] M. Law, L. E. Greene, A. Radenovic, T. Kuykendall, J. Liphardt, and P. Yang, "ZnO-Al₂O₃ and ZnO-TiO₂ core-shell nanowire dye-sensitized solar cells," *J. Phys. Chem. B*, vol. 110, pp. 22652-22663, 2006.
- [44] X. Tang, J. Q. Ian, Z. Wang, H. Wang, Q. Feng, and G. Liu, "Comparison of low crystallinity TiO₂ film with nanocrystalline anatase film for dye-sensitized solar cells," *J. Coll. Int. Sci*, vol. 330, pp. 386-391, 2009.
- [45] H. Yin, Y. Wada, T. Kitamaru, S. Kambe, S. Murasawa, H. Mori, T. Sakata, and S. Yanagida, "Hydrothermal synthesis of nanosized anatase and rutile

- TiO₂ using amorphous phase TiO₂," *J. Mater. Chem.*, vol. 11, pp. 1694-1703, 2001.
- [46] N.-G. Park, J. v. d. Lagemaat, and A. J. Frank, "Comparison of dye-sensitized rutile and anatase-based TiO₂ solar cells," *J. Phys. Chem. B*, vol. 104, pp. 8989-8994, 2000.
- [47] M. K. Nazeeruddin, F. D. Angelis, S. Fantacci, A. Selloni, G. Viscardi, P. Liska, S. Ito, B. Takeru, and M. Grätzel, "Combined experimental and DFT-TDDFT computational study of photoelectrochemical cell ruthenium sensitizers," *J. Am. Ceram. Soc.*, vol. 127, pp. 16835-16847, 2005.
- [48] M. K. Nazeeruddin, A. Kay, I. Rodicio, R. Humphry-Baker, E. Mueller, P. Liska, N. Vlachopoulos, and M. Gratzel, "Conversion of light to electricity by cis-X₂bis(2,2'-bipyridyl-4,4'-dicarboxylate)ruthenium(II) charge-transfer sensitizers (X = Cl-, Br-, I-, CN-, and SCN-) on nanocrystalline titanium dioxide electrodes," *J. Am. Ceram. Soc.*, vol. 115, pp. 6382-6390, 1993.
- [49] G. C. Vougioukalakis, A. I. Philippopoulos, T. Stergiopoulos, and P. Falaras, "Contributions to the development of ruthenium-based sensitizers for dye-sensitized solar cells " *Coordination Chemistry Reviews*, vol. 255, pp. 2602-2621, 2011.
- [50] M. K. Nazeeruddin, P. Péchy, and M. Grätzel, "Efficient panchromatic sensitization of nanocrystalline TiO₂ films by a black dye based on atrithiocyanato-ruthenium complex," *Chem. Commun.*, pp. 1705-1706, 1997.
- [51] A. Hagfeldt and M. Gratzel, "Light-induced redox reactions in nanocrystalline systems," *Chem. Rev.*, vol. 95, pp. 49-68, 1995.
- [52] R. Argazzi, N. Y. M. Iha, H. Zabri, F. Odobel, and C. A. Bignozzi, "Design of molecular dyes for application in photoelectrochemical and electrochromic devices based on nanocrystalline metal oxide semiconductors," *Coordination Chemistry Review*, vol. 248, pp. 1299-1316, 2004.

- [53] M. K. Nazeeruddin, S. M. Zakeeruddin, J.-J. Lagref, P. Liska, P. Comte, C. Barolo, G. Viscardi, K. Schenk, and M. Graetzel, "Stepwise assembly of amphiphilic ruthenium sensitizers and their applications in dye-sensitized solar cell," *Coordination Chemistry Reviews*, vol. 248, pp. 1317-1328, 2004.
- [54] A. S. Polo, M. K. Itokazu, and N. Y. M. Iha, "Metal complex sensitizers in dye-sensitized solar cells," *Coordination Chemistry Review*, vol. 248, pp. 1343-1361, 2004.
- [55] G. J. Meyer, "Molecular approaches to solar energy conversion with coordination compounds anchored to semiconductor surfaces," *Inorg. Chem.*, vol. 44, pp. 6852-6864, 2005.
- [56] L. M. Goncalves, V. d. Z. Bermedez, H. A. Ribeiro, and A. M. Mendes, "Dye-sensitized solar cells: a safe bet for the future," *Energy Environ. Sci.*, vol. 1, pp. 655-667, 2008.
- [57] Y. Liu, A. Hagfeldt, X.-R. Xiao, and S.-E. Lindquist, "Investigation of influence of redox species on the interfacial energetics of a dye-sensitized nanoporous TiO₂ solar cell," *solar Energy Material & Solar Cells*, vol. 55, pp. 267-281, 1998.
- [58] K. Hara, T. Horiguchib, T. Kinoshitab, K. Sayama, and H. Arakawa, "Influence of electrolytes on the photovoltaic performance of organic dye-sensitized nanocrystalline TiO₂ solar cells," *Solar Energy Materials and Solar Cells*, vol. 70, pp. 151-161, 2001.
- [59] P. Wang, S. M. Zakeeruddin, J.-E. Moser, and M. Grätzel, "A new ionic liquid electrolyte enhances the conversion efficiency of dye-sensitized solar cells," *J. Phys. Chem. B*, vol. 107, pp. 13280-13285, 2003.
- [60] L. Wang, S. Fang, Y. Lin, X. Zhou, and M. Li, "A 7.72% efficient dye sensitized solar cell based on novel necklace-like polymer gel electrolyte containing latent chemically cross-linked gel electrolyte precursors," *Chem. Commun.*, pp. 5687-5689, 2005.

- [61] A. Kay and M. Grätzel, "Low cost photovoltaic modules based on dye sensitized nanocrystalline titanium dioxide and carbon powder," *Solar Energy Materials and Solar Cells*, vol. 44, pp. 99-117, 1996.
- [62] M. Gratzel and J. R. Durrant, "Dye-sensitized Mesoscopic solar cells," in *Nanostructured and Photoelectrochemical Systems for Solar Photon Conversion*, vol. 3, A. J. N. Mary D Archer, Ed. London: Imperial College Press, 2003.
- [63] D. Matthews, P. Infelta, and M. Gratzel, "Calculation of the photocurrent-potential characteristic for regenerative, sensitized semiconductor electrodes," *Solar Energy Materials and Solar Cells*, vol. 44, pp. 119-155, 1996.
- [64] Q. Zhang and G. Cao, "Nanostructured photoelectrodes for dye-sensitized solar cells," *Nano Today*, vol. 6, pp. 91-109, 2011.
- [65] S. Y. Huang, G. Schlichthörl, A. J. Nozik, M. Grätzel, and A. J. Frank, "Charge recombination in dye-sensitized nanocrystalline TiO₂ solar cells," *J. Phys. Chem. B*, vol. 101, pp. 2576-2582, 1997.
- [66] D. Cahen, G. Hodes, M. Grätzel, J. F. Guillemoles, and I. Riess, "Nature of photovoltaic action in dye-sensitized solar cells," *J. Phys. Chem. B*, vol. 104, pp. 2053-2059, 2000.
- [67] Y. Lee, J. Chae, and M. Kang, "Comparison of the photovoltaic efficiency on DSSC for nanometer sized TiO₂ using a conventional sol-gel and solvothermal methods," *J. Ind. Eng. Chem.*, vol. 16, pp. 609-614, 2010.
- [68] A. B. F. Martinson, T. W. Hamann, M. J. Pellin, and J. T. Hupp, "New architectures for dye-sensitized solar cells," *Chem. Eur. J.*, vol. 14, pp. 4458-4467, 2008.
- [69] D. V. Bavykin, V. N. Parmon, A. A. Lapkina, and F. C. Walsh, "The effect of hydrothermal conditions on the mesoporous structure of TiO₂ nanotubes," *J. Mater. Chem.*, vol. 14, pp. 3370-3377, 2004.

- [70] R. Ma, Y. Bando, and T. Sasaki, "Directly rolling nanosheets into nanotubes," *J. Phys. Chem. B*, vol. 82, pp. 2115-2119, 2004.
- [71] B. D. Yao, Y. F. Chan, X. Y. Zhang, W. F. Zhang, Z. Y. Yang, and N. Wang, "Formation mechanism of TiO₂ nanotubes," *Appl. Phys. Lett.*, vol. 82, pp. 281-283, 2003.
- [72] S. Liu and K. Huang, "Straight forward fabrication of highly ordered TiO₂ nanowire array in AAM on aluminum substrate," *Solar Energy Material & Solar Cells*, vol. 85, pp. 125-131, 2005.
- [73] A. Ghicov, S. P. Albu, R. Hahn, D. Kim, T. Stergiopoulos, J. Kunze, C.-A. Schiller, P. Falaras, and P. Schmuki, "TiO₂ nanotubes in dye-sensitized solar cells: Critical factors for the conversion efficiency," *Chem. Asian J.*, vol. 4, pp. 520-525, 2009.
- [74] N. N. Bwana, "Comparison of the performances of dye-sensitized solar cells based on different TiO₂ electrode nanostructures," *J. nanopart. Res.*, vol. 11, pp. 1917-1923, 2009.
- [75] G. Oskam, A. Nellore, R. L. Penn, and P. C. Searson, "The growth kinetics of TiO₂ nanoparticles from titanium (IV) alkoxide at high water/titanium ratio," *J. Phys. Chem. B*, vol. 107, pp. 1734-1738, 2003.
- [76] Y. Bessekhoud, D. Robert, and J. V. Weber, "Synthesis of photocatalytic TiO₂ nanoparticles: optimization of the preparation conditions," *J. Photochem. Photobiol. A*, vol. 157, pp. 47-53, 2003.
- [77] H. Zhang and J. F. Banfield, "Kinetics of crystallization and crystal growth of nanocrystalline anatase in nanometer-sized amorphous titania," *Chem. Mater.*, vol. 14, pp. 4145-4154, 2002.
- [78] H. Zhang, M. Finnegan, and J. F. Banfield, "Preparing single-phase nanocrystalline anatase from amorphous titania with particle sizes tailored by temperature," *Nano Lett.*, vol. 1, pp. 81-85, 2001.

- [79] J. Ferber and J. Luther, "Computer simulations of light scattering and absorption in dye-sensitized solar cells," *Solar Energy Materials and Solar Cells*, vol. 54, pp. 265-275, 1998.
- [80] A. Usami, "Theoretical study of application of multiple scattering of light to a dye-sensitized nanocrystalline photoelectrochemical cell," *Chemical Physics Letters*, vol. 277, pp. 105-108, 1997.
- [81] G. Rothenberger, P. Comte, and M. Grätzel, "A contribution to the optical design of dye-sensitized nanocrystalline solar cells," *Solar Energy Materials and Solar Cells*, vol. 58, pp. 321-336, 1999.
- [82] H.-J. Koo, J. Park, B. Yoo, K. Yoo, K. Kim, and N.-G. Park, "Size-dependent scattering efficiency in dye-sensitized solar cell," *Inorganica Chimica Acta*, vol. 361, pp. 677-683, 2008.
- [83] S. Hore, P. Nitz, C. Vetter, C. Prahl, M. Niggemann, and R. Kern, "Scattering spherical voids in nanocrystalline TiO₂ – enhancement of efficiency in dye-sensitized solar cells," *Chem. Commun.*, pp. 2011–2013, 2005.
- [84] Q. Zhang, C. S. Dandeneau, K. Park, D. Liu, X. Zhou, Y.-H. Jeong, and G. Cao, "Light scattering with oxide nanocrystallite aggregates for dye-sensitized solar cell application," *Journal of Nanophotonics*, vol. 4, p. 041540, 2010.
- [85] J. Xi, Q. Zhang, K. Park, Y. Sun, and G. Cao, "Enhance power conversion efficiency in dye-sensitized solar cells with TiO₂ aggregates/nanocrystallite mixed photoelectrodes.," *Electrochimica Acta*, vol. 56, pp. 1960-1966, 2011.
- [86] Y. J. Kim, M. H. Lee, H. J. Kim, G. Lim, Y. S. Choi, N.-G. Park, K. Kim, and W. I. Lee, "Formation of highly efficient dye-sensitized solar cells by hierarchical pore generation with nanoporous TiO₂ spheres," *Adv. Mater.*, vol. 21, pp. 3668–3673, 2009.
- [87] E. A. Barringer and H. K. Bowen, "High-purity, monodisperse TiO₂ powders by hydrolysis of titanium tetraethoxide: 1. Synthesis and physical properties," *Langmuir*, vol. 1, pp. 414-420, 1985.

- [88] J. H. Jean and T. A. Ring, "Nucleation and growth of monosized TiO₂ powders from alcohol solution," *Langmuir*, vol. 2, pp. 251-255, 1986.
- [89] E. A. Barringer and H. K. Bowen, "High-purity, monodisperse TiO₂ powders by hydrolysis of titanium tetraethoxide: 2. Aqueous interfacial electrochemistry and dispersion stability," *Langmuir*, vol. 1, pp. 420-428, 1985.
- [90] S. Ito, P. Chen, P. Comte, M. K. Nazeeruddin, P. Liska, P. Pechy, and M. Gratzel, "Fabrication of screen-printing paste from TiO₂ powders for dye-sensitized solar cells," *Prog. Photovolt: Res. Appl.*, vol. 15, pp. 603-612, 2007.
- [91] J. Haber, J. H. Block, and B. Delmon, "Manual of methods and procedures for catalyst characterization (Technical Report)," *Pure & Appl. Chem.*, vol. 67, pp. 1257-1306, 1995.
- [92] D.-U. Lee, S.-R. Jang, R. Vittal, J. Lee, and K.-J. Kim, "CTAB facilitated spherical rutile TiO₂ particles and their advantage in a dye-sensitized solar cell," *Solar Energy*, vol. 82, pp. 1042-1048, 2008.
- [93] J. Wu, S. Hao, J. Lin, M. Huang, Y. Huang, Z. Lan, and P. Li, "Crystal morphology of anatase titania nanocrystals used in Dye-sensitized solar cells," *Crystal Growth & Design*, vol. 8, pp. 247-252, 2008.
- [94] M. G. Kang, K. S. Ryu, S. H. Chang, N. G. Park, J. S. Hong, and K.-J. Kim, "Dependence of TiO₂ film thickness on photocurrent-voltage characteristics of dye-sensitized solar cells," *Bull. Korean Chem. Soc*, vol. 25, pp. 742-744, 2004.
- [95] V. Baglio, M. Girolamo, V. Antonucci, and A. S. Aricò, "Influence of TiO₂ film thickness on the electrochemical behaviour of dye-sensitized solar cells," *Int. J. Electrochem. Sci*, vol. 6, pp. 3375-3384, 2011.
- [96] J. Halme, "Dye-sensitized nanostructured and organic photovoltaic cells: technical review and preliminary tests," in *Department of Engineering Physics*

and Mathematics. vol. Master of Science in Technology Helsinki, Finland: University of Helsinki, 2002, p. 115.

- [97] Y. Leng, "Thermal analysis," in *Material Characterization: Introduction to Microscopic and Spectroscopic Methods* Hong Kong: John Wiley & Sons (Asia) Pte Ltd, 2008.
- [98] W. N. Wang, I. W. Lenggono, Y. Terashi, T. O. Kim, and K. Okuyama, "One-step synthesis of titanium oxide nanoparticles by spray pyrolysis of organic precursors," *Mater. Sci. Eng. B*, vol. 123, pp. 194-202, 2005.
- [99] H. Xie, Q. Zhang, T. Xi, H. Wang, and Y. Liu, "Thermal analysis on nanosized TiO₂ prepared by hydrolysis," *Thermochimica Acta*, vol. 381, pp. 45-48, 2002.
- [100] Y. Gao, Y. Masuda, Z. Peng, T. Yonezawa, and K. Koumoto, "Room temperature deposition of a TiO₂ thin film from aqueous peroxotitanate solution," *J. Mater. Chem.*, vol. 13, pp. 608-613, 2003.
- [101] Y. Hu, H.-L. Tsai, and C. L. Huang, "Phase transformation of precipitated TiO₂ nanoparticles," *Mater Sci. Eng. A*, vol. 344, pp. 209-214, 2003.
- [102] Y. Leng, "X-Ray diffraction method," in *Material Characterization: Introduction to Microscopic and Spectroscopic Methods* Hong Kong: John Wiley & Sons (Asia) Pte. Ltd., 2008, pp. 45-76.
- [103] T. P. Chou, Q. F. Zhang, B. Russo, G. E. Fryxell, and G. Z. Cao, "Titania particle size effect on the performance of dye-sensitized solar cells," *J. Phys. Chem. C*, vol. 111, pp. 6296-6302, 2007.
- [104] S. Agarwala, M. Kevin, A. S. W. Wong, C. K. N. Peh, V. Thavasi, and G. W. Ho, "Mesophase ordering of TiO₂ film with high surface area and strong light harvesting for dye-sensitized solar cell," *Applied Materials & Interfaces*, vol. 2, pp. 1844-1850, 2010.

- [105] X. Chen and S. S. Mao, "Titanium dioxide nanomaterials: synthesis, properties, modification and applications," *Chem. Rev.*, vol. 107, pp. 2891-2959, 2007.
- [106] J. Park, V. Privman, and E. Matijević, "Model of Formation of Monodispersed Colloids," *J. Phys. Chem. B*, vol. 105, pp. 11630-11635, 2001.
- [107] J.-K. Lee, B.-H. Jeong, S.-i. Jang, Y.-G. Kim, Y.-W. Jang, S.-B. Lee, and M.-R. Kim, "Preparations of TiO₂ pastes and its application to light-scattering layer for dye-sensitized solar cells," *Journal of Industrial and Engineering Chemistry*, vol. 15, pp. 724-729, 2009.
- [108] J. G. Yu, Y. R. Su, and B. Cheng, "Template-free fabrication and enhanced photocatalytic activity of hierarchical macro-/mesoporous titania," *Advanced Functional Materials*, vol. 17, pp. 1984-1990, 2007.
- [109] S. Nakade, T. Kanzaki, Y. Wada, and S. Yanagida, "Stepped light-induced transient measurements of photocurrent and voltage in dye-sensitized solar cells: application for highly viscous electrolyte systems," *Langmuir*, vol. 21, pp. 10803-10807, 2005.
- [110] S. Pavasupree, Y. Suzuki, S. Pivsa-Art, and S. Yoshikawa, "Preparation and characterization of mesoporous MO₂ (M = Ti, Ce, Zr and Hf) nanopowders by a modified sol-gel method," *Ceramics International*, vol. 31, pp. 959-963, 2005.
- [111] J. Yu, G. Wang, B. Cheng, and M. Zhou, "Effects of hydrothermal temperature and time on the photocatalytic activity and microstructures of bimodal mesoporous TiO₂ powders," *Applied Catalysis B: Environmental*, vol. 69, pp. 171-180, 2007.
- [112] J. Yua, J. Fan, and L. Zhao, "Dye-sensitized solar cells based on hollow anatase TiO₂ spheres prepared by self-transformation method," *Electrochimica Acta*, vol. 55, pp. 597-602, 2010.

- [113] J. Yu, L. Zhang, B. Cheng, and Y. Su, "Hydrothermal preparation and photocatalytic activity of hierarchically sponge-like macro-/mesoporous titania," *J. Phys. Chem. C*, vol. 111, pp. 10582-10589, 2007.
- [114] J. Yu, W. Wang, B. Cheng, and B.-L. Su, "Enhancement of photocatalytic activity of mesoporous TiO₂ powders by hydrothermal surface fluorination treatment," *J. Phys. Chem. C*, vol. 113, pp. 6743-6750, 2009.
- [115] K. S. W. Sing, D. H. Everett, R. A. W. Haul, L. Moscou, R. A. Pierotti, J. Rouquerol, and T. Siemieniowska, "Reporting physisorption data for gas/solid systems," *Pure & Appl. Chem.*, vol. 57, pp. 603-619, 1985.
- [116] S. Ngamsinlapasathian, T. Fujieda, Y. Suzuki, and S. Yoshikawa, "Dye-sensitized solar cells using mesoporous TiO₂-based electrodes," in *The 2nd Joint International Conference on "Sustainable Energy and Environment (SEE 2006)"* Bangkok, Thailand, 2006.
- [117] Z. S. Wang, H. Kawauchi, T. Kashima, and H. Arakawa, "Significant influence of TiO₂ photoelectrode morphology on the energy conversion efficiency of N719 dye-sensitized solar cell," *Coordination Chemistry Review*, vol. 248, pp. 1381-1389, 2004.
- [118] H. Kusama, M. Kurashige, K. Sayama, M. Yanagida, and H. Sugihara, "Improved performance of Black-dye-sensitized solar cells with nanocrystalline anatase TiO₂ photoelectrodes prepared from TiCl₄ and ammonium carbonate," *Journal of Photochemistry and Photobiology A: Chemistry*, vol. 189, pp. 100-104, 2007.
- [119] S. K. Deb, "Dye-sensitized TiO₂ thin-film solar cell research at the National Renewable Energy Laboratory (NREL)," *Solar Energy Material & Solar Cells*, vol. 88, pp. 1-10, 2005.
- [120] R. L. Penn and J. F. Banfield, "Oriented attachment and growth, twinning, polytypism, and formation of metastable phases: Insights from nanocrystalline TiO₂," *American Mineralogist*, vol. 83, pp. 1077-1082, 1998.

- [121] H. Zhang and J. F. Banfield, "Size dependence of the kinetic rate constant for phase transformation in TiO₂ nanoparticles," *Chem. Mater.*, vol. 17, pp. 3421-3425, 2005.

APPENDIX A

Figure of Characterization Equipment



Figure 3.5: The image of EXSTAR TG/DTA 6000 Series

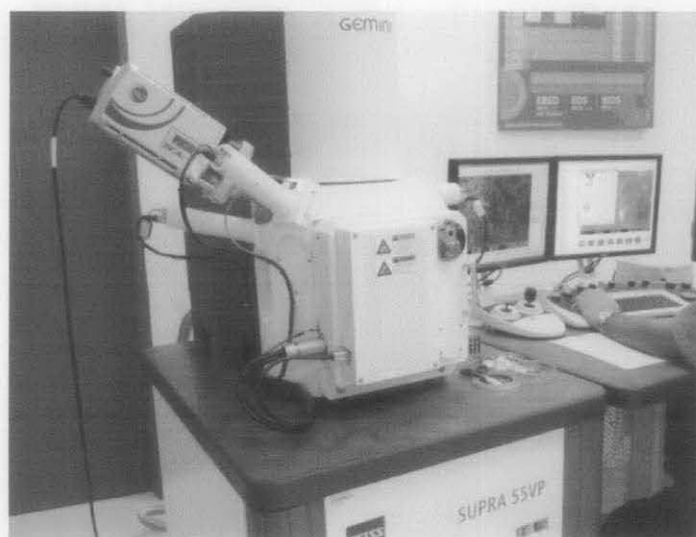


Figure 3.7: Image of Zeiss Supra 55VP Scanning Electron Microscopy



Figure 3.8: Image of X-Ray Diffractometer D8 Advance

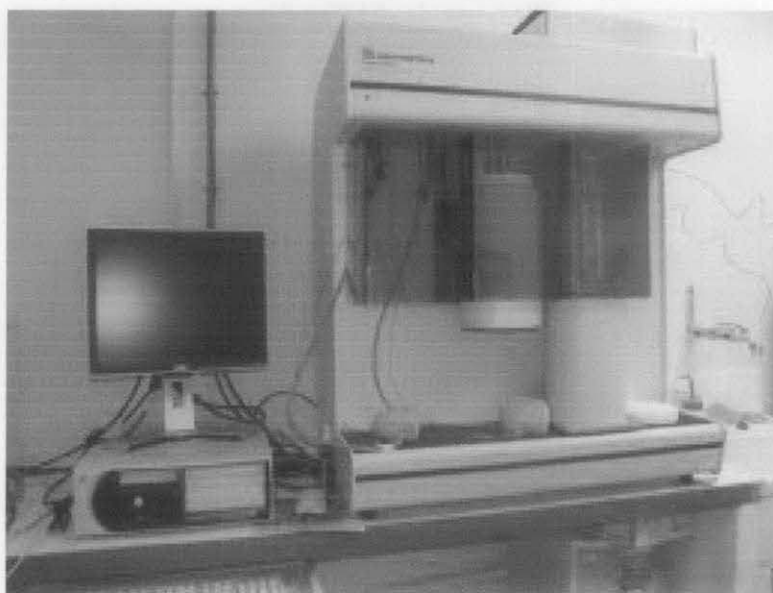


Figure 3.11: Image of Surface Area and Pore Size Analyzer model Micromeritics
ASAP 2020

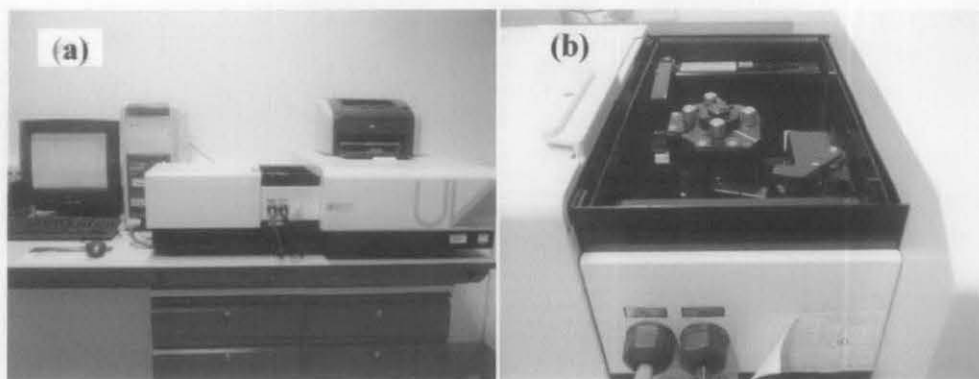


Figure 3.12: Image of (a) UV-Vis Reflectance Spectrophotometer (Shimadzu UV-3150) and (b) the sample holder

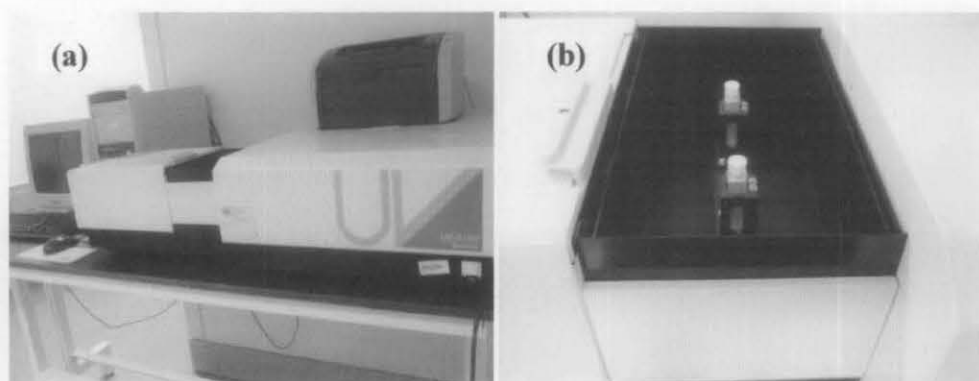


Figure 3.13: Image of (a) UV-Vis Spectrophotometer (Shimadzu UV-3150) and (b) the sample holder

APPENDIX B

List of Patent Filed/Publication/Exhibition & Award/Conference & Seminar

Patent Filed:

1. Fabrication of dye solar module using TiO₂ aggregates-nanocrystallites composites

Publication:

1. Siti Nur Azella Zaine, Ahmad Anis Kalantar Mastan, Sharizal Shaik Ahmedullah, Norani Muti Mohamed, Anita Ramli and Ita Athirah, "Synthesis and characterization of pure anatase TiO₂ aggregates," Journal of Applied Sciences, vol. 11, pp. 1326-1330, 2011.

DOI: 10.3923/jas.2011.1326.1330

2. Siti Nur Azella Zaine, Norani Muti Mohamed and Mohd Azmi Bustam, "The effect of calcination temperature on the performance of TiO₂ aggregates-based dye solar cells (DSC)," Advanced Materials Research, vol. 364, pp. 248-253, Oct. 2011.

DOI: 10.4028/www.scientific.net/AMR.364.248

Exhibition & Award:

1. NanoMalaysia Summit & Exhibition 2011 at Putra World Trade Centre (PWTC), Malaysia, June 2011.
2. Malaysia Technology Expo 2011, silver medal, through the invention of "Low-cost Dye Solar Module with Better Overall Performance in Real Solar Condition," Kuala Lumpur, Malaysia, Feb 2011.
3. INNOVA Brussels Exposition 2010, gold medal, through the invention of "Fabrication of Dye Sensitized Solar Module (DSSM) using TiO₂ Nanocomposites," Brussel, Belgium, Oct 2010.

Conference & Seminar:

1. N. M. Mohamed, S. N. A. Zaine, Performance of TiO₂ aggregates-based dye solar cells. submitted for presentation in Nanotechnology Applications in Energy & Environment (NAEE2012), Bandung, 20-21 Sep. 2012.

2. N. M. Mohamed, S. N. A. Zaine, M. A. Bustam, Performance of dye solar cells based on TiO₂ aggregates/nanoparticles composite. accepted for presentation in the 8th International Conference on Diffusion in Solids & Liquids (DSL2012), Istanbul, Turkey, 25-29 June 2012.
3. N. M. Mohamad, S. N. A. Zaine. Optimized TiO₂ nanocrystallite aggregates for enhanced efficiency in dye solar cells. Submitted for presentation in 2nd International Conference on Process Engineering and Advanced Materials (ICPEAM 2012). Kuala Lumpur Convention Centre, Malaysia. 12 - 14 June 2012.
4. N. M. Mohamed, S. N. A. Zaine and M. A. Bustam. Effect of process parameter on the performance of TiO₂ aggregates-based dye solar cell. presented at International Conference on Nanoscience and Technology. Beijing, China. 7-9 Sept. 2011.
5. S. N. A. Zaine, N. M. Mohamed and M. A. Bustam. Development of TiO₂ aggregates as photoelectrode material in dye solar cells (DSCs). presented at 1st UTP-SOJO Nano and Bio Joint Seminar. Universiti Teknologi PETRONAS, Malaysia. 30 Sept. 2011.
6. S. N. A. Zaine, N. M. Mohamed and M. A. Bustam. The effect of calcination temperature on the performance of TiO₂ aggregates-based dye solar cells (DSCs). presented at International Conference for Nanomaterials Synthesis and Characterization. Seri Kembangan, Malaysia. 6-7 July 2011.
7. S. N. A. Zaine, N. M. Mohamed and M. A. Bustam. Effect of water content in the formation of TiO₂ aggregates on the performance of dye solar cells (DSCs). presented at International Conference of Nanotechnology Research and Commercialization. Sabah, Malaysia. 6-9 June 2011
8. N.M. Mohamed, S.N.A. Zaine, A. Mohd Ismail, A.A. Kalantar Mastan, S. Shaik Ahmedullah, Enhanced efficiency of dye-sensitized solar cells using TiO₂ aggregates-nanoparticles composites. presented at 4th International Conference on the Industrialisation of Dye Solar Cells (DSC-IC2010), Colorado Springs, CO, USA, 1-4 Nov. 2010.
9. S. N. A. Zaine, A. A. K. Mastan, S. S. Ahmedullah, N. M. Mohamad, A. Ramli and I. A. Ahmad. Synthesis and characterization of pure anatase TiO₂

aggregates. presented at International Conference on Fundamental & Applied Sciences. Kuala Lumpur Convention Centre, Malaysia. 15 - 17 June 2010.